Fabrication and Characterisation of Zinc Oxide Thin Films Singly doped With Trace amounts of Rare Earth Materials

A thesis submitted in partial fulfillment

of the requirements for the Degree

of

Doctor of Philosophy in Physics

in the

University of Canterbury

by

Masaed M. Almotari

Department of Physics and Astronomy

University of Canterbury

2013

Contents

List of Figures

List of Tables

Acknowledgments

As a matter of fact the decision to travel from your home to another country on the other side of the world, and to be away from your family and loved ones for a number of years, is not an easy one to make. However, for me the purpose motivating me travelling to come to New Zealand was solely to pursue my studies and to gain knowledge from highly experienced, skilful and educated people.

I am very indebted and grateful to many people who have helped me in one way or another during my studies. First and foremost, I would like to express my sincere gratitude to all my family members for their encouragement, assistance, care and endless love. My parents have always remembered me in their prayers and thoughts. My brothers and sister have been unceasingly supportive. I would also like to thank my lovely wife, Amal, for being always at my side backing me up, especially during some very difficult times. I still clearly remember my mixed feelings when I had to send her back to Saudi Arabia and had to remain in Christchurch alone because of the devastating earthquake that struck Christchurch in 2011. At the time she was pregnant with our first child.

I would like to thank my principal supervisor, Professor Roger Reeves, for his guidance, encouragement and helpful discussions. Also, many thanks due to Dr. Scott Choi, Dr. Ian Farrell, Dr. Rueben Mendelsberg and my fellow research student, Young Wook Song, for giving me some of their valuable time to train me up on the use of various instruments necessary to carrying out my research. I should also thank Prof. Rod Syme for reading my thesis in draft form and providing me with fruitful suggestions and comments.

I would like to thank the technical staff of the Physics and Astronomy Department, University of Canterbury, for their assistance and for running the spectroscopy lab so superbly well.

Finally, particular thanks to Prof. Ahmed Y. Alyamani at the National Nanotechnology Research Centre, King Abdulaziz City for Science and Technology (KACST), for allowing me to conduct the first part of my experimental work in his lab. I am very grateful to him for his tremendous support, guidance and encouragement. He has been a great help to me.

Abstract

Two sets of nanostructured Zinc Oxide (ZnO) thin films doped with varying nominal concentrations of rare earth (RE) ions were prepared by pulsed laser deposition (PLD). One set was doped with europium ions ($ZnO:Eu^{3+}$) while the other was doped with erbium ions ($ZnO:Er^{3+}$). The nominal concentration of RE ions ranged from 0.025 to 5 atomic %. The produced films were structurally, morphologically and optically characterised using different techniques such as X-ray diffraction (XRD), scanning electron microscopy (SEM), photoluminescence (PL), combined excitation and emission spectroscopy (CEES) and X-ray photoelectron spectroscopy (XPS).

All films were found to possess a single-crystal hexagonal structure and were strongly oriented along the *c*-axis. However, the crystallinity of the investigated films seemed to deteriorate as the concentration of the rare earth ions increased. This deterioration is assumed to be due to the local distortion of the ZnO structure (host material) caused by the insertion of the relatively large RE ions, hence inducing structural stresses.

Importantly, XRD measurements showed that no other crystalline phases related to europium or erbium, such as Eu_2O_3 or Er_2O_3, were observed. Surprisingly, the ZnO lattice constant (*c*) tended to become smaller as more RE^{3+} ions were added to the films. An explanation is offered whereby this observation can be taken as further evidence that Zn^{2+} ions were successfully substituted by RE^{3+} ions.

Interestingly, doping ZnO films with RE^{3+} ions of a nominal concentration of ≥ 0.5 at.% or higher exhibited a drastic effect on the optical properties of the host matrix (ZnO) in which the near band edge luminescence characteristic of pure ZnO completely disappeared.

According to SEM images, morphological changes also occur as dopant concentrations increase. Well-defined grains (crystallites) were clearly seen in films doped with < 0.5 at.% of RE ions. However, these grains became hardly distinguishable at higher RE ion concentrations.

Typical intra-4f shell transitions of RE^{3+} ions were observed when these ions were non-resonantly excited with UV radiation, indicating that energy had been efficiently transferred from ZnO to the rare earth ions. A plausible physical mechanism for this energy transfer is proposed.

The radiative optical centres of rare earth ions were studied by CEES. In these experiments, both sets of films exhibited multiple optical sites. ZnO:Eu^{3+} thin films were found to have two distinct optical sites with differing site symmetries, whereas up to four optical sites were detected in the ZnO:Er^{3+} films.

.

Chapter 1

INTRODUCTION

The invention of the p-n junction in the beginning of the twentieth century was a key turning point, leading to the huge revolution in semiconductor-based electronics technology. Classical semiconductors such as silicon (Si), germanium (Ge), gallium arsenide (GaAs) and related III-V materials were the earliest materials used in the industry of electronics and are characterised by their small to moderate bandgap energies. The bandgap energy of Ge and Si is 0.67 eV and 1.12 eV respectively while GaAs has 1.43 eV. However, classical semiconductors cannot be effectively utilised to fulfill the rapidly growing demand for efficient optical, high-temperature, high-frequency and high-power semiconductor-based devices due to their performance limitation induced by the narrow size of the bandgap.[1] Such unwanted limitation is explained next.

From the point of view of fabricating semiconductor-based devices, decreasing intrinsic free-carrier (thermally generated carrier) concentrations below the concentration of extrinsic carriers induced by doping is a key factor for improving the performance of the device. At high temperatures the concentration of the intrinsic carriers in classical semiconductors is high in contrast to wide bandgap materials. Therefore, semiconductors with wider band gaps are considered preferable for designing a device for higher temperature applications, to offset the degradation of the device performance due to the unnecessary increase of the intrinsic carrier numbers. Moreover, small-gap semiconductors are known to suffer from a low breakdown voltage which limits their practicality in high operating voltage instruments for high power and gain applications.[2, 3]

Furthermore, there are additional unique features for wide-gap semiconductors such as high saturation velocity, high thermal conductivity, chemically stable and low thermally generated leakage current.[2] Based on these reasons there is strong motivation, supported by intensive research activities, for shifting to wide bandgap semiconductors for efficient light, higher-temperature, high-voltage and high-frequency devices.[4] The correct choice of semiconductor is extremely important in determining its usefulness in practical applications. A semiconductor which has a gap energy greater than 2 eV is considered "wide bandgap".[1] Figure 1.1 depicts a large number of wide bandgap semiconductors (direct and indirect) along with their gap energies, their crystal structures and their lattice constant. It is worth mentioning that II-VI semiconductor materials encompass a large region of the electromagnetic spectrum from near infrared (CdTe) to ultraviolet (MgO) and they exist over a wide range of lattice constants. This particular feature is advantageous when a heterostructure epitaxial growth is considered since there will be a wide selection of materials for a substrate. Thus, lattice misfit effect between the substrate and the film could be minimised.

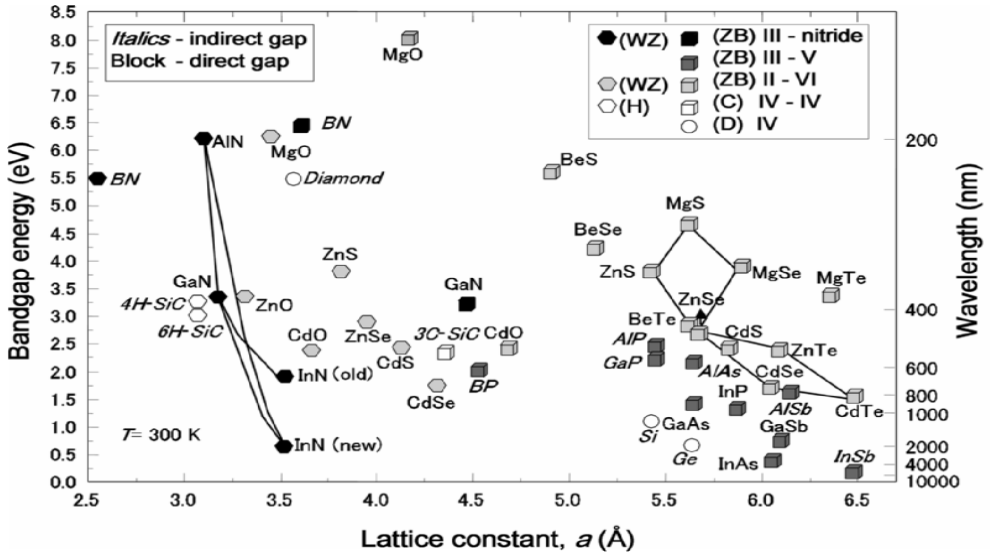

Figure 1.1 The energy gap, the lattice constant and the crystal structure at room temperature of different wide-gap semiconductors.[1]

In this work ZnO (a well-known wide gap semiconductor) was considered. A series of nominally pure and intentionally doped ZnO thin films with trace amounts of rare earth ions were fabricated by means of the pulsed laser deposition technique and spectroscopically and structurally investigated. Aims and motivations behind this work are discussed next.

1.1Aims and motivations

The underlying aim of the work undertaken in this thesis is threefold. Primarily, to successfully manufacture dense ceramic targets from the required raw material by finding the appropriate procedure using a hydraulic compression method and sintering process. Secondly, to use these targets to produce a series of high quality nanostructured thin films of ZnO doped with europium and erbium ions at a variety of nominal concentrations using the pulsed laser deposition technique (PLD). Lastly, to study and characterise the grown films by using different investgation techniques.

Doping rare earth (RE) atoms into a variety of solid state hosts has been receiving increasing research attention in the last decades, as this could fulfil the industrial demand for highly efficient fluorescent materials required for many important applications such as photonic devices and next-generation electronics.[5] RE elements are commonly chosen as promising optical dopants owing to their characteristic optical features. For example, the 4f-4f intra-shell transitions of the trivalent RE ions are considerably sharp (typically <5 nm) linewidth and hence require no colour filtering. The sharpness of these transitions is because the 4f electrons are electrically shielded by the electrons of the closed outer shells 5s and 5p. RE ions exhibit long luminescence lifetimes, typically 100 μs to 1 ms, and they cover a wide spectral range from vacuum ultraviolet (VUV) to infrared (IR).[6]

Furthermore, RE^{3+} ions embedded in a crystal can be used as optical probes to spectroscopically investigate the host crystal. The absorption and emission spectra due to inner shell f-f transitions are sensitive to the local symmetry of the host crystal which results in different spectral characteristics. Therefore, different optically active centres due to different site symmetries can be identified.[7, 8]

Interestingly, it has been demonstrated that the intensity of the intra-4f-configurational emissions of RE ions embedded in narrow bandgap semiconductors decreases substantially as the temperature increases due to the thermal quenching effect which is a major issue that prevents the use of smaller to moderate bandgap material to host RE ions. In contrast, using wide bandgap semiconductors was found to enhance the luminescence efficiency and to increase the intensity of the RE emissions even at room temperature.[9]

Moreover, doping RE ions into nanocrystalline semiconductors can improve the efficiency of the RE-related luminescence due to a sensitising effect via the typical intrinsic excitonic recombinations of the host matrix. Thus, extensive studies have been carried out in the hope that a RE-based material serving as an efficient light source could be successfully synthesised.[10-12]

In this thesis ZnO was considered for the following reasons: ZnO is a direct wide bandgap semiconductor possessing a number of remarkable optical, chemical and electrical properties. The wide range of its properties provides great amenability to be a suitable candidate for a variety of potential applications. It is an environmentally friendly material and is known to be mechanically, chemically and thermally robust.[13] ZnO emits UV radiation and has high transmittance to visible light, allowing RE-related visible and infrared luminescence. This important feature is valuable for making

efficient RE-based light sources that can simultaneously emit in different spectral regions.[14]

Large and high quality wafers of ZnO bulk crystal can be commercially obtained at a reasonable price in comparison to the price of its main competitor GaN. Using a high quality ZnO bulk wafer as a substrate for homoepitaxial growth is important to minimise serious residual stress created by lattice misfit and the difference in coefficient of thermal expansion between the substrate and the grown material. For electronic applications, ZnO has a large saturation velocity (3.2×10^7 cm/sec) and a high breakdown electrical field (2×10^6 V/cm) which is approximately twice greater than the breakdown field of GaAs.[15] ZnO demonstrates an excellent non-linear voltage-current relation. Such (V-I) characteristic is widely utilised in electrical surge protection devices so-called varistor. The non-ohmic behaviour is mathematically expressed by the following empirical equation [16]

$$A = \left(\frac{V}{V_b}\right)^{\alpha} \qquad (1)$$

where α is known as non-linearity parameter, V_b is a constant called breakdown voltage (or varistor voltage). V_b is mainly affected by the microstructure changes such as grain sizes and their numbers. Such changes can be greatly altered by mixing additives with varistor materials. For example, the majority of commercial ZnO-based varistors contain some additives such as Bi_2O_3 Al_2O_3 and Sb_2O_3.[17-20] ZnO is amenable to the conventional wet chemical etching process used in device fabrication in typical Si technology, which helps in reducing the material cost. This is a very important key advantage over GaN semiconductor for which reactive ion etching is utilised.[21, 22] The surface conductivity of ZnO thin film is

highly sensitive to adsorb species which makes ZnO a good candidate for gas sensors.[23]

By far the most beneficial feature of ZnO is that it has the largest exciton binding energy (60 meV) in comparison to all other semiconducting materials belong to II-IV and III-V groups. Figure 1.2 shows the exciton binding energy (E_{ex}) for various materials with different gap energies (E_g). The exciton binding energy is defined as the amount of energy needed to dissociate the exciton into a free hole and a free electron. The exciton binding energy of ZnO is about 2.4 times greater than the thermal energy (k_BT=25 meV) at room temperature (RT). This particular feature indicates that the electron-hole pair (exciton) is strongly bound and thus less likely to be thermally dissociated, which would ensure excitonic emission can be obtained at RT. This is an essential requirement for a stable performance operation of a ZnO-based device at and above room temperature.[23] Interestingly, a ZnO-based laser action has been successfully stimulated by excitonic emission at RT.[24]

ZnO is exceptionally resistant to damage when exposed to high energy radiation. When a semiconductor is irradiated by a high energy source, deep centres are formed in the forbidden energy gap which negatively modify the device sensitivity, response time and noise level. The superior radiation hardness of ZnO makes it a very useful material for space applications.[15]

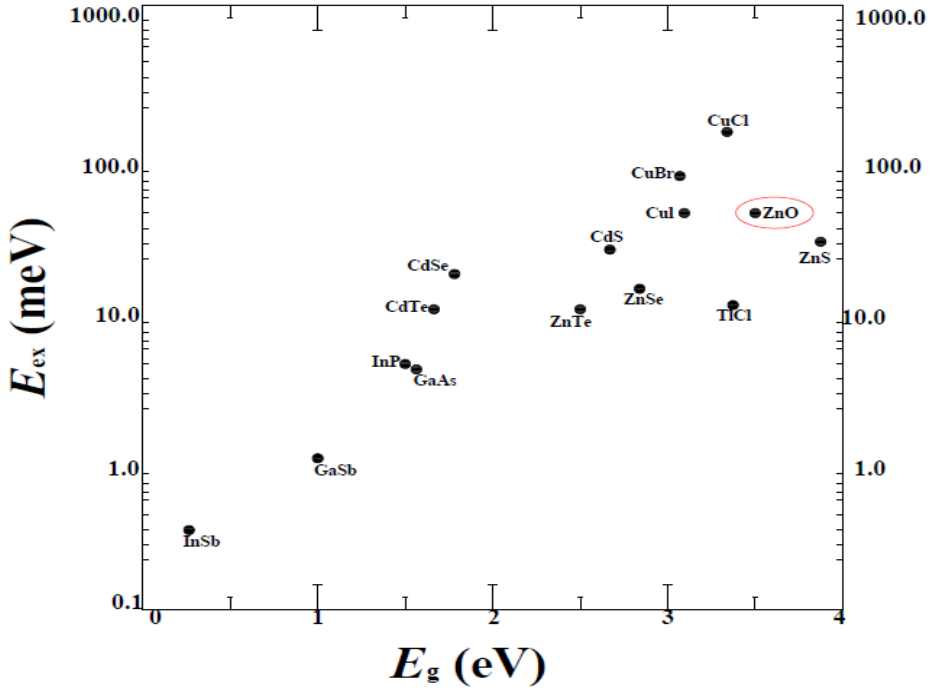

Figure 1.2 The exciton binding energy as a function of bandgap energy of various semiconductors.[25]

The trivalent europium (Eu^{3+}) ion is widely regarded as an attractive optical dopant capable of emitting strong orange/red light between 540 and 665 nm and ZnO is considered as a green/blue and UV/violet semiconductor phosphor.[26, 27] Therefore, incorporating Eu ions into ZnO is expected to produce different visible emissions in different spectral regions which are important for many promising industrial applications such as display monitor, optical communications, X-ray imaging and solar cells and lasers.

Erbium (Er) is an essential element in the field of optical communication systems because of its intra-4f shell luminescence emission in the infra-red region at approximately 1.54 μm. At this particular wavelength the commonly used silica-based fibre optic has minimum loss, nearly zero dispersion and maximum transparency. However, Er-doped silicon suffers from a thermal quenching effect which prevents effective use of this

emission. Therefore, ZnO has been used to host Er atoms in order to enhance the Er-related emission especially at higher temperatures.

At nanometre dimensions, the physical properties of the host matrix could be considerably different from its bulk counterpart. For example, optical properties are dependent on the shape and the size of the nanocrystal. Furthermore, the synthesis method and the imbalance in size and charge between the incorporated RE ion and the ions of the host matrix are expected to induce structure distortion, various defects and residual stress. These unwanted effects may influence the structural and luminescent properties of both the optically active dopants and the host material. Therefore a clear understanding of the structural and optical properties of these materials is very important and a prerequisite which will hopefully determine their usefulness in advanced technological applications.

1.2Zinc Oxide: its physical properties and applications

In spite of the fact that ZnO is not a newly discovered semiconductor, it has been sparking a growing attention among the scientific community, which is evident by the numerous relevant publications, conferences and workshops related to zinc oxide material. ZnO was discovered in 1810 by Bruce in Franklin (New Jersey, USA) and since then it has been commercially the most important chemical compound of zinc element.[28] Zinc and oxygen elements are abundant in nature. The earth's crust contains about 132 ppm of Zn and 49.4 % of O.[28] This is an important factor in reducing the cost of ZnO large-scale production. ZnO is an intrinsic n-type and direct wide-gap semiconductor with a bandgap energy of 3.37 eV at RT.

ZnO crystallises in either a cubic zinc-blend or, preferentially in a wurtzite structure with a symmetry point group 6 *mm* and space group $P6_3mc$ where

the lattice has a hexagonal unit cell as depicted in Figure 1.3 Each unit cell consists of two ZnO molecules. The zinc-blende structure is a metastable phase which can only be realised by epitaxial growth on a zinc-blende type wafer such as GaAs(100) with a ZnS buffer layer.

At ambient conditions, the wurtzite structure has the following lattice constants $a = b = 0.3249$ nm and $c = 0.52042$ nm giving a $c:a$ ratio (1.602) lower than the value of 1.6333 for perfectly hexagonally closed-packed (hcp) atoms. In the ZnO hexagonal unit cell, every oxygen atom is tetrahedrally coordinated with four zinc atoms and vice versa. However, the tetrahedron is slightly distorted since the Zn-O bond length (0.196 nm) along the c axis is a bit smaller than the other three oxygen atom bonds (0.198 nm).[28]

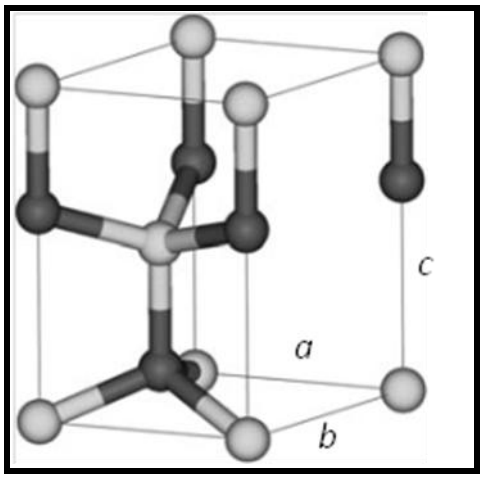

Figure 1.3 The primitive unit cell of hexagonal wurtzite ZnO. The grey spheres represent oxygen atoms while the dark ones correspond to zinc atoms.

The wurtzite lattice has no inversion symmetry and is composed of two interpenetrating hexagonal closed-packed (hcp) sublattices, one containing the anions (O^{2-}) and the other the cations (Zn^{2+}). These sublattices are displaced from one another by 3/8 along the *c*-axis. Therefore, the ZnO crystal exhibits crystallographic polarity along the *c*-axis due to the lack of

inversion centres [29]. Cleaving ZnO normal to the *c*-axis would result in two different polar surfaces either O-polar or Zn-polar surface. In the case of the O-polar face the surface is terminated by oxygen atoms whereas the Zn-polar surface is terminated by zinc atoms. The opposite polarity gives rise to a net dipole moment causing spontaneous electrical polarisation. As a result of the non-centrosymmetric crystal structure and the polarity, ZnO possess ferroelectric and high piezoelectric properties.

Types of chemical bond are quantitatively identified by measuring their iconicity. In ZnO owing to the tetrahedral coordination nature of its lattice the Zn and O atoms are expected to exhibit a typical covalent bond (sp^3). However, the Zn-O bond has a substantial fraction of ionic bonding with iconicity value of 0.616 on the Philips ionicity scale, which is caused by the very strong electronegativity of oxygen atoms (about 3.5 on the Pauling scale).[30] Thus, zinc and oxygen in ZnO may well be regarded as ionised Zn^{2+} and O^{2-}. The ratio between its iconicity and covalencey is 39%.[31] Therefore, ZnO lies on the borderline between being considered as a covalent or ionic semiconductor. The ionic radii of Zn^{2+} and O^{2-} are 0.074 and 0.140 nm, respectively.[30]

Another characteristic feature of the ZnO lattice is that it is relatively empty due to only 44 % of its volume being occupied by the oxygen and zinc atoms while 56 % of the volume is still open. This means other atoms such as intrinsic impurities can be incorporated into the lattice especially at high temperatures, distorting the crystal structure, which may lead to notable changes in its physical properties.[32]

At 300 K the thermal expansion coefficients of ZnO (wurtzite) crystal, which largely depend on the direction are, 2.9×10^{-6} K^{-1} along the c-axis and 4.7×10^{-6} K^{-1} perpendicular to c-axis.[30] It is difficult to obtain precise figures for the electrical properties of ZnO mentioned in the literature due

to the big variance of the sample quality. However for p-type doping, hole concentrations in the range of 10^{17} cm^{-3} [24] have been increasingly cited while the largest reported electron concentration for n-ZnO is ~10^{21} cm^{-1}.[33]

The optical properties of a material are strongly influenced by the energy band structure and the lattice structure. Thus, an accurate knowledge of the electronic band structure of a given crystalline semiconductor is very important in understanding the optical properties. The band diagram for wurtzite ZnO at the Brillouin Zone centre where k=0 (Γ-point) is schematically shown in Figure 1.4 The valance band is triply degenerate due to the crystal field and the spin-orbital interactions and these three sub-bands are labelled A, B and C. However, the band structure of pure ZnO is anomalous compared to the other II-VI wurtzite semiconductors. The symmetry of the electron wavefunctions in the A valance sub-band remains controversial despite the fact that several theoretical and experimental studies have been carried out. Thus, the correct ordering of the valance sub-bands is not yet fully clear.[33]

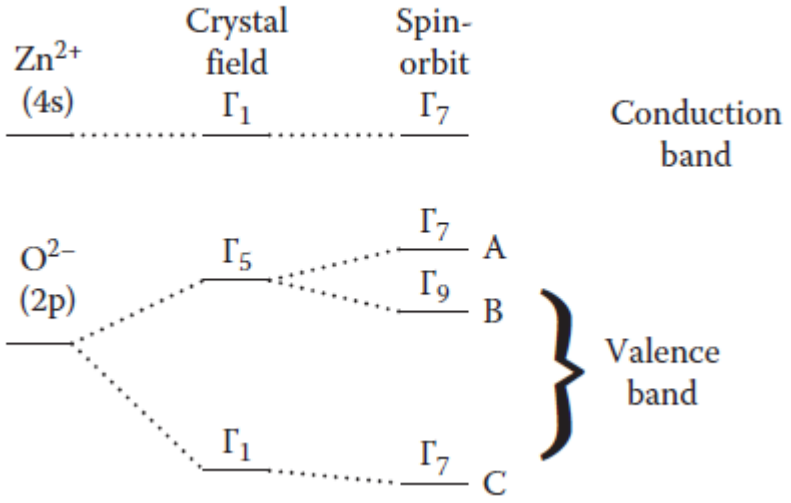

Figure 1.4 Schematic diagram of ZnO band structure along with band symmetries.

Typical low-temperature luminescence spectra of nominally undoped ZnO bulk crystals have been extensively investigated and well documented in the literature by many researchers for more than 40 years .[30] The spectrum is richly composed of many excitonic features which are dominated by donor bound exciton recombinations since ZnO is an intrinsically n-type semiconductor and other optical features. These optical emissions are summarised in Table 1.1 where some associated optical centres have been chemically identified for some of the photoluminescence (PL) emission peaks. The physical concept of these different optical emissions is discussed in Chapter three.

Table 1.1 PL excitonic recombinations commonly seen in bulk ZnO at 4.2 K. E_{loc} is the bound exciton localisation energy with reference to the transverse free A-exciton energy. E_D refers to the donor binding energy. (D^o,X) and (D^+,X) stand for neutral and ionised donor bound excitons respectively.[33]

Peak	***E*** (eV)	$\boldsymbol{E}_{loc}$ (meV)	$\boldsymbol{E}_D$ (meV)	**Chemical identity**
A_L	3.3785			A_L free exciton-polariton (longitudinal)
A_T	3.3765			A_T exciton-polariton (transverse)
I_0	3.373	3.5	54.5	(D^+,X)—aluminum
I_1	3.3724	4.1	56.7	(D^+,X)—gallium
I_2	3.3674	9.1	66.9	(D^+,X)—indium
I_3	3.3665	10.0	—	(D^+,X)—unknown donor
I_4	3.3628	13.7	50.2	(D^0,X)—hydrogen
I_5	3.3614	15.1	54	(D^0,X)—unknown donor
I_6	3.3612	15.3	54.5	(D^0,X)—aluminum
I_7	3.3607	15.8	55.9	(D^0,X)—unknown donor
I_8	3.3604	16.1	56.7	(D^0,X)—gallium
I_{8a}	3.3598	16.7	58.3	(D^0,X)—unknown donor
I_9	3.3566	19.9	66.9	(D^0,X)—indium
I_{10}	3.353	23.5	76.7	(D^0,X)—unknown donor
I_{11}	3.3519	24.6	79.6	(D^0,X)—unknown donor

A PL spectrum of a bulk ZnO crystal obtained from ZN Technology Inc. (previously Eagle-Picher) in USA was recorded at 4 K and is shown in Figure 1.5. In addition to the numerous near band edge excitonic features, a non-excitonic broad green luminescence was detected. This broad emission is commonly observed in ZnO and wide-gap semiconductors where its origin is still not definitely discovered.[34-36] The high resolution spectrum of the excitonic region is depicted in the inset. The crystal was grown at 2000 ^oC by the seeded chemical vapour transport pressurised melt method.[28]

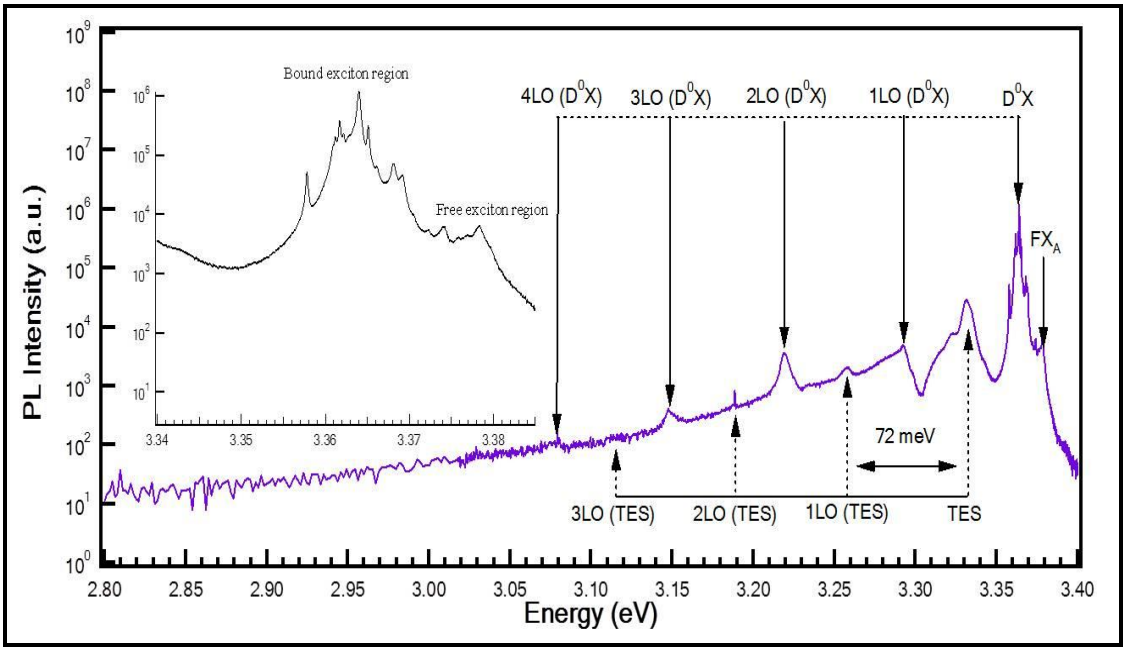

Figure 1.5 Low temperature PL spectrum of a ZnO bulk crystal excited by a He-Cd laser. A high resolution spectrum of near band edge is shown in the inset. Two-electron satellites (TES) transition and longitudinal optical phonon (LO) replica are also observed.

The notation I_x, as shown in table 1.1, used to label the excitonic recombination of ZnO has been adopted historically in many excitonic materials where the subscript x takes number from 0 to 11. Other secondary spectral features are commonly seen in ZnO PL spectrum. TES stands for two-electron satellites transition while LO refers to longitudinal optical phonon replica. These secondary features are explained in details in Chapter three.

Even though ZnO has been investigated for many years, some essential issues related to its conductivity and optical properties are still not well understood. For example, no concrete conclusion has been established for the assignment of various sharp emissions seen in the photoluminescence spectrum. Also, the real cause of the residual n-type conductivity in nominally undoped ZnO remains a formidable challenge. Consequently, producing a reproducible and satisfactorily stable p-type ZnO thin film with

low resistivity has not yet been realised. Moreover, the growth of large-area and high quality heteroepitaxial ZnO layers is still a problematic issue.

Despite the previously mentioned obstacles, n-type ZnO can still be utilised in many important applications. It has been demonstrated that ZnO can be efficiently used as a piezoelectric transducer, a low voltage varistor and an acoustic element. ZnO exhibits high optical transparency in the visible range and therefore it can be exploited as a window material in solar cells. Furthermore, great attention has been focused on making high quality ZnO-based heterostructure devices such as LEDs and ultraviolet photodetectors (PD) where the p-type junction is obtained from other materials like GaAs, Si or GaN. ZnO films have also been doped with transition-metal atoms (Mn, Co, Ni, etc.) which will introduce local magnetic moments into the lattice and hence dilute magnetic semiconductors could be obtained and used as spin injectors in spintronic devices.

1.3 Rare earth elements

This subsection will be mainly devoted to giving an overview of the rare earth (RE) elements, their properties and some of their novel applications. The term “RE” refers to a group of chemically similar metallic elements that occur naturally. Their chemical similarity comes from the fact that they have the same number of electrons in their outer atomic shell so they behave in a similar way during a chemical reaction. Interestingly, they are relatively abundant in the Earth's crust and available in larger quantities than silver, gold and platinum. In fact, they are not found as pure metals but they inevitably exist in minerals as mixtures of different REs and strikingly behave as a single chemical entity. Furthermore, they are extremely difficult to chemically separate from one another; hence the word “rare” was adopted to refer to such difficulty in extracting pure RE elements.

As a result of such difficulty the discovery of all REs took nearly 160 years (from 1788 to 1941) to be completed. In fact, prior to 1945 long and tedious processes were required to purify the metals from their oxides.[37] However, ion-exchange and solvent extraction methods are currently used to produce highly purity (99.999 % pure) and low-cost RE elements.[37] The main significant resources to produce REs are bastnaesite, monazite and xenotime ores. Figure 1.6 shows typical pictures of two of these ores. China and the United States are believed to have the largest economic resources in the world for REs.[38]

Figure 1.6 Typical pictures of two rare earth ores.[38]

The rare earth elements can generally be divided into two series, as shown in Figure 1.7, where each series consists of fifteen elements, namely lanthanides and actinides. Interestingly, RE elements are characterised by the successive filling of their incomplete 4f and 5f shells. The lanthanides start with the element lanthanum which has the atomic number (Z= 57) and it ends with the element lutetium (Z=70). The actinide group which is identified by the progressive filling of the 5f-shell begins with actinium (Z=89) and end with element lawrencium (Z=103). The name of lanthanide was derived from the Greek word lanthano which means hidden.[39] In this thesis two elements europium and erbium, belonging to the lanthanides

series are used. Thus discussion will be only focussed on the lanthanide elements. Hence, whenever the RE term is mentioned we shall always mean the lanthanide elements.

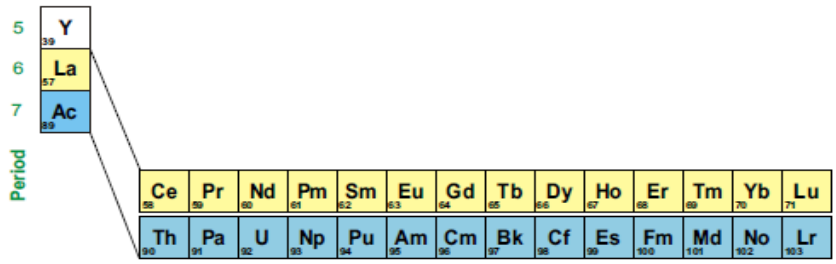

Figure 1.7 Rare earth elements.

In theory, elements are identified by their atomic number. The higher the atomic number, the greater the number of electrons orbiting in shells around the nucleus. Normally, the average radius of an atomic shell gradually increases as more electrons are added to it. In contrast, as one goes along the lanthanide series from the smaller to the bigger atomic number a steady decrease in the size of atoms and ions is observed. This phenomenon is called the lanthanide contraction.[37, 39] Such reduction of the $4f^n$ shell is ascribed to the imperfect screening of one 4f electron by another 4f electron because of the shape of the orbital. As the number of 4f electrons successively increases by one at each element the nuclear charge rises as well. As a result the effective nuclear charge experienced by the 4f electrons increases due to poor shielding and hence the 4f electrons tend to be more and more firmly bound to the nucleus causing a reduction in the size of the 4f shell.[37, 40, 41]

Another impressive physical feature of the RE elements is that when RE atoms are intentionally embedded into a crystal, the magnitude of the crystal field effect on the RE ions is relatively small, since the 4f electrons are relatively “well screened” from external fields by the two closed outer

electronic shells $5s^2$ and $5p^6$ which have larger radial extension than the 4f shell. Therefore, the spectra of RE ions are richly composed of narrow lines due to intra-4f transitions similar to those commonly observed in the spectra of (free ions) gases. Also, RE ions have a large number of accessible states in the ground and the first excited configurations, producing many emissions over a wide spectral range. Thus, RE ions are widely accepted as optically efficient luminescent candidates. It is known that RE elements are strongly reactive and can be easily oxidised when exposed to air. By far, the most common stable valance state of the majority of RE elements in solids is the trivalent state.[39, 42]

The electronic configuration of an atom belonging to the RE series, in its ground state, is [Xe] $4f^n$ where [Xe] represents the electronic configuration of the xenon atom and *n* is the number of electrons in the incompletely filled f shell. For a free RE ion, (vapour phase) various atomic forces such as the columbic repulsion and spin-orbit coupling between 4f electrons will split the original $4f^n$ configuration into several electronic states. Typically, in many-electron atoms approach, these states can be described using the Russell-Saunders (spin-orbit) coupling scheme where each electronic state is called J-multiplets (or J-mainfolds) and conventionally labelled by a spectroscopic symbol, $^{(2S+1)}L_J$, where S and L are the total spin angular momentum quantum number and the total angular momentum orbital quantum number respectively. The vector sum of the orbital angular momentum of all 4f electrons yields the L number and S can be similarly calculated. J is the total angular momentum quantum number which is obtained by vectorially adding L to S. *l* can take the values of 0 to n-1 while *s* can be denoted by an arrow pointing up, which is +1/2, or an arrow pointing down, which is -1/2. The (2S+1) term is the so-called the spin multiplicity since there are (2S+1) degenerate levels in each electronic state where the states having S = 0 are referred to as singlets while states with

S=1 are known as triplets. States with L= 0,1,2,3,4,5 are spectroscopically denoted by letters S, P, D, F, G, F. For example, the ground state of Er^{3+} is denoted by $^4I_{15/2}$ which means S = 3/2, L = 6 and J equals 15/2. Table 1.2 shows the values of S,L,J of some RE^{3+} ions in their ground state.

Table 1.2 Electronic configuration of some RE ions in their ground state.

Ion	Number of electrons (n)	$S = \sum_{i=1}^{n} s_i$	$L = \sum_{i=1}^{n} l_i$	$J = L - S$ (if n < 7) $J = L + S$ (if n ≥ 7)
Ce^{3+}	↑	1/2	3	5/2
Pr^{3+}	↑ ↑	1	5	4
Nd^{3+}	↑ ↑ ↑	3/2	6	9/2
Pm^{3+}	↑ ↑ ↑ ↑	2	6	4
Sm^{3+}	↑ ↑ ↑ ↑ ↑	5/2	5	5/2
Eu^{3+}	↑ ↑ ↑ ↑ ↑ ↑	3	3	0
Gd^{3+}	↑ ↑ ↑ ↑ ↑ ↑ ↑	7/2	0	7/2
Tb^{3+}	↑ ↓ ↑ ↑ ↑ ↑ ↑ ↑	3	3	6
Dy^{3+}	↑ ↓ ↑ ↓ ↑ ↑ ↑ ↑ ↑	5/2	5	15/2
Ho^{3+}	↑ ↓ ↑ ↓ ↑ ↓ ↑ ↑ ↑ ↑	2	6	8
Er^{3+}	↑ ↓ ↑ ↓ ↑ ↓ ↑ ↓ ↑ ↑ ↑	3/2	6	15/2

However, when a RE atom is placed in a chemical environment such as a crystal (ordered structure) or a glass (amorphous) the spherical symmetry of the local structure, that the free RE ions possess, will be disturbed due to the crystal field (i.e. electrostatic field of the atomic arrangements) and hence the energy of these free-ion atomic states will be slightly shifted and

split further into a number of states depending on the site symmetry of the ions inside the host matrix. These induced electronic states are called Stark levels. Figure 1.8 shows a simple schematic representation of the splitting of the $4f^n$ electronic configuration.[39]

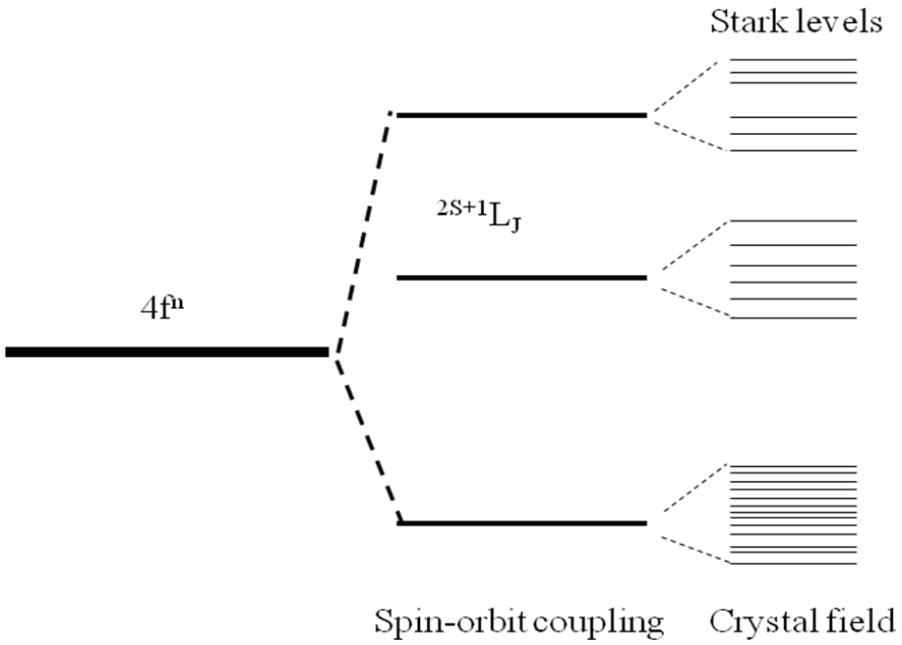

Figure 1.8 Schematic drawing of the splitting of the $4f^n$ state of a free RE ion when inserted into a crystal.

In theory, the 4f-related transitions between 4f multiplets are strictly forbidden for electric dipole radiation because of Laporte's selection rule which requires the parity of the wave function of the initial state and the final state to differ. However, experimentally a 4f electron can be easily excited within the 4f states and 4f-related transitions are observed. Such unexpected observation leads to what is known as "the puzzle of the 4f electron optical spectra". Actually, the 4f states are not perfectly shielded by the closed $5s^2$ and $5p^6$ shells, so when RE ions are incorporated into crystals they are weakly affected by the electric fields produced by the surrounding ions and therefore will experience to some extent an inhomogeneous electrostatic field, the so-called static crystal field,

produced by the charges of the surrounding ligands such as atoms, molecules, radicals or ions.[39]

In addition, the RE ions interact with the crystal lattice vibrations (known as phonons) due to the dynamic crystal field which is induced by shifting the neighbouring ions from their equilibrium positions and alter the electrical field experienced by the RE ions. Consequently, these perturbation factors will cause some higher states having different parities to be mixed up with the 4f states making admixtures of states that will permit 4f-related transitions to take place. Such types of transitions are called electric dipole forced transitions.[39]

The magnetic properties of rare earth ions are determined by the unpaired electrons of the f shell. In general at room temperature all RE elements apart from scandium, yttrium, lanthanum, ytterbium and lutetium are strongly paramagnetic. However, some RE elements exhibit antiferromagnetic behaviour at low temperatures and upon further cooling they become ferromagnetic. RE elements are magnetically anisotropic materials which means their magnetic properties depend on the direction in which they are measured. Electrically, RE materials exhibit poor conductivity and also their resistivity varies due to their anisotropic character.[37]

The optical properties of RE ions are dominated by the radiative transitions within the 4f manifolds. As a result, a great deal of research has been carried out by many scientists to investigate the RE-related transitions. For example, Dieke and co-workers[43] have intensively investigated the optical transitions of different trivalent lanthanide ions embedded into lanthanum chloride ($LaCl_3$) bulk crystals and provide us with a very useful energy level diagram which shows the energy of the different $^{(2S+1)}L_J$ states for various RE^{3+} ions. The relative positions of the low-lying 4f energy levels

of trivalent lanthanides ions are shown in Figure 1.9. Although Dieke's study was based on systematic spectral measurements of RE ions incorporated into a specific crystal it can still be reliably used as a good qualitative description to study the energy levels of RE ions in most crystals. This assumption can be rationalised as follows: since the effect of the crystalline field is weak due to the electrostatic shielding effect when the RE ions are incorporated into crystals the spin-orbit interaction between the 4f electrons themselves is dominant with its value largely independent of the host matrix. Thus, the energy levels of the 4f states of RE ions are slightly perturbed and the gross optical features of RE ions in most solids are expected to be similar to those of the free ions.[39, 42]

Many important RE-related applications ranging from high-technology to medicine and health rely principally on the novel physical and chemical properties of RE. For example, the localised $4f^n$ to $4f^n$ transitions are responsible for the unique optical properties of RE ions which are key components in optical fibres, data storage, high laser power systems, display monitors, energy efficient fluorescent light bulbs, phosphor-based light-emitting diodes and medical imaging.[37, 38] They also play a significant role in high-tech digital products that surround us in our daily lives like audio-visual equipment, photographic and communication devices.[37-39] Furthermore, RE elements contribute greatly to the fast growing field of green energy technology which aims to limit green house gas emissions. In this technology, RE elements are key factors in producing hybrid and electric vehicles and wind power generators, hence minimising hydrocarbon consumption.[44] RE elements are also used as catalysts in the petroleum refining process. They are capable of producing strong permanent magnets that are useful in a wide range of applications. Therefore, RE elements are increasingly considered indispensable and non-replaceable materials.

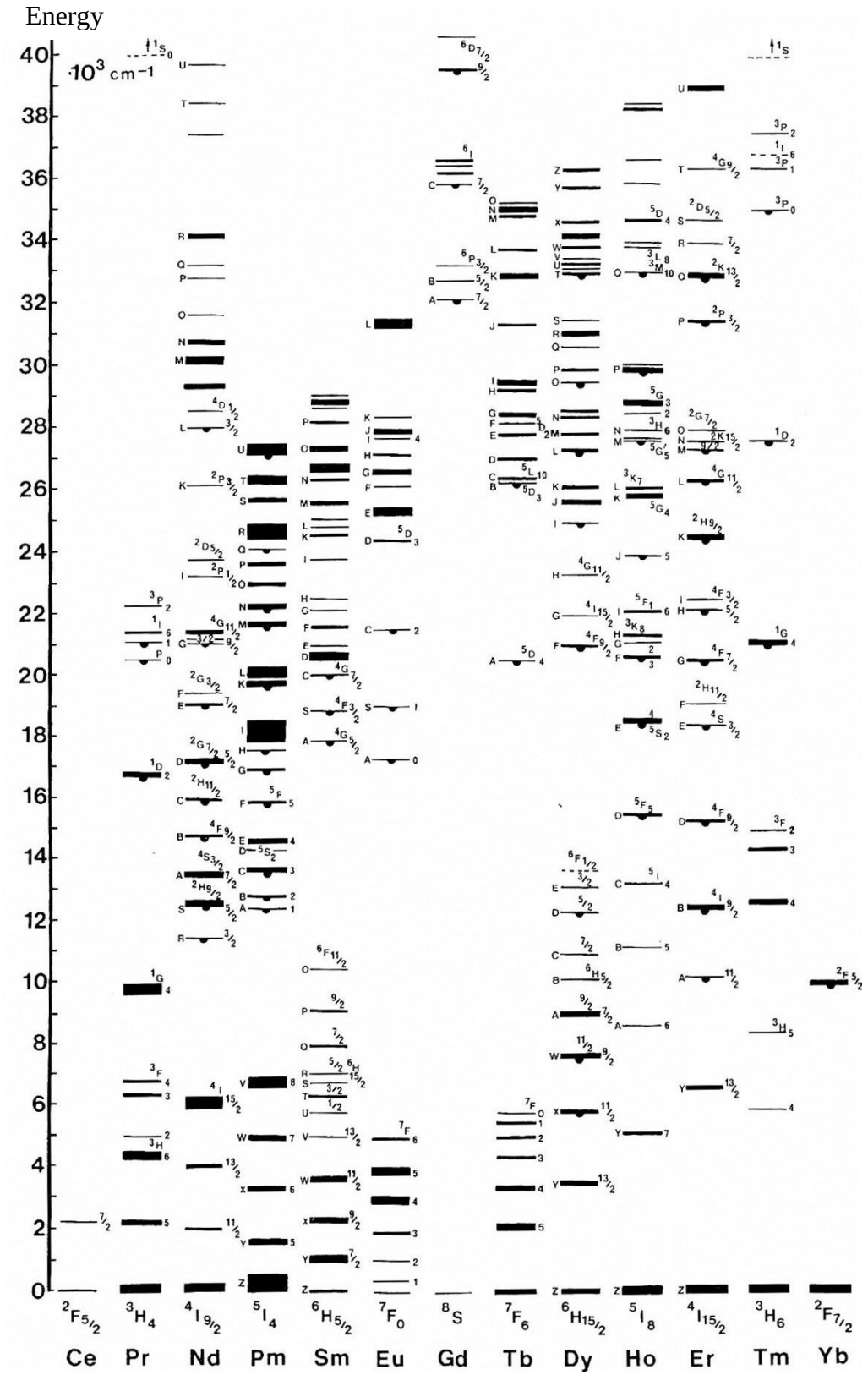

Figure 1.9 An energy-level diagram, known as Dieke diagram, for trivalent lanthanide rare earth ions incorporated into lanthanum chloride ($LaCl_3$) crystal.[43]

1.4Europium

Europium (Eu) is present in the Earth's crust at an average concentration of 1 part per million. Eu is a silvery-white ductile metal [45], typically produced by metallothermic reduction of the oxide. A picture of pure metallic europium is displayed in Figure 1.10 In 1901, Eugène-Anatole Demarçay, a French chemist and geologist, discovered the europium element. It was named europium, after the continent of Europe where the element was first found.[37, 46] In 1964 a new Eu^{3+}:YVO_4, red-emitting phosphor was developed and successfully used to produce the first true red colour in television screens.[47] Eu is considered the most chemically reactive element, hygroscopic, among the lanthanides series where it readily reacts with water to produce hydrogen. It is commonly used as an activator, effective emitter, and as a probe dopant in many host materials to study their optical properties. Table 1.2 summarises some of its physical and chemical properties.

Figure 1.10 Typical picture of pure europium element.[38]

Table 1.3 Some physical and chemical properties of europium.[37]

Symbol	Eu
Atomic number (Z)	63
Density (g/cm^3) @ 24 ^{o}C	5.244
Atomic mass (amu)	151.965
Atomic volume (cm^3/mol) @ 24 ^{o}C	28.979
Melting point (^{o}C)	822
Boiling point (^{o}C)	1597
Coefficient of thermal expansion (^{o}C^{-1})	35.0×10^{-6}
Thermal conductivity W/(cm.K)	0.139
Electrical resistivity (μΩ/cm)	90.0
Electronegativity of Eu^{3+} ion	1.152
Natural isotopes	Eu-151 and Eu-153
Crystal structure	Body-centered cubic (bcc)
Ionic radius (3^+) (Å)	0.95
Electronic configuration of Eu atom	$4f^7 5s^2 5p^6 6s^2$

1.5Erbium

In 1843 Carl Gustav Mosander, a Swedish scientist, discovered the erbium (Er) element. It is a shiny silvery white metal, as shown in figure 1.11 which can be extracted from various sand ores such as Monazite and Xenotime. It is estimated that the average concentration of Er in the Earth's crust is about 3 parts per million by weight. In contrast to Eu, element Er is considered to be fairly reactive when exposed to air. Table 1.3 outlines some physical and chemical features of Er.

Figure 1.11 A picture of pure erbium metal.

Table 1.4 Some physical and chemical properties of erbium.[37, 45]

Symbol	Er
Atomic number (Z)	68
Density (g/cm^3) @ 24 ^{o}C	9.066
Atomic mass (amu)	167.26
Atomic volume (cm^3/mol) @ 24 ^{o}C	18.449
Melting point (^{o}C)	1529
Boiling point (^{o}C)	2863
Coefficient of thermal expansion (^{o}C^{-1})	12.2× 10^{-6}
Thermal conductivity W/(cm.K)	0.145
Electrical resistivity (μΩ/cm)	86.0
Electronegativity of Eu^{3+} ion	Er-162, Er-164, Er-166, Er-167, Er-168, Er-170
Crystal structure	Hexagonal close-packed (hcp)
Ionic radius (3$^+$) (Å)	0.89
Electronic configuration of Eu atom	4f^{12}5s^{2}5p^{6}6s^2

Er ions have several important uses in a variety of technological fields. For example, in the optical communication systems, Er-doped fibre amplifiers have been used. Er can efficiently emit at 1.5 μm due to the transition from its first excited state to the ground state. Interestingly, at this particular wavelength the commonly used silica-based fibre optic has minimum loss, nearly zero dispersion and maximum transparency, thus Er ions are considered as an important component to successfully amplify high frequency telecommunication signals. Moreover, lasing of Er ions when doped into aluminium garnet (Er:YAG) is safely and popularly used by dermatologists for skin treatments.

Chapter 2

TARGET PREPARATION AND THIN FILM GROWTH

A successful growth of high quality thin films using the pulsed laser deposition (PLD) technique basically requires high density targets to largely eliminate the commonly observed micron-sized particulates during the ablation process. These particulates are ejected from targets due to the high intensity laser pulse and are believed to seriously degrade the optical properties of the grown films.[48] Although high grade PLD targets are commercially available doped targets which are required to grow doped-thin films cannot be readily obtained from commercial sources at reasonable prices, especially if different concentrations of doping material are needed. Therefore, doped targets have to be locally manufactured by researchers.

The PLD targets are usually fabricated by thorough mixing of predetermined quantities of finely ground powders of the materials of interest and then compressing into pellets followed by a well-defined heat-treatment process called sintering. This chapter gives a full physical description of the sintering process, the exact fabrication method of the targets which was followed to produce the targets and the adopted growth procedure of the thin films. Furthermore, the physical principles as well as the advantages of using the PLD technique are discussed.

2.1What is sintering?

Sintering is technically referred to as a densification process where a solid body can be produced from compact powder (also known as *green body*) under appropriate conditions of applied pressure, temperature, particle size and the sintering environment. Such a process has been widely practiced for

thousands of years. For example, bricks were one of the first products to have been sintered in an open fire.[49] Many approaches have been suggested to effectively improve the sintering process. Such approaches involve different pressing techniques, adding chemical materials (known as binders) and performing different types of sintering methods (apart from conventional sintering) such as two-step sintering, spark plasma sintering...etc. The sintering operation is a crucial step to produce targets that are necessary to grow thin films by many deposition techniques such as PLD, magnetron sputtering and electron beam deposition (EBD).

The surface free energy of a compact powder forms the fundamental basis of the sintering process. This can be explained as follows: pressed powder is composed of many distinct particles where each one has its own surface area and hence the total surface area for the whole system is deemed high. If we consider one mole of powder composing of spherical particles with a radius r the number of particles will be:

$$N = \frac{3M}{4\pi r^3 \rho} = \frac{3V_m}{4\pi r^3} \qquad (2)$$

where ρ is the density of particles, M is the molecular mass and V_m is the molar volume. The total surface area of the powder system is

$$S = 4\pi r^2 N \qquad (3)$$

If γ is the surface energy per unit area (or surface tension of the particles) then the surface free energy included in the system is

$$E_{\gamma s} = \frac{3\gamma V_m}{r} \qquad (4)$$

If we assume $\gamma = 1$ J/m^2, $r = 1$ micron and $V_m = 25\times10^{-6}$ m^3 then $E_{\gamma s} = 75$J for only one mole of substance.[50] Thus the surface free energy is

considered a driving source of sintering. Minimising the surface energy leads to a more stabilised system and is widely accepted as the main driving force of the sintering process.[49-51]

As the compact powder is heated (thermally activated) the total surface area is reduced, by the creation of necks that weld the particles together, and consequently leads to the development of grain boundaries due to transport of matter by atomic diffusion. In reality there are several pathways that lead to mass transportation which are diagrammatically shown in Figure 2.1 They can be generally grouped into two main classes. Surface transport and bulk transport.[50, 51] The surface transport refers to those mechanisms where mass flow starts and ends on the particle surface such as surface diffusion and evaporation/condensation. Bulk transport includes all paths that lead to transfer of material from inside the compressed particles into the neck region such as volume diffusion, grain boundary diffusion and plastic flow. [50, 51]

Despite the fact that all transport mechanisms participate in the creation of the interparticle necks and hence the grain boundaries, some of these mechanisms will lead to densification (pore removal) whereas others will cause a non-densifying effect known as grain coarsening which provides an alternative way by which the system can reduce its free energy without densification. Coarsening is defined as rapid growth of grains and pores.[50] Both coarsening and densification occur simultaneously where the densification rate is considerably affected by the dominant operating mechanisms. Growth of grains occurs by the motion of the grain boundaries since the atoms located in the grain boundary possess more energy than those inside the grains.[50, 51] Since the total sum of the individual grain sizes must remain constant due to the conservation of matter some grains will grow at the expense of others (often the small ones). Coarsening (grain

growth) must be limited in order for a density high object to be attained.[49-51]

Grain boundary diffusion, volume diffusion and plastic flow cause pore removal and are hence called densifying mechanisms. In contrast, surface diffusion and evaporation/condensation process do not contribute to densification and are therefore called non-densifying mechanisms.

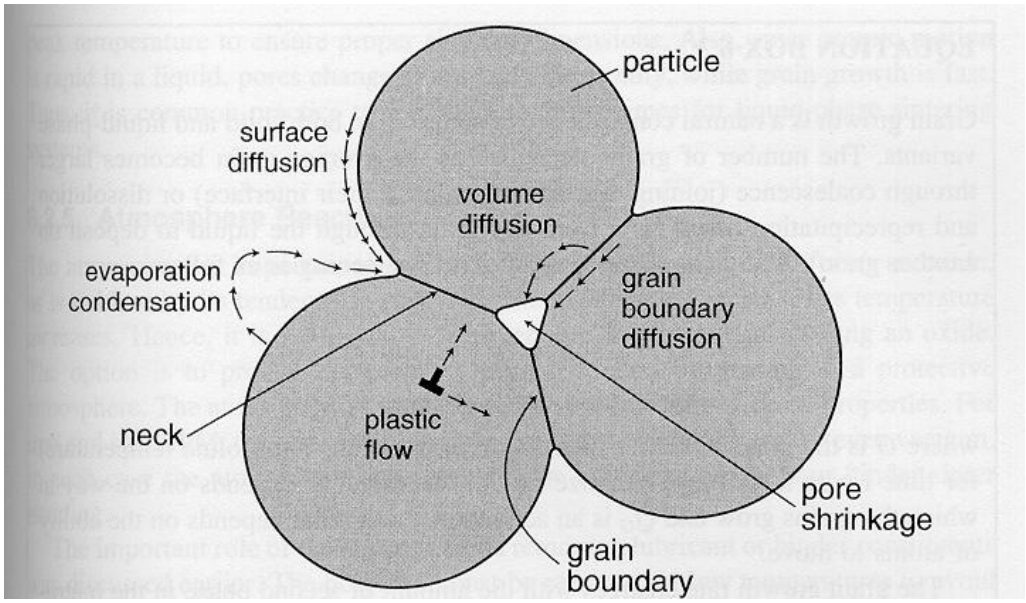

Figure 2.1 Schematic illustration showing different pathways (more precisely mechanisms) of mass transportation where ⊥ represents dislocations. [51]

As sintering is a fairly sophisticated physical process, scientists have been actively showing great efforts to gain a clearer understanding of such phenomenon. However, the sintering process can be reasonably well explained according to the overall microstructural (morphological) progression of the consolidated particles of powder during the sintering course as particles begin to combine together leading to a decrease in the porosity degree of the system. This evolution of microstructure can be split into three consecutive stages. These stages are schematically shown in

Figure 2.2 for idealised geometrical structures that, are widely accepted to give a descriptive explanation of these stages. [49-51]

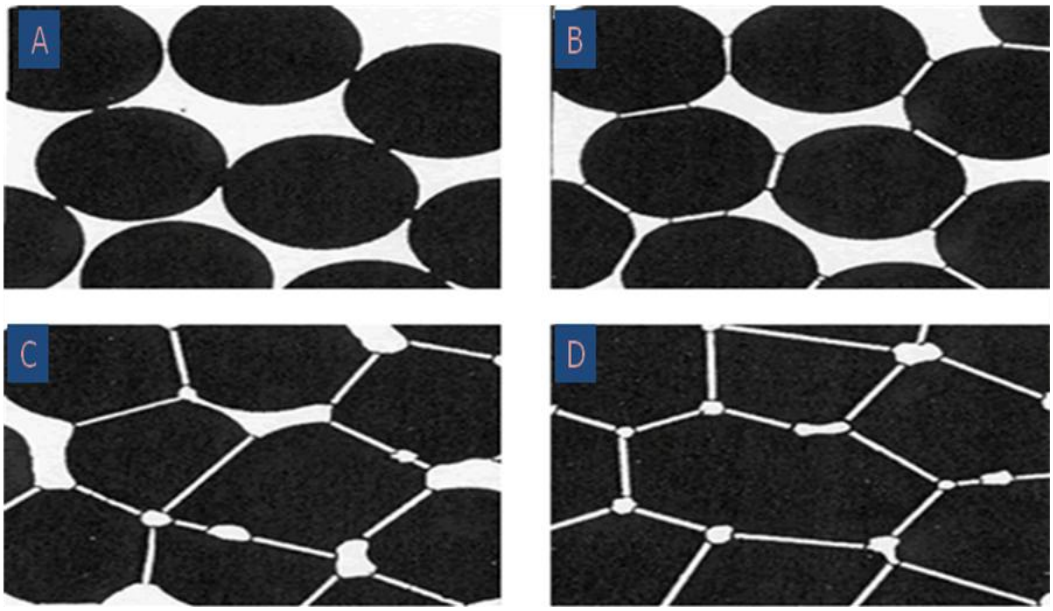

Figure 2.2 Illustration of sintering stages: (A) Compressed particles of powder. (B) Interparticle neck starts to grow between the particles. (C) Second stage discrete particles are less evident and grains are formed and connected to the pores where they start to shrink. (D) In final stage the grains growth have completed and the remaining pores become isolated at four grain intersections.

The initial stage of sintering is characterised by necks formings between contacting particles and adhesive bonds develop. This stage includes rearrangements and slight movements of particles. Thus the overall contact area between particles expands by approximately 20% of its initial value and the densification degree rises only up to 65% in comparison to the green body density. In the second stage, the sizes of necks appreciably increase and particles move close to each other where grain boundaries developed in the place of the necks leading to a rapid grain growth. A network of continuous pore channels is developed along the grain edges and gases can permeate through these pore channels. The grain boundaries will continue to move facilitating the grains to emerge and become bigger. Simultaneously, the pore channels will continue to shrink until they pinch

off and the pores become completely isolated, completing the second stage. Most of the densification process occurs in the second stage. In the third stage (the final stage) the grain growth has completed and any gases trapped inside the closed pores have little chance of escaping. Therefore, less densification happens in this stage.[49-51]

A key factor in achieving highly dense targets is to control the grain growth through the rate of heating. If the temperature increases quickly over a short period of time the grain growth will be rapid since the grain boundaries can move faster. Since the motion of the pores is slower than the grain boundaries the pores will ultimately be left behind trapped, inside the grains. The confined pores can shrink mainly via a volume diffusion mechanism which is not as effective as the grain boundary diffusion. However, when the pores are attached to grain boundaries they can be readily eliminated since atoms located at the boundaries can migrate into pores more quickly by a grain boundary diffusion mechanism leading to densification.[51, 52] In practice, grain growth and densification processes are competing against each other, therefore, grain growth must be controlled to obtain maximum removal of porosity (high density) and this can be realized if the heating rate during sintering is appropriately chosen.

2.2FABRICATION METHOD OF PLD TARGETS

In the last few years, several students in our research group have repeatedly tried to manufacture their PLD targets but unfortunately these targets were brittle and of poor solidity. Thus, they had to buy the PLD targets from outside resources at dearer prices. However, it was decided to challenge this obstacle and try to find a solution. After carrying out a thorough investigation, it was confidently concluded that the main reason causing these targets to be fragile was the rapid heating rate used during the sintering process which unfortunately prevented high densification. The

relation between the density of the sintered target and the speed of heating will be explained in a following subsection.

A number of pure ZnO pellets were prepared to conduct a preliminary study on the effect of different sintering processes (i.e. different heating rates) on the density of the ZnO pellets. Based on this study a proper sintering procedure can be adopted. The pellets were fabricated as follows: a small amount of pure ZnO powder was finely ground for approximately 2 hours using a ball milling machine. The ground powder was placed into a small (0.5" in diameter) stainless steel die and uniaxially cold compressed into pellets using a hydraulic pump. The small die was used in order to reduce ZnO powder usage since these pellets were to be used to carry out the sintering study, and not to grow the thin films.

The density of the sintered pellet can be calculated by measuring its weight and dimensions. An electronic balance with a precision of 0.0001 kg and a digital calliper were used. The pellets' relative densities before and after sintering were determined in respect to the ZnO bulk value (5.65 g/cm^3).[53] The sintering temperature was set to 950 ^oC. Densification degree was studied at different dwell times as well as various heating rates.

Figure 2.3 shows the effect of heating rate on the relative density of pure sintered ZnO pellets. It can be seen that the highest relative density of ~97%, was obtained when a heating rate of 5 ^oC/min was adopted.

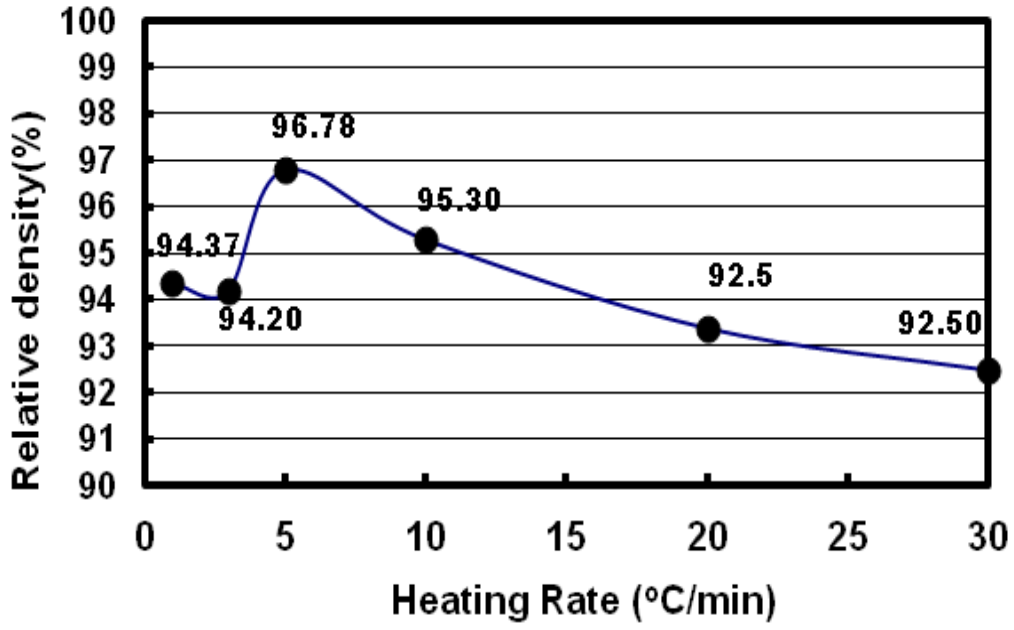

Figure 2.3 The heating rate effect on the relative density of the PLD target sintered at 950 °C.

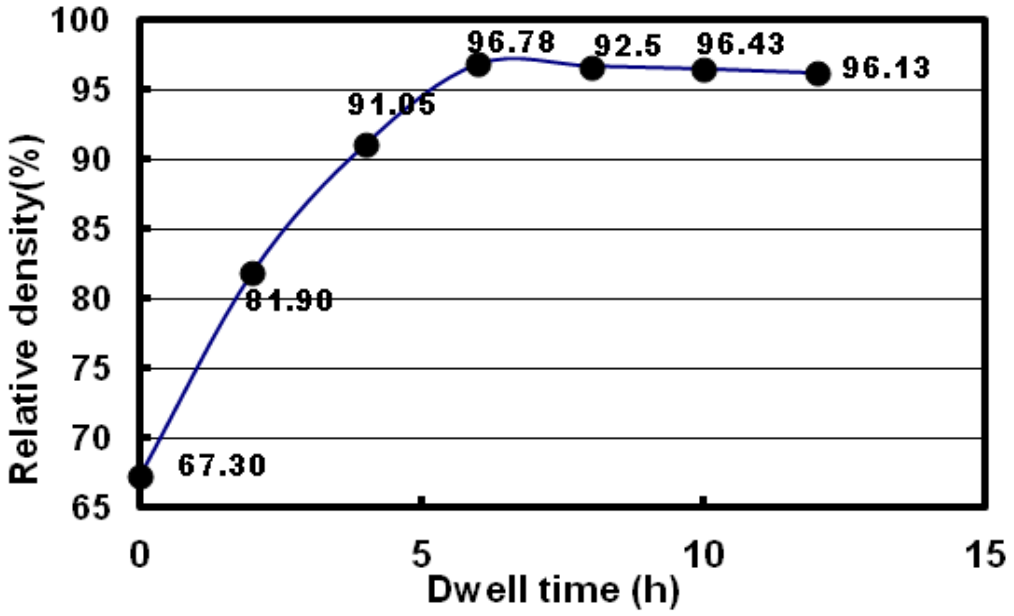

Figure 2.4 The effect of the dwell time on the relative density of the PLD target as the sintering temperature was maintained at 950 °C.

The relative density as a function of the sintering dwell time at 950 ^{o}C was studied and the results are depicted in Figure 2.4. It was concluded that the maximum length of time that the sintered pellet be kept should at 950 ^{o}C is approximately 6 hours. Beyond this time the relative density will slightly drop off. This reduction in density is commonly observed and attributed to material loss (weight loss) of ZnO during heating since Zn sublimes at ~ 900 ^{o}C.[18, 53, 54] Figure 2.5 shows an SEM image of a high density sintered target. The image reveals highly packed grains and almost no pores can be observed.

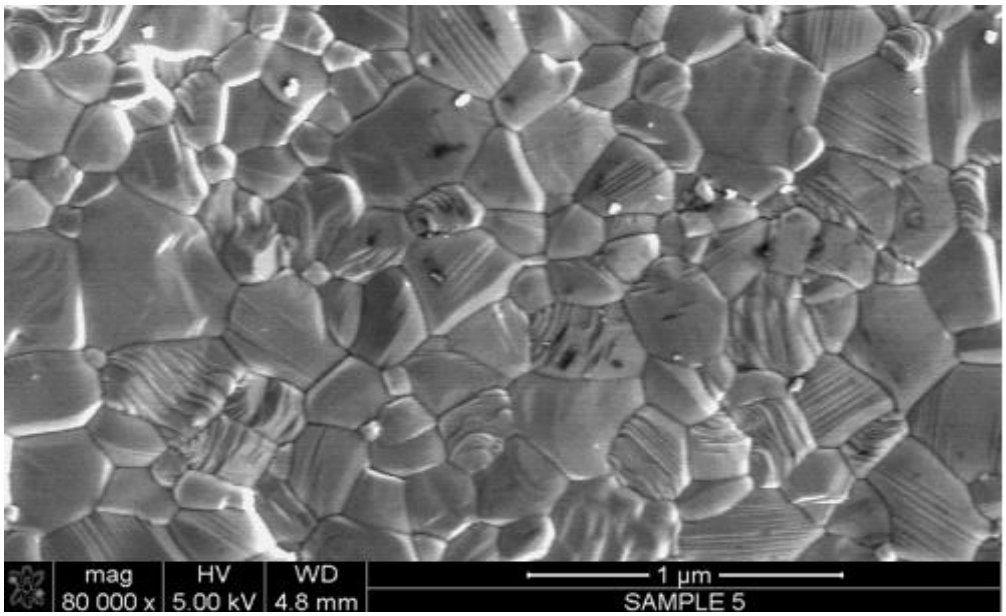

Figure 2.5 SEM image of the surface of a ZnO pellet sintered at 950 ^{o}C for 6 h at a heating rate of of 5 ^{o}C/min.

Two series of doped targets of approximately 1" diameter were also manufactured, denoted here as ZnO: Eu and ZnO: Er. Each series consists of seven targets where the nominal concentration of the rare earth element is varied from one sample to the next. The atomic nominal concentrations of the doping material in these targets of both series were 0.025%, 0.05%, 0.1%, 0.5%, 1%, 2% and 5 at.%. Zinc oxide (Acros Organic Company, New Jersey USA) (99.999 % purity) powder was used. Also, Eu_2O_3 and

Er_2O_3 (Nanostructured & Amorphous Materials Inc., USA) (99.99 % and 99.9 % purity respectively) nano-powders were used as source material for Eu and Er atoms. The average particle size is 43 nm for erbium oxide and between (45-58) nm for europium oxide. The required amounts of Eu_2O_3, Er_2O_3 and ZnO powders were determined and then mixed carefully. The mixture was ground using a ball milling machine (Pulverisette 7 premium line). The milling bowl is made of silicon nitride which is wear resistant with a hardness measuring 91.1 HRA. Therefore no contamination would be expected from the internal wall of the bowl during the grinding process. It should be pointed out that a stainless steel bowl was first considered but the ZnO powder was found to have some iron contamination which come from the erosion of the internal wall of the bowl during the grinding course. The ground mixtures were uniaxially cold compressed into pellets of 1 inch in diameter using a hydraulic pump at pressure of 40 MPa. Figure 2.6 shows a photo of these fabricated targets.

Figure 2.6 One-inch diameter PLD targets of ZnO doped with Er and Eu atoms.

Another set of pure undoped ZnO ceramic targets were also prepared. These targets were fabricated first and used to grow pure ZnO thin films at different growth conditions in order to establish the optimum growth parameters for the PLD system. Such parameters include the growth temperature, target to substrate distance and background gas pressure. The roughness and surface morphology of these pure thin films were investigated using atomic force microscope (AFM) and scanning electron microscope (SEM) techniques since micron-size particulates and a high degree of roughness would have a negative impact on the optical properties of the films.[55]

2.3Pulsed Laser Deposition and Growth Procedure

In 1960, Theodore Maiman successfully demonstrated the first ruby laser operating in the visible region at a wavelength of 694.3 nm, pumped by a pulsed high-power flash-lamp.[56] Not long after this discovery was announced, the first experiment on deposition a thin film using an intense laser radiation was performed by Smith and Turner.[57] However, at the time not much attention was paid to this work since many materials such as ZnO and InSb could not be ablated by such lasers since the visible photons are not effectively absorbed by these materials.[57]

Nevertheless, the development of highly powered lasers operating in the UV region as well as the electronic Q-switching technique helped in generating very short laser pulses which have laid the foundation of successful work on using the laser for producing thin films and also enabled a wide range of materials to be readily ablated since UV photons can be efficiently absorbed by most material.[58] Moreover, the quality of the produced thin films from different materials has been greatly enhanced.[58] Therefore, PLD has been reliably and extensively employed in thin film growth research for years. It is widely considered as one of the simplest

growth techniques utilised for thin film synthesis for different types of materials such as insulators, semiconductors, metals, polymers and biological materials.[59] The next sections discuss the theoretical principles of the PLD technique as well as the experimental setup and growth procedure that was adopted in this work.

2.3.1 How does PLD work?

Basically, PLD is a technique employed to grow a wide range of thin films where a solid material is ablated (vaporised) by using high powered laser pulses and then gets deposited onto a suitably chosen substrate. A typical cross-section of a PLD system is schematically shown in Figure 2.7. This system was used to produce all the thin film samples studied in this thesis.

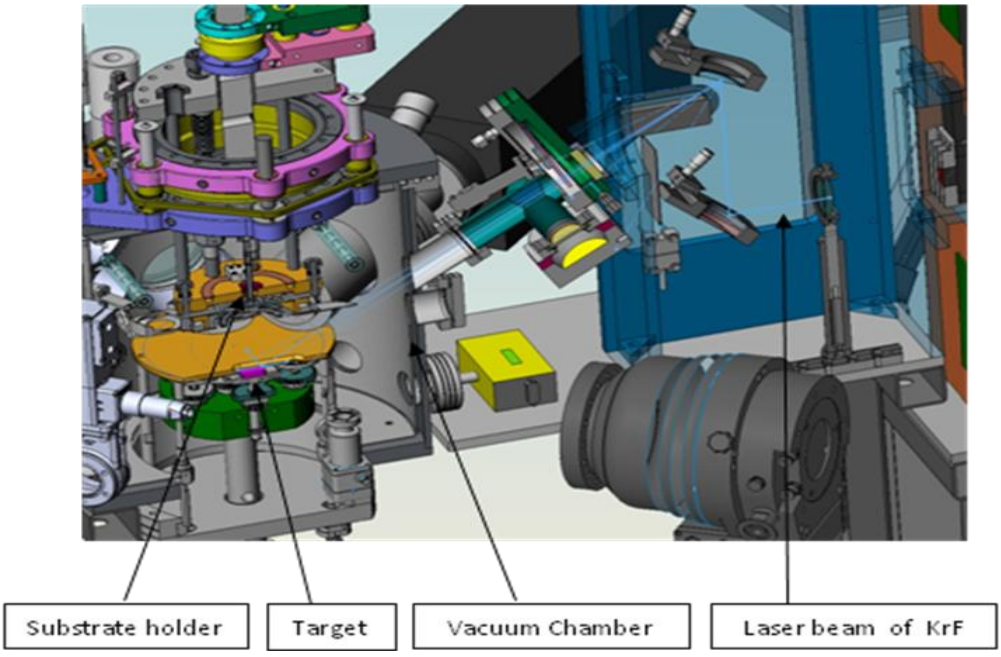

Figure 2.7 Schematic cross-section of the PLD system used at King Abdul Aziz City for Science and Technology (KACST) in Saudi Arabia.

Experimentally and conceptually the PLD technique is deemed simple. Its experimental set-up consists of a high-power UV nanosecond pulsed laser, a vacuum chamber which accommodates a multi-target carousel, a resistive

heater, substrate holder, vacuum pumps and optics to guide and focus the laser beam onto the target. In a PLD system the deposition process begins when the pulsed laser is tightly focused onto a rotating target. When the laser has a sufficient energy density each pulse is absorbed by a small volume of the target, typically the first top surface layers, and then ablates (vaporises) a small amount of the target generating a plasma plume. The plume consists of highly energetic species such as atoms, diatoms, radicals and other low mass constituents which travel away from the target in a highly-forward directional motion.[59] Although the experimental set-up of the PLD is simple and its operation is fairly easy, the ablation dynamics of laser-plasma-solid interactions is a very complex phenomenon.

A detailed theoretical study of such phenomenon was carried out by Rajiv Singh and his colleague.[60] In their study a theoretical model to simulate the laser-plasma-target interactions was developed. In this model, the plasma is assumed to be an ideal gas which is confined in a small space at high pressure and temperature and abruptly expands towards a substrate. The ablation phenomenon can generally be described as a three-stage process based on the nature of the laser-plasma-target interactions. These processes are summarised as follows:

1- In the first stage, interaction between the laser pulses and the first top surface layers of the target takes place resulting in removal of target material. During this phase several processes such as target melting, ripple pattern formation and phase segregation are usually seen on the target surface. The removal of the material results from the intense heating supplied by the laser energy which consequently leads to melting and rapid evaporation processes in the form of a highly energetic plume of plasma. In reality, these thermal effects involve many physical parameters. Some are laser-related such as pulse energy density, pulse time, pulse shape and

wavelength while the other effects are material-related such as reflectivity, absorption coefficient, heat capacity and thermal conductivity. Based on the heat balance equation, the amount of the ablated material per pulse as a function of laser and material parameters is given by[60]

$$\Delta x_t = \frac{(1-R)(E-E_{th})}{(\Delta H + C_v \Delta T)} \qquad (5)$$

where Δx_t, ΔH, C_v and ΔT are the evaporated thickness, volume latent heat, volume heat capacity and the maximum temperature increase respectively. R is the target reflectivity, E_{th} is the energy threshold above which evaporation is observed and E is the laser energy density.

2- Stage two involves the interaction between the incident laser pulse and the evaporated material. In this interaction, the plasma is created along with its initial isothermal expansion. The plasma temperature further increases due to the absorption of the laser energy via an inverse Bremsstrahlung process. The temperature of the plasma is estimated to be around 10,000 K. The absorption of the laser radiation by the plasma is considered more efficient only within a distance very close to the target which is the region that has high ion density. The absorption coefficient of the plasma is given by[60]

$$\alpha_p = 3.69 \times 10^8 \frac{Z^3 n_i^2}{T^{0.5} \nu^3} (1 - e^{\frac{-h\nu}{k_B T}}) \qquad (6)$$

where Z, n_i, T, h, k_B and ν are the average charge, ion density, the temperature of the plasma, Planck constant, Boltzmann constant and the laser frequency respectively.

3- In the third stage, a three-dimensional adiabatic plasma expansion occurs in vacuum when the laser beam is terminated between two successive

pulses and the plume dissipates causing the melt front on the target to re-solidify. The rapid adiabatic expansion in vacuum is produced by the large density and pressure gradients. When the expansion starts, the velocities of the various ejected species are comparatively slow but their accelerations are high. However, when the velocities reach ~10^5 – 10^6 cm/s accelerations start to slow down and finally become zero. For this reason the plume is formed into an elongated shape. Figure 2.8 shows a typical plume of plasma of a ZnO ceramic target irradiated with an excimer laser running on KrF which lases at 248 nm.

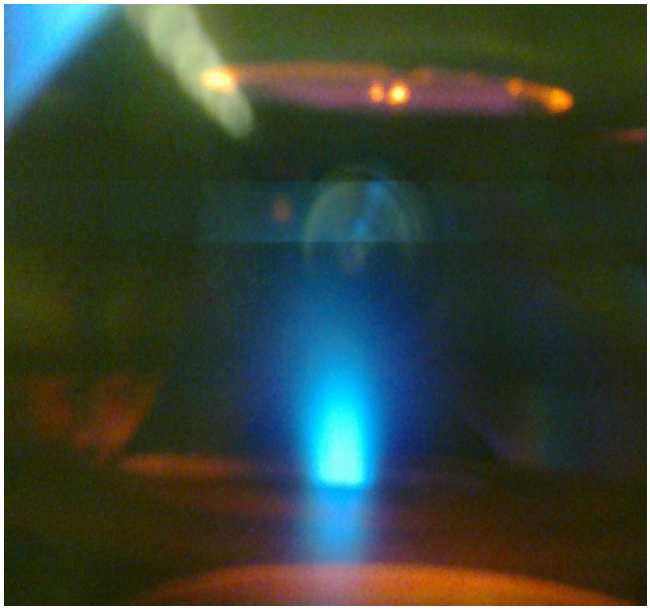

Figure 2.8 ZnO plume in 100 mTorr O_2 and laser energy density of ~3 J/cm^2.

2.3.2Why PLD was used in this work?

It is a matter of fact that the ablation process involves a number of complicated physical and chemical processes in addition to some other intrinsic problems associated with the PLD method such as splashing (generation of micro-sized particulates due to the sub-surface boiling effect) and small area coverage due to the narrow angular distribution of the

ablated species. Despite these drawbacks, the PLD is still a very versatile research technique and is favourably chosen by many scientists.[59]

PLD has many attractive features. For instance, the high probability of obtaining stoichiometric transfer between the target and the grown film is the most significant feature of PLD due to congruent ablation of the target. This means the atomic ratios of a multicomponent target can be retained in the deposited thin film. Producing stoichiometric thin films using a single target by evaporation or sputtering techniques is challenging since the partial vapour pressures and the sputtering yield of the target's constituents are generally varied leading to different atomic ratios.[61] In PLD, the extremely high heating rate (typically 10^{12} K/s) of the target surface induced by the intense laser radiation ensures all constituents of the target can evaporate at almost the same time in spite of their different binding energies. As a result stoichiometric films are expected.[61]

Furthermore, due to the consistency of the stoichiometry the PLD technique can be effectively used in producing stoichiometric thin films out of very chemically complicated materials. For example, a PLD thin film was produced using a Nd and Cr-doped $Gd_6Sc_2Ga_6O_{12}$ target (lasing garnet) which would be difficult to produce by other deposition techniques such as chemical vapour deposition.[62] This very complex material consists of six different elements and more than 160 atoms per unit cell.

Another remarkable feature of the PLD technique which is so beneficial for this work is that it has been demonstrated that during, the ablation process dopant atoms are mainly ejected from the PLD targets in the form of atomic radicals and not as molecules. Importantly, the radical particles have high sticking coefficients and a damage-free nature which greatly assist in achieving successful doping while preventing clustering of Er-O and Eu-O compounds in the deposited films.[63, 64]

2.3.3Growth Procedure

All thin films studied in this work were grown as follows: 5×5 mm double-side polished *c*-cut sapphire substrates were first cleaned using a three-step sonication. Trichloroethylene, acetone and methanol were successively used for 10 minutes each. PLD targets and a cleaned substrate were inserted into the chamber which was then evacuated to 1.5×10^{-5} Torr base pressure using two pumps. The temperature of the sample heater was raised from room temperature to 300 ^{o}C at a heating rate of 10 ^{o}C/min and held at this temperature for 30 minutes. This step was done to eliminate any chemical residuals resulting from the cleaning process and to minimise the thermal shock to the substrate when the temperature was increased to the desired growth value. The temperature was then increased to 750 ^{o}C at 30 ^{o}C/min and held there for two hours. The growth took place during the second hour where the first hour was allocated for the thermal annealing process. A pure ZnO buffer layer was first grown at 400 ^{o}C for 10 minutes for some samples then the doped ZnO film was deposited on this buffer layer as explained above.

Pure O_2 gas at flow rate of 10 sccm (standard cubic centimetre per minute) was introduced into the chamber before the target was ablated and then the growth was carried out at 100 mTorr. When the deposition finished the temperature of the sample heater was gradually decreased to 25 ^{o}C at 20 ^{o}C/min. The O_2 flow was maintained until the temperature dropped to around 300 ^{o}C before the O_2 flow completely stopped. The laser energy density was calculated to be ~ 3 J/cm^2 and the laser pulse repetition rate was 10 Hz and the target was continuously rotated at a speed of 25 rotations per minute.

Chapter 3

CHARACTERISATION TECHNIQUES

In this work, a number of characterisation techniques were employed to investigate the structural and the optical properties of all the samples grown. A brief description of the physical basis, usefulness and the experimental set-up of each technique are presented.

3.1X-ray Diffraction

The constituents of an ideal crystalline material (atoms, ions or molecules) are perfectly and orderly arranged in a long-range lattice which is spatially extended in three dimensions. A two dimensional representation of such an arrangement is schematically depicted in Figure 3.1 However for real crystals imperfections and stresses are unavoidably present due to native defects, impurities and lattice misfits between substrate and deposited films...etc. Thus, the structure quality is disturbed. Such irregularity can easily affect other physical aspects of the crystal such as the optical and electrical properties. Therefore, investigating the crystal structure is essentially invaluable to obtain clearer understanding of the material under study.

It is known that the spacing of planes in crystal lattice of solids are of the order of 1 Å which is comparable to the wavelengths of the X-ray radiation. Hence X-ray wavelengths can be advantageously used to structurally investigate the crystalline materials. Since the atoms exhibit a regular pattern inside the lattice they can be thought of as scattering centres or simply they can act as a three dimensional grating. When a lattice is irradiated with monochromatic X-ray beams constructive interference can happen. This diffraction effect was practically demonstrated by W. L.

Bragg in 1913. As a result he derived a physical law based on the light diffraction principles, later called Bragg's Law, which states that an x-ray diffractive peak will only be detected if the following equation is satisfied[65, 66]:

$$n\lambda = 2d\sin\theta \qquad (7)$$

where λ is the wavelength of the x-ray radiation, d is the interplanar distance between two consecutive atomic planes, θ is the Bragg's angle (incident angle of the x-ray beams) and n is an integer number. Clearly, Bragg's Law provides the conditions that are required for the observation of diffractive peaks. Figure 3.1 schematically illustrates the Bragg's Law for the reflection of x-rays by a crystal. The two parallel incident x-ray beams shown are reflected by atoms (acting as scattering centres) located in two different planes. For these reflected beams to interfere constructively the path difference between them, $2d\sin\theta$, must be equal to an integral number of the x-ray wavelength. The produced pattern of scattered radiation is characteristic of the crystal being irradiated and the wavelength of the x-ray source.[65, 66]

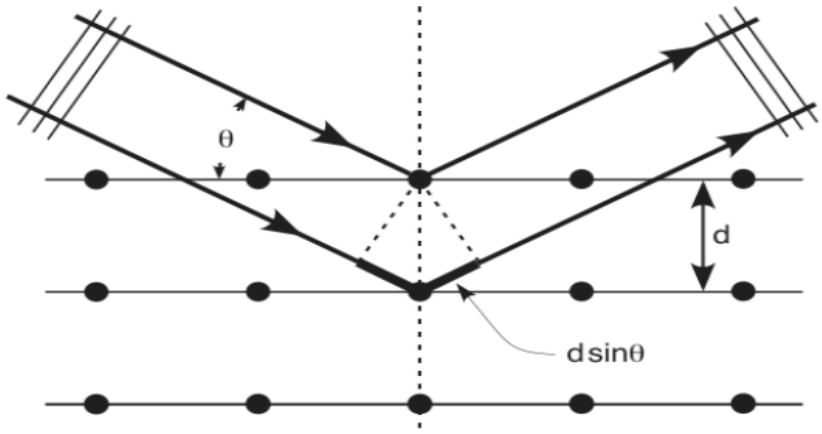

Figure 3.1 Schematic representation of the diffraction of two x-ray beams occurring in a crystal consisting of parallel atomic planes with an interplanar spacing d. The path difference between the two beams is $2\,d\sin\theta$ and θ is the incident angle.

Bragg's Law can also be linked to the Miller indices (*h*, *k*, *l*) of a hexagonal structure by the following equation[67]:

$$\frac{1}{d} = \frac{4}{3}\left(\frac{h^2 + hk + k^2}{a^2}\right) + \frac{l^2}{c^2} \qquad (8)$$

where a and c are the lattice constants.

Generally, an X-ray diffraction (XRD) setup consists of three basic components: an X-ray tube, a goniometer (stepping motor assembly) and a detection system. The X-ray tube contains a filament which is heated electrically to release electrons and then they are accelerated by a high voltage (20-50 kV) to collide with a target metal (the anode) usually copper or molybdenum. The anode will emit very sharp lines superimposed on a continuous x-ray radiation which are characteristic features of the anode material. These sharp lines arise because the bombarding electrons remove electrons from the innermost K shell (n = 1) leaving their spaces empty which are then occupied by electrons descending from higher energy electronic shells such as L or M where n = 2, 3 respectively. The difference in energy between the involved shells appears as an X-ray radiation and is denoted by K_α when the descending electrons come from L shell while K_β when they come from M shell.[65, 66]

In XRD measurements a monochromatic beam is used so one sharp line is selected and the continuous radiation and the other lines are filtered out using a thin foil of a suitable metal.[65] The generated XRD pattern for a sample is simply compared with an XRD powder pattern disseminated by the International Centre for Diffraction Data® (ICDD®), a non-profit scientific organisation established to collect, edit and disseminate XRD data for crystalline material analysis and identification.

All samples studied in this work were crystallographically analysed using a D8 advanced X-ray diffractometer with CuKα radiation (1.5405Å) available at the Department of Chemical and Materials Engineering at Auckland University. Since the position of the diffraction peaks (θ) depends on the instrumental characteristics such as wavelength the diffraction spectra of all samples were offset using the diffraction peaks of a *c*-axis single crystal sapphire.[66] The bulk sapphire is used because it is stress-free and possesses a hexagonal crystal structure as ZnO.

Furthermore, X-ray diffraction is an important analytical technique to study the internal configuration of crystalline materials, providing structural information such as phase identification, crystal orientation, residual strain, grain sizes and crystallinity. When a lattice of a crystalline material is distorted by, for example, impurities, intrinsic defects, lattice misfit...etc an internal stress is developed leading to elongations and contractions which change the inter-planar spacing of the lattice planes. Such stress effect can be accurately evaluated by comparing the inter-planar distances of the stressed material with those of a bulk crystal (stress-free) from the same material. The residual internal strain along the *c*-axis (perpendicular to the c-plane) in the prepared films can be estimated from the XRD measurement by using the following equation[68]

$$\varepsilon = \frac{c - c_o}{c_o} \times 100\% \qquad (9)$$

where c_o is the lattice constant in ZnO bulk (strain-free) which has a value of 5.2057 Å[69] at 300 K while *c* is the calculated lattice constant in the deposited film. The residual strain is considered compressive in *c* direction if the ε has a negative value while tensile if it has a positive value. The in-plane stress of the films can be obtained using the modulus of elasticity and the calculated strain [68, 70]

$$\sigma = \frac{2c_{13}^2 - c_{33}(c_{11} + c_{12})}{2c_{13}} \cdot \varepsilon \qquad (10)$$

Where c_{ij} are the elastic stiffness constants of bulk ZnO and have the following values: c_{11} = 208.8, c_{33} = 213.8, c_{13} = 104.2 and c_{12} = 119.7 GPa. By substituting these constants into equation 9 a numerical relation is obtained:

$$\sigma = -465 \cdot \varepsilon \qquad (11)$$

where the unit of the residual average stress is GPa.

3.2X-ray Photoelectron Spectroscopy

X-ray Photoelectron Spectroscopy (XPS) is a versatile and non-invasive spectroscopic technique which is increasingly applied to a wide range of materials in order to acquire a variety of important analytical information associated with the outer surface layers of the materials. Its physical concept is based on the photoelectric effect which was discovered by Hertz in 1887. He noticed that when two electrically isolated metallic plates placed in vacuum are exposed to light they showed an enhanced ability to spark. Later, Albert Einstein was able to successfully explain this phenomenon using Planck's quantisation concept of energy. Einstein's interpretation was a great achievement where he was awarded the Nobel Prize in 1921 for this work.[71]

The advantages of x-ray photoelectron spectroscopy were not fully appreciated until Kai Siegbahan and his colleagues were able to develop an instrument capable of adequately analysing core photoelectron emissions with sufficiently high resolution. In an XPS measurement the binding energies of the core electrons of the material under study are the cornerstone of this technique since core electrons are shielded by the outer

electrons in the higher energy levels. Thus, the core electrons' energies are not perturbed. Also, they are tightly bound to the nucleus so they do not take part in the formation of chemical bonding in contrast to valance electrons.[50, 71] Therefore the binding energies of the core electrons are characteristic for elements in a certain chemical environment and can be reliably used as a finger print of the investigated material.

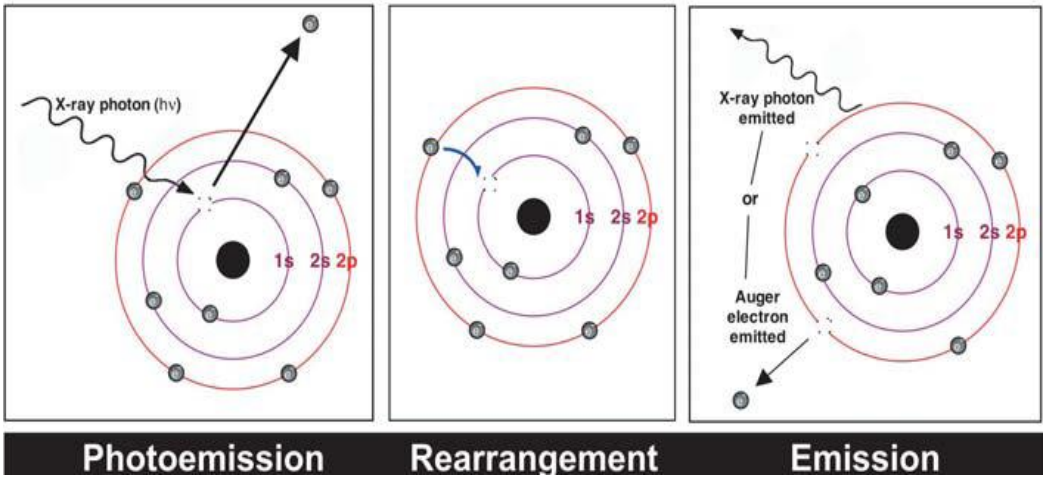

Figure 3.2 Schematic diagram showing X-ray radiation-atom interaction and the possible outcomes.[71]

An understanding of the interaction process between the x-ray photons and matter is fundamentally important for the interpretation of the XPS spectrum. When X-ray radiation of a sufficient energy is directed on the surface of a material, they will interact and usually three possible processes occur. These processes are schematically shown in Figure 3.2. The x-ray photons are absorbed by the atoms in the material causing the emission of photoelectrons from both the core and valance shells of the atoms. As a result a core hole is created and is generally filled by an electron dropping from a higher energy level. The excess energy due to the difference between the two orbital levels will be emitted as x-ray fluorescence or it will be giving up to an electron in one of the higher energy level leading to its complete removal from the atom. This ejected electron is called an

Auger electron. Therefore, the obtained XPS spectrum is typically composed of a number of peaks attributed to both photoelectrons (XPS electrons) and Auger electrons as well as some other spectral features such valance band peaks.[50, 71]

As previously mentioned, each emitted photoelectron is associated with a characteristic binding energy for each element present in the sampled volume of the investigated material. Thus, the presence of peaks at specific binding energies confirms the existence of a particular element in the sample. Furthermore, the intensity of the XPS peak, precisely the number of the ejected electrons, is directly related to the concentration (the number of atoms) of the element within the sampled volume. Theoretically, there are several factors that must be taken into consideration when the intensity, here referred to as the integrated area under the photoelectron peak, is calculated and hence a quantitative evaluation for the elemental composition can be accurately obtained. These factors can be either sample characteristics or spectrometer characteristics. The cross-section of the photoemission and the inelastic mean free path (escape depth) of the photoelectron are some examples of the sample-related factors while the transmission function of the spectrometer and the detector efficiency belong to spectrometer-related factors.[72]

By assuming a homogenously distributed sample and taking into account the above-mentioned factors a very simplified mathematical formula which relates the intensity I_i of a photoelectron from element *i* to the concentration η_i of the element *i* is given by[72]

$$I_i = J\eta_i\sigma_i\delta\gamma \qquad (12)$$

where J is the x-ray flux, σ_i is the photoemission cross-section of a photoelectron element *i*, δ is a term which accounts for all spectrometer-

related factors and γ is the electron attenuation length. By defining elemental sensitivity factor as $S_i = J\sigma_i\delta\gamma$ the concentration of the element *i* is given by

$$\eta_i = \frac{I_i}{S_i} \tag{13}$$

The sensitivity factors are usually stored in a library in the processing programme that is used to carry out the quantification process.

However, a direct comparison of peak areas (integrated intensity) should not be chosen for making a meaningful comparison between samples. This is due to various reasons, for example, not all the emitted electrons from the sample can be effectively collected because of the ability of the instrument to capture them. Moreover, the efficiency with which the ejected electrons are detected relies on the operating mode of the XPS instrument. Therefore, the elemental concentration is adequately expressed in terms of atomic percentage as follows[72]

$$C\% = 100 \times \frac{\frac{I_i}{S_i}}{\sum \frac{I_i}{S_i}} \tag{14}$$

XPS is mainly considered as a chemical surface sensitive technique since it can only probe the uppermost atomic layers of the sample's surface approximately the first top 10 nm and the concentration of the elements of interest should exist at 0.1 at. % or higher.[73] The sensitivity of the XPS detection toward the atoms in the surface is caused by the relatively short distance that the photoelectrons can travel to escape the material and arrive at the detector without losing their kinetic energies due to inelastic scattering processes.[71]

In XPS measurements the characteristic binding energies of the ejected core electrons can be calculated based on the well-known formula derived by Einstein which he used to explain the photoelectric effect and given by[50, 71]

$$E_k = h\nu - E_b - W \qquad (15)$$

where E_k and E_b are the kinetic energy and the binding energy of the ejected electron respectively, $h\nu$ is the energy of the incident x-ray photon and W is the combined work function of the sample and the spectrometer. Once these photoejected electrons are in vacuum they are accumulated by a collecting lens (electrostatic or electromagnetic) and then sent to an energy analyzer where they are separated according to their respective kinetic energies. The analysed electrons are detected using a multi-channel detector. A simplified representation of an XPS spectrometer is schematically shown in Figure 3.3.

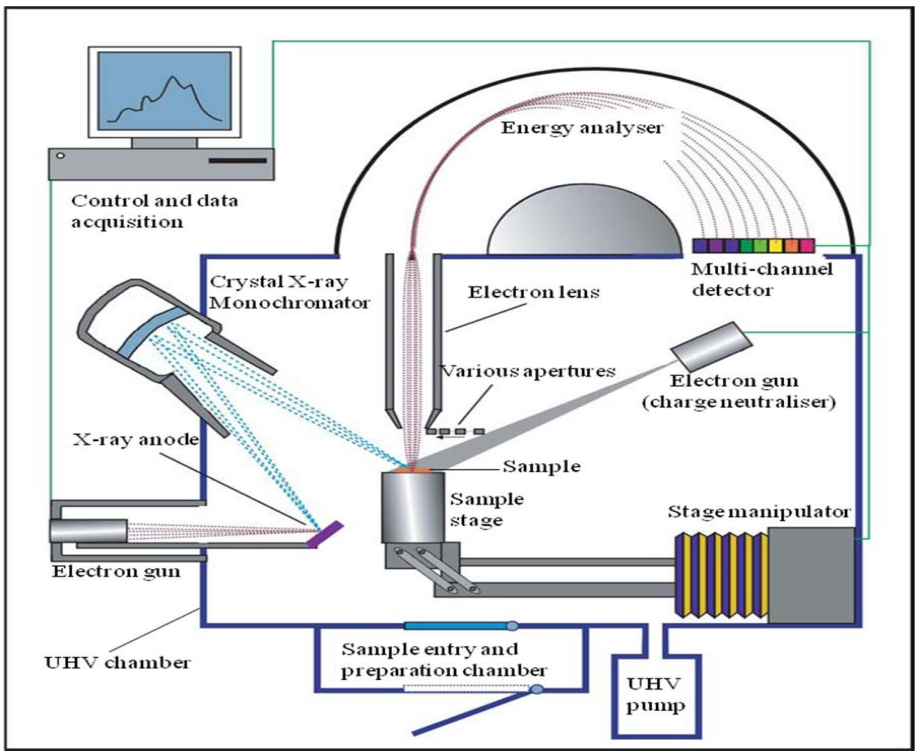

Figure 3.3 A simplified schematic representation of an XPS spectrometer.[71]

Typically, the X-axis of an acquired XPS spectrum represents the binding energy of the core-level electrons belong to different atomic orbits while in the Y-axis a series of photoelectron peaks where their relative intensities indicate the number of the outgoing electrons at each particular binding energy as shown in Figure 3.4. The spectroscopic notation for the XPS spectral lines conventionally takes the form nl_j which is different from the $^{(2S+1)}L_J$ atomic notation that was previously mentioned in section 1.3 to describe the electron energy states in an atom.[73] The letters n,l,j are the principal, the orbital angular momentum and the total angular momentum quantum numbers respectively. It should be noted that the orbital angular momentum number is designated by letters in lower case.

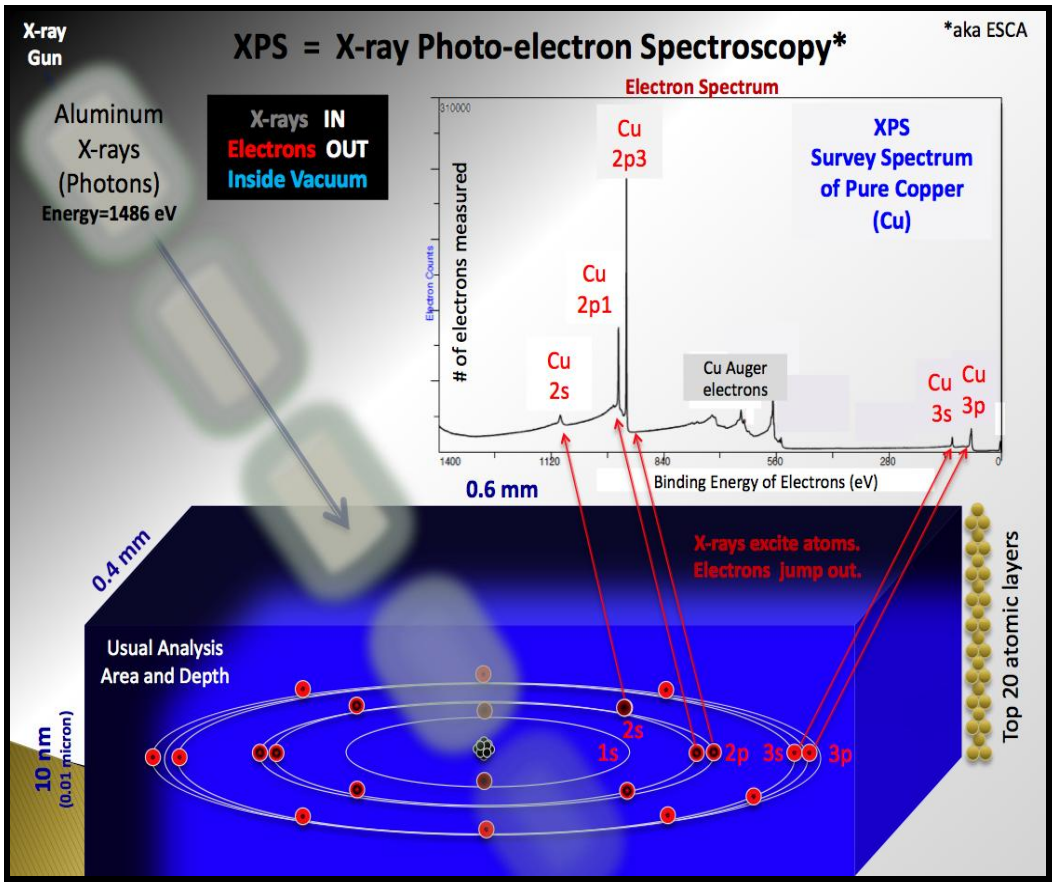

Figure 3.4 An illustration showing how a typical XPS spectrum is generated for a pure copper thin film.

The X-ray photoelectron spectroscopy is widely applied to obtain both qualitative and quantitative information. A survey scan is recorded over a broad range of energies using wide steps, typically between 50 and 100 eV. This fast scan is very useful to quickly discover what elements are present, which are absent and their relative abundances within the detection limit of the XPS system. The elemental surface concentration can be reliably estimated by integrating peak areas after eliminating the background contribution caused by inelastic scattering.[71, 73, 74]

Furthermore XPS measurement can also provide very informative data such as the oxidation state of the atom and the local chemical environment around the atom. The binding energies of core electrons are noticeably affected by the chemical structure giving a small shift in the peak positions. This small shift is called a chemical shift since it is related to the chemical status of the material. The chemical shift can be readily identified by performing high resolution scans over a narrow energy range, around one of the core level peak, at small step sizes, typically (10 – 20) eV. Thus, detailed line shape and small shifts in peak position can be easily determined in the high resolution spectra. The ability to identify different oxidation states and chemical environments is considered one of the major strength features of the XPS technique. The measured peak positions are compared to those documented in a standard database in order to calculate the chemical shift.[50, 71, 73, 74]

The XPS measurements were carried out at the Department of Chemical and Materials Engineering at Auckland University using a Kratos Axis Ultra DLD spectrometer which is equipped with a monochromatic X-ray Al Kα source of 1486.69 KeV. These experiments were performed in a high vacuum environment where the base pressure was less than 10^{-9} mbar. Such condition is needed to prevent the existence of any adsorbed contaminants

(gas molecules usually present in the analytical chamber) and hence to reduce the scattering effect of the x-ray photons by such contaminants. As a result, the mean free path of the XPS electrons is enhanced leading to more accurate measurement of the electrons kinetic energies.

Accumulation of positive charge at the surface due to the ejection of photoelectrons from the samples is a common problem in XPS measurements leading to the so-called "charging" effect. Such electrostatic charging would decelerate the photoejected electrons and hence alter their kinetic energies. Therefore, XPS peaks would appear at higher binding energy than they should be. The Kratos charge neutralizer system was employed to produce low energy electrons to correct for the built-up charges.

An analysis area was set to be approximately 500 μm^2 of every examined sample. The recorded spectra were calibrated using the "adventitious" C 1s transition at a binding energy of 284.8 eV.[75] Hydrocarbon atoms are inevitably common contaminants where a carbon overlayer can be easily formed when the samples are exposed to air.[75] Hydrocarbon atoms are generally accepted to be of the chemical state of the sample under study. XPS spectra were analysed by CasaXPS processing software developed and published by the Casa Software Ltd., UK.

3.3Transmission Measurement

Optical transmission (and/or absorption) measurements are generally performed to determine and evaluate some optical constants of materials which are considered important in the fabrication and analysis of devices. These optical constants include the absorption coefficients, the bandgap energy, dielectric index and refractive index. Moreover, optical transmission or absorption measurements are used to detect certain impurities present in a material as some impurities have characteristic absorption lines. During a transmission measurement a range of monochromatic wavelengths is systematically shone through a sample and the transmitted light is continuously recorded as a function of the incident wavelength. A transmission spectrum is generated by plotting the relative intensity of the transmitted light to the incident light as a function of the wavelength.

In this work transmission spectra were obtained at room temperature using a model 14 CARY spectrometer at the Physics and Astronomy Department at University of Canterbury. The CARY 14 is a dual beam spectrometer controlled by a desktop computer and can be scanned over a wide range of wavelengths from ultra-violet to near infra-red. This instrument utilises the comparative photometry principle where a beam of light is passed alternately through a reference compartment and a sample compartment and the intensity ratio of the sample-to-reference gives the sample's transmittance.

An advantageous feature of the spectrometer is a servo system which acts as an electronic feedback loop so the slit width can be automatically adjusted to keep the reference beam intensity constant as the wavelength is varied. All spectra were corrected for the background and dark

contributions. Figure 3.5 illustrates various optical components of the spectrometer.

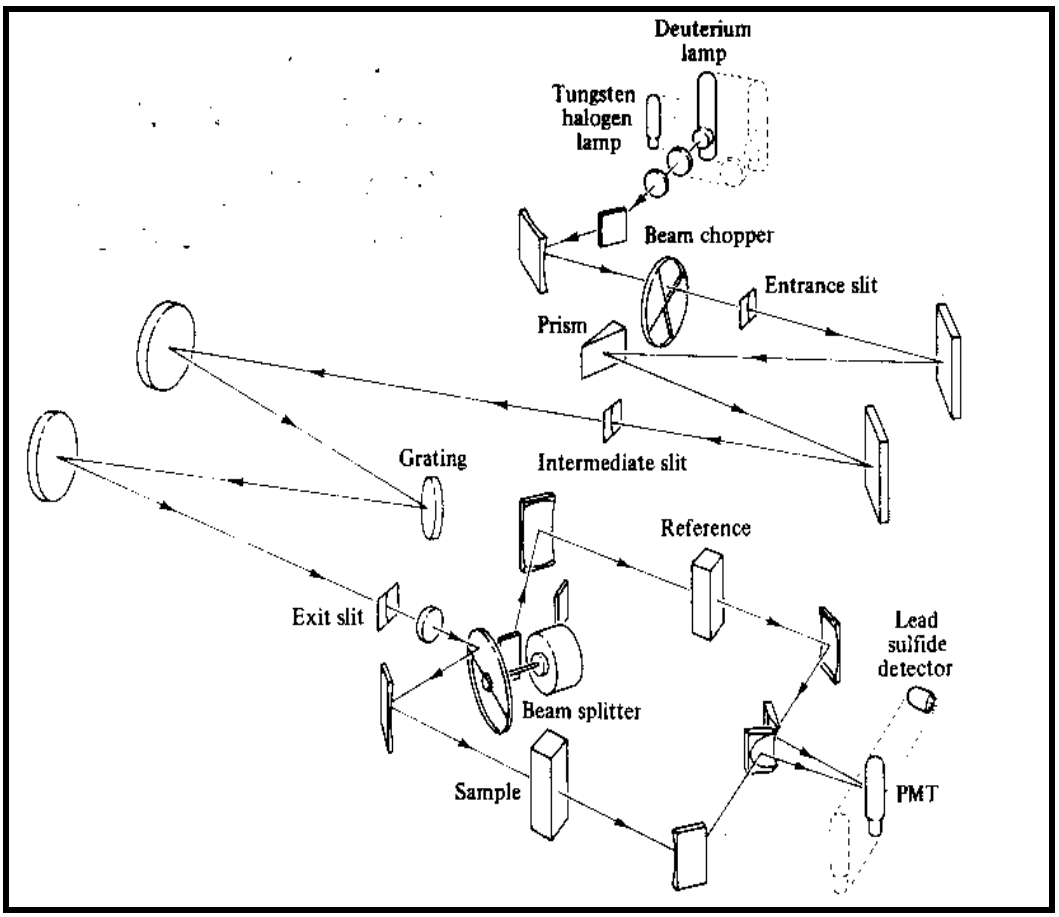

Figure 3.5 Simplified schematic diagram of the CARY model 14 spectrometer.

From the transmission data the optical bandgap E_g can be easily determined using the Tauc relation which is given by[76]

$$\alpha = \frac{C(h\nu - E_g)^n}{h\nu} \tag{16}$$

Where α is the absorption coefficient, C is an absorption constant, $h\nu$ is the photon energy and $n = 1/2$ for a direct bandgap or $n = 2$ for an indirect gap. The absorption coefficient α can be calculated using the following equation:

$$\alpha = \frac{A \times \ln(10)}{d} \qquad (17)$$

where d is the film thickness and A is the absorbance which is obtained from the transmission (T),

$$A = -\log_{10}(T) \qquad (18)$$

According to equation (15) if $(\alpha h\nu)^2$ is plotted vs $h\nu$ the bandgap energy (E_g) is the *x*-intercept of the extrapolation of the best fit line.

3.4Scanning Electron Microscope

The Scanning Electron Microscope (SEM) is undoubtedly one of the most valuable and powerful analytical tools capable of producing high resolution topographical and morphological images with magnification extending to the nanoscale. Generally speaking, SEM images are simply developed by scanning an electron beam across a surface of a specimen. However, the formation of an image using the SEM technique is technically based on acquiring distinct emitted electrons resulting from the interaction between the incident electrons, known as primary electrons, and the imaged area of the specimen.

Such an interaction will be first briefly discussed in order to understand how these emissions are produced inside the sample and how they can be used to form an SEM image of the sample.[77] Generally when an accelerated finely focused beam of electrons strikes into the surface of a sample a number of emanations are generated such as secondary electrons (SE), Auger electrons, backscattered electrons (BSE), cathodoluminescence and characteristic X-rays. These emitted electrons and photons are only produced from a particular emission volume inside the sample where the size of the emission volume largely depends on the kinetic energy of the

accelerated beam and the atomic number of the sample.[77, 78] Figure 3.6 illustrates a schematic representation of the various produced outcomes due to the interaction between the incident electrons and the imaged material along with the spatial distribution inside the material.[78]

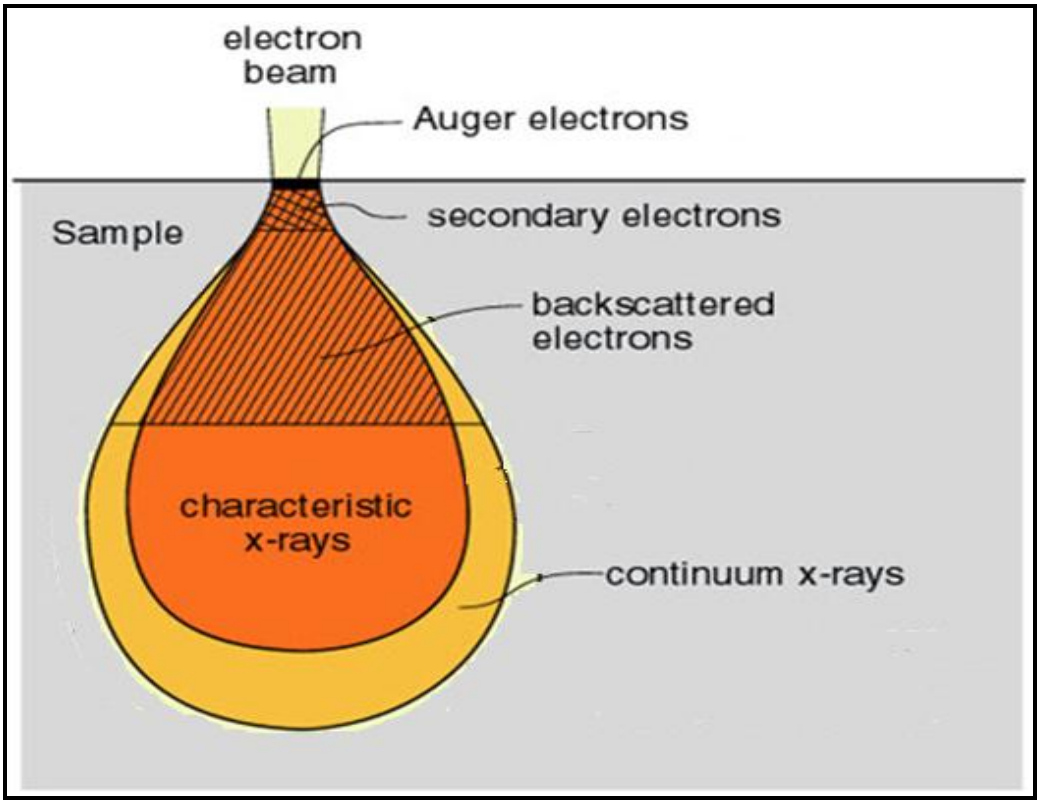

Figure 3.6 A simplified illustration showing various emissions occuring as a beam of electrons strikes a surface of material and the anticipated emission volume inside the material.[78]

These different emissions can be effectively collected, analysed and advantageously applied in many scientific applications such as in the SEM where a variety of very important data can be obtained. They can be classified according to their energies as follows[78]

Auger electrons < SE < BSE < x-rays

When a beam of electrons impinges the surface of a specimen each individual incident electron will go through a scattering effect either

elastically or inelastically. In the case of elastic scattering the kinetic energy and the velocity of the scattered electrons will remain constant but their trajectories will change. However, some of the elastically scattered electrons will bounce back out of the specimen as backscattered electrons (BSE) while the rest will penetrate randomly throughout the sample till their kinetic energies eventually vanish and dissipate as heat.

For the inelastic scattering process the primary electrons may interact with the atoms in the irradiated sample giving rise to several other types of emissions. For example, continuum X-ray (Bremsstrahlung) radiation can be generated when the primary electrons are decelerated by the electromagnetic field (the coulomb field) around the atom. Other effects can also be seen when the primary electron collides with an inner atomic electron, causing it to be completely removed from the atom and simultaneously creating a vacancy in the place of the ejected electron. This vacant position can be filled by another electron from a higher orbital level, leading to either a characteristic X-ray emission or an Auger electron.

Furthermore, low energy secondary electrons can also be produced when the primary electron strikes with a loosely bound electron to the nucleus, which is located in the outer shells of an atom. However, if the secondary electron recombines with a hole, which has been created during the previously mentioned scattering processes, a photon may be emitted at wavelengths in the range of visible or near-infra-red. This photonemission is known as cathodoluminescence. The energy spectrum of the previously mentioned emitted electrons is shown in Figure 3.7. SEs are those which have low energies relative to the energy of the primary electrons typically less than 50 eV. The majority of the SEs lie between 0.5 to 5 eV while the BSEs are more energetic and exhibit a wide range of energy from above 50 eV up to the primary electron energy.[79]

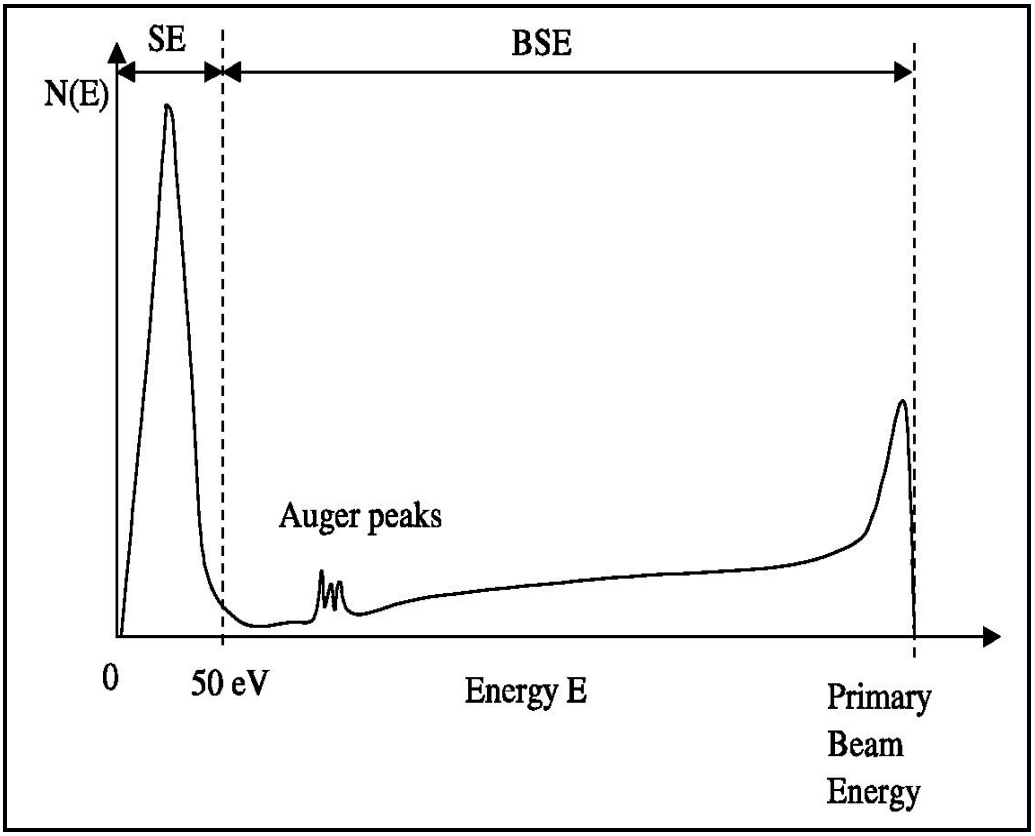

Figure 3.7 An energy spectrum of the different emitted electrons from the sample being imaged.[79]

In general, SEM images can be formed by optionally operating the SEM in one of its different imaging modes based on which kind of emitted electrons are detected and analysed. BSE and SE operational modes are the two main types. Usually, an SEM can be equipped with different detectors either for BSE or SE or both.

The formation of an SEM image based on the SE mode is the most widely used imaging mode since secondary electrons are abundant and their yield (the number of SE per primary electron) is high, which can even exceed unity as can be clearly seen in Figure 3.7. SEs are highly topography-related (i.e., surface texture and roughness) since they are only produced near to the surface of the sample, typically within a few nanometres.[77] This means that SE electrons have very small exit depths and hence any changes

in the surface topography of the sample will alter the sampling depth which in turn will affect the number of the emitted SEs that reaches the detector. Therefore, the larger the sampling depth the lower the number of SE that can be collected. Hence, bright areas on the image correspond to parts of the sample where large numbers of secondary electrons are emitted relative to other areas on the surface of the sample which would appear darker. This topographic contrast is used to form the SEM images.[77, 80]

In the backscattered electrons imaging mode the number of the emitted BSE largely depends on the atomic number of the atoms that reside on the surface of the imaged sample. Thus, the amount of BSE increase as the atomic number increases which means bright areas indicate regions where higher concentrations of elements of high atomic numbers present. Images formed based on BSE imaging mode differentiate between areas with several chemical composition specifically when the average atomic number in these areas is different. For more details about the various imaging modes refer to references [77 and 80].

Figure 3.8 depicts a cross-section view for an SEM set-up showing its important components. The SEM must be operated under high vacuum conditions to reduce the number of collisions between the electron beam and the atmosphere in the sample chamber. As a result the attenuation effect is minimised and consequently the collection efficiency of the emitted electrons is enhanced. An electron gun produces a beam of electrons which are then accelerated by applying a high voltage between the electron gun and the anode. A number of electromagnetic lenses are used to finely focus the beam onto the surface of the sample. Scanning coils are employed to manipulate the beam and move it across the sample surface to create the image.

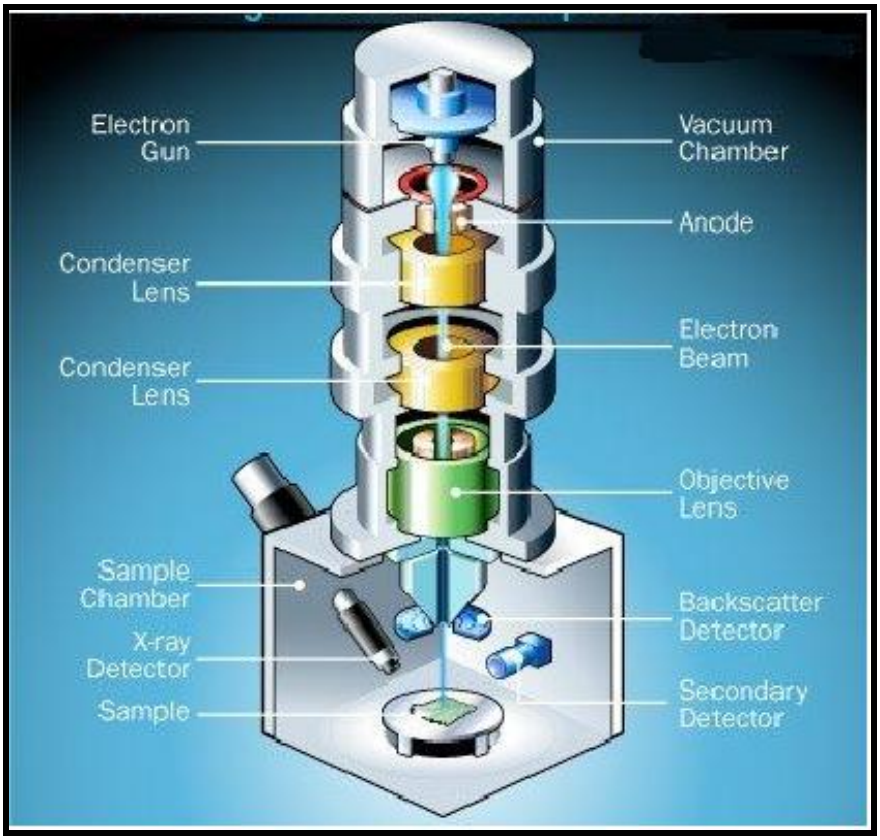

Figure 3.8 Schematic cross-section of a typical scanning electron microscope.

In this work an FEI Nova 200 dual-beam SEM device located at King Abdul Aziz City for Science and Technology (KACST) in Saudi Arabia was used to investigate the grown samples. This SEM has a precise focused ion beam (FIB) feature which is valuable in etching and cutting cross-sections of the sample so, more images can be taken.

3.5Atomic Force Microscope

The Atomic Force Microscope (AFM) has been widely used to create a three-dimensional profile of samples' surfaces on a nanoscale. This is achieved by monitoring a deflection of a very fine and flexible cantilever when it is scanned over an uneven surface. Importantly, AFMs are also extensively applied to estimate the sample's surface roughness.

Generally, an AFM is composed of a very sharp tip attached to the free end of a flexible cantilever, a laser source, a photodiode and a piezoelectric scanner as depicted in the simplified Figure 3.9. When the tip is scanned over the surface of the sample various forces such as the Van der Waals, electrostatic and magnetic forces will interact with the tip leading either to a static deflection of the cantilever when the tip is actually in contact with the surface or a change in the fundamental resonant frequency of the cantilever when the tip is brought very close to the sample's surface.[81]

In the first case the AFM is operated in the contact mode where the tip touches the surface as it is moved but when the cantilever is vibrated hence the AFM is said to operate in dynamic or non-contact mode. In the case of the contact mode, the magnitude of the cantilever deflection can be precisely measured by shining a laser beam on the back of the tip and continuously monitoring the reflected beam changes which can be directly related to the deflection magnitude. Therefore, the cantilever displacements can be converted into electrical signals and then processed for creating an image.

However, for the non-contact mode the cantilever is mechanically vibrated at or close to its natural resonant frequency utilising a piezoelectric crystal. The oscillated tip is systematically scanned over the surface of the sample and the oscillation is monitored where any changes in the oscillation wave properties such as frequency, amplitude or phase is attributed to the surface features and hence topographical images can be created. For more information about the operating modes, their advantages and disadvantages and the physics involved the reader is advised to see references [78 and 81].

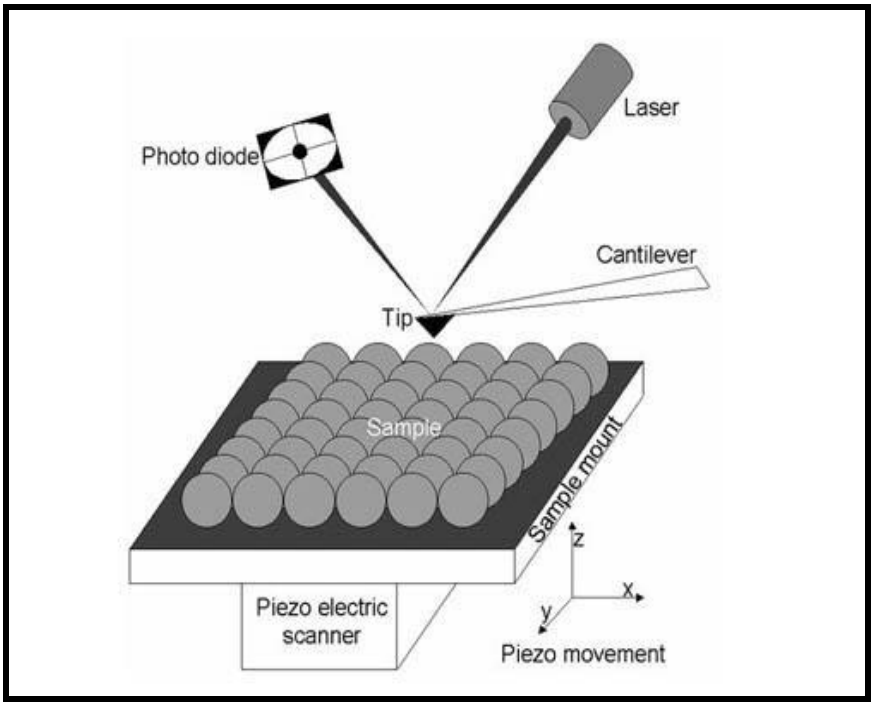

Figure 3.9 Drawing to show the working principle of an AFM.

In this work, the roughness values of the studied samples were determined using a Vecco di CP-II AFM with lateral resolution of ~ 0.1 nm and is available at the King Abdul Aziz City for Science and Technology (KACST) in Saudi Arabia. The AFM was operated in the contact mode.

3.6Photoluminescence Spectroscopy

Scientifically, luminescence refers to a stimulated radiative transition leading to a spontaneous emission of light when certain materials are effectively excited. It is nonthermal radiation as opposed to blackbody radiation. Luminescence is significantly important for mankind because in almost every spot on Earth people are heavily dependent on luminescent phosphors to lighten up their households, offices...etc. For example, fluorescent lighting tubes produce light by converting the ultraviolet radiation emitted by toxic mercury vapour into a visible light via rare earth based phosphors.[33]

Luminescence in general is a collective term and can be broadly classified into several categories based on the type of the excitation source. For instance, photoluminescence (PL) refers to emission of light produced by a luminescent material when it is excited by electromagnetic radiation (photons) while in the thermoluminescence process the excitation process is carried out thermally. Similarly, electroluminescence occurs when an electrical current is passed through the luminescent material and so on. Investigating the emitted light from an excited material is significantly an important step to evaluating the crystal quality, to determining the composition of the material and to exploring the energy levels associated to dopants and active defects present.

Photoluminescence spectroscopy is an invaluable tool largely used to investigate the optical properties of a material prior to considering device fabrication. PL experiments are highly appreciated over the other types of luminescence experiments for optically studying material where contact or junction technology has not been satisfactorily established. For instance, the PL technique can be beneficially applied to excite high resistive material where electroluminescence is inadequate or impossible.[33] PL is considered

a surface sensitive experiment where emitted photons are generated within the topmost area of the excited sample. For example, when a ZnO sample was excited using a He-Cd laser (3.81 eV) nearly most of the laser energy was absorbed by the first 40 nm of the sample surface as was experimentally shown by ellipsometry measurements.[82]

PL process starts when a sample is optically excited. In the case of semiconductors, pairs of free carriers (electrons and holes) are created in the conduction and valance band respectively when a semiconductor is excited providing an appropriate source whose energy ($h\upsilon$) is greater than the energy gap (E_g) of the semiconductor. Since the excess energy ($h\upsilon$-E_g) can be expressed in terms of the thermal energy (kT) the generated free carriers will have a higher thermal energy thus will be out of equilibrium with the lattice. Therefore, the electrons and holes will have to lose energy in order to gain thermal equilibrium by rapidly and nonradiatvely relax, usually by giving up some energy to the lattice, to the lowest vibrational states at the extrema of the conduction and the valence bands. Such a relaxation process is so-called thermalisation. However, these thermally relaxed electron-hole pairs are still not energetically stable. As a result of such instability they will further relax by radiatively recombining together and emitting luminescence. Each pair of electron and hole where they have electrical opposite charges may be electrostatically bound by a few meV due to their mutual coulomb interaction forming a quasi-particle called an exciton. Such a small amount of binding energy is referred to as an exciton binding energy. Exciton is a spatially delocalised state and can freely wander through the crystal of a material because of its electrically neutral feature.[3, 22, 28, 33]

In general, free excitons can be created in both pure and doped semiconductors and can be bound to any potential minimum exist in

bandgap of the semiconductor. Such minima can be created by impurities or defects. In a real semiconductor (nominally undoped) material imperfections are inevitably present in the crystal lattice creating intrinsic point or structural defects such as vacancies, dislocations and interstitials. These defects can be treated like purposely inserted dopant atoms in the way that both will produce localised states in the bandgap of the semiconductors. These states can generally act as donors or acceptors based on their physical properties and the energy levels associated with these induced localised states are denoted by E_D and E_A for a donor and an acceptor respectively. It should be pointed out that donors and acceptors can be either neutral as well as charged.[3, 22, 28, 33]

A free exciton can combine with one of these states by exchange interaction between an imperfection (dopant or defect) and the particle (electron or hole) of the free excition and become localised around the imperfection creating various excitonic complexes. For example, a neutral donor-bound exciton is formed when an exciton is bound to a neutral donor while an ionised donor-bound exciton is produced when an ionised donor is involved and so on. A neutral donor consists of a positive ion and a bound electron providing an attractive potential to an exciton to capture. In 1958 such a four-body system was first proposed by Lampert.[83] Typically, excitonic features dominate the optical properties of the semiconducting materials where the optical absorption and emission processes are largely affected by the creation and the radiative recombination of excitons.[3, 33]

However, when a semiconductor with band gap energy of (E_g) is appropriately excited and the produced free carriers have been thermally relaxed a number of radiatively excitonic transitions can simultaneously result which give rise to various optical emissions. The thermalisation process as well as some of these different excitonic transitions are

schematically illustrated in Figure 3.10. It should be pointed out that radiative recombination of bound exciton to a localised state generates photons which are less energetic than those produced by the free (not localised) exciton recombination. The energy difference these recombinations gives the exciton localisation (binding) energy (E_{loc}) which is dependent on the nature of the state.[81] In the case of a donor, this means different donors have distinct and characteristic localisation energies.

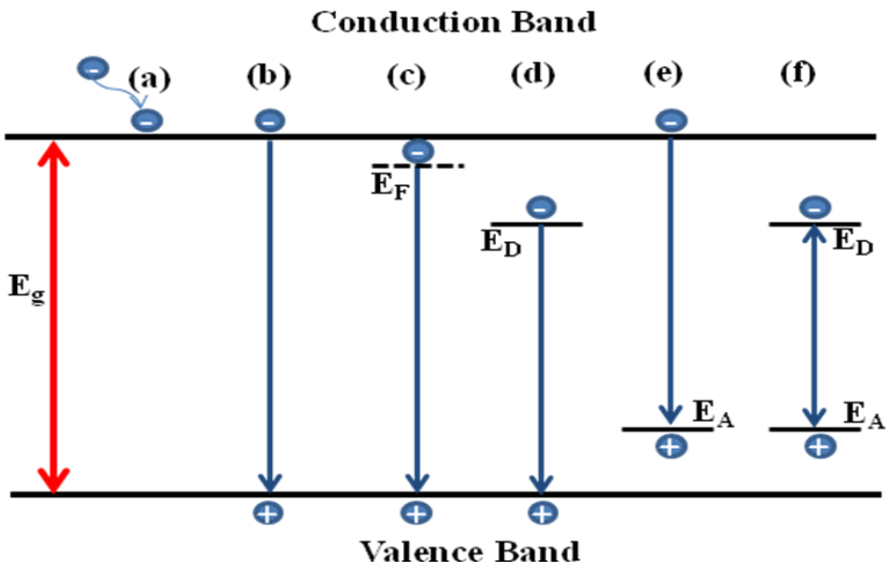

Figure 3.10 Schematic presentation simplifying relaxation process and various possible radiative recombinations in a semiconductor when it is excited by energy greater than the bandgap energy: (a) themalisation process of free carriers (b) band-to-band transition, (c) free exciton transition, (d) donor to free hole transition, (e) free electron to acceptor transition, (f) donor-acceptor pair transition.

Band-to-band transition usually takes place at energies equal to or slightly higher, due to thermal energy (k_BT), than the bandgap energy of a semiconductor as indicated by process (b) in Figure 3.10. This type of transition can be clearly observed in very high pure bulk crystals where bound excitons are not dominant especially at high temperature since bound excitons will thermally dissociate into free carriers.

Free exciton (Fx) transition occurs at a slightly lower energy than the bandgap energy where the energy difference accounts for the exciton binding energy. Free exciton emission becomes evidently clear as temperature increases since bound excitons would have sufficient energy to liberate from their localised states. However, due to the splitting effect of the energy band of a crystalline material a number of different free exciton emissions can be spectrally detected. For example, the valance band in ZnO is split into three different sub-bands labelled, previously mentioned in section 1.2, A, B, C because of the crystal field and the spin-orbit interaction. Thus, three different free excitons transitions can occur based on the associated valance sub-band and are referred to as Fx_A, Fx_B, Fx_C respectively. Assuming a simple hydrogenic model since the electron can orbit around the hole as if this were a hydrogen-like atom the transition energy of the free exciton for a given material and at a specific temperature T can be determined by[81]

$$\mathrm{E}_{FX}(T) = E_g(T) - E_{\mathrm{ex}}^{\mathrm{n}}, \quad E_{ex}^{n} = \frac{m_r e^4}{2(4\pi\varepsilon_0\varepsilon_r\hbar)^2 n^2} \tag{19}$$

where E_{g} and E_{ex}^{n} are the bandgap energy and the free exciton binding energy respectively. m_r is the reduced electron-hole mass and n is an integer number ≥ 1 which indicates the ground and the various excited states of the exciton. ε_0 and ε_r are the dielectric constant in vacuum and relative dielectric constant of the material respectively while $\hbar = h/2\pi$, h being Planck's constant.

From eq. 18 it can be clearly seen that the exciton binding energy is inversely proportional to the relative dielectric constant of a given material. Therefore, the exciton binding energy for a wide-band gap, such as ZnO, semiconductor is large (60 meV) in comparison to the narrow-band gap semiconductors where their dielectric constants are considerably smaller.

The dielectric constant which is a characteristic feature of materials will induce an electrostatic shielding effect between the electron and the hole which results in a reduction in the attractive columbic force and subsequently an exciton of a small binding energy is formed.

As previously stated free excitons have the ability to move through the lattice and they can be attracted by various impurities or lattice defects hence they become localised. As a result different excitonic complexes are created which generally are called bound excitons. The radiative transitions of the bound excitons are spectroscopically characterized by very sharp peaks since bound excitons are localised thus they do not possess kinetic energy. Consequently they are not greatly influenced by the thermal broadening effect due to Boltzmann kinetic energy distribution.[81] These excitonic emissions are referred to as free-to-bound transitions since they occur between free carriers (holes or electrons) in the relative semiconductor band and the localised states in the band gap. The energy position of a bound exciton transition always appears in the luminescence spectrum at the lower energy side of the free exciton. The recombination energy of a bound exciton as a function of temperature (T) is given by[81]

$$E_{BX}(T) = E_g(T) - E_{ex} - E_{Loc} \qquad (20)$$

where the term E_{Loc}, as previously stated, is the bound exciton localisation energy which is the required energy to bind the free exciton to the localised state (imperfection). Generally, neutral donor bound exciton emission is denoted by D^oX while neutral acceptor-bound exciton is referred to as A^oX. Similarly, the ionised donor and acceptor-bound exciton are labelled as D^+X and A^-X respectively. These types of exitonic recombinations are illustrated in Figure 3.10 by processes (d) and (e).

Donor-Acceptor Pair (DAP) transition: Semiconductor materials often have both donors and acceptors in varying degrees. Donors and acceptors have opposite charges hence they can attract each other and form a pair which can be thought of as a stationary molecule. Above room temperature, both donors and acceptors can be thermally ionised. Also, when donors and acceptors are sufficiently close to each other they can be ionised due to the compensating effect where the wavefunction of the donor electron and the acceptor hole will overlap. As a consequence, the electron can be captured (or compensated) by the acceptor leading to an ionised donor and an ionised acceptor[58]. However, when the semiconductor is excited the electron-hole pairs (excitons) can be captured by the ionized donor (D^+) and acceptor (A^-) sites, forming neutral donors (D^0) and acceptors (A^0) centres. In returning to equilibrium states, some electrons on neutral donors will recombine with holes on neutral acceptors giving rise to a donor-acceptor pair transition (DAP). This transition can be described by[84]

$$D^0 + A^0 \rightarrow h\nu + D^+ + A^- \qquad (21)$$

Other frequently observed transitions in the PL spectrum of a semiconductor associated with the excitonic emissions are phonon replica and two electron satellites. In a crystal at any temperature above zero Kelvin there will be a thermal energy ($k_B T$) which is enough to cause every atom to vibrate around its equilibrium position in a simple harmonic motion. The amplitude of vibration rises with increasing temperature. However, since the lattice atoms are bound together they are oscillating collectively around their equilibrium positions at their resonant frequencies. Similarly to the photon concept the associated vibrational energies are quantised and referred to as phonons. By analogy to a photon, phonons can be thought of as a particle or a wave. The vibrational frequencies are

determined by the phonon modes of the lattice which can be studied by a variety of techniques such as Raman spectroscopy or infrared scattering.[85]

Generally, phonons can be subdivided into two main different groups. If adjacent lattice atoms oscillate in the same direction, it is described as an acoustical phonon mode whereas the optical phonon modes occur when two adjacent atoms vibrate in the opposite direction.[85] Phonons exhibit polarisation properties. Both modes can be either transverse or longitudinal according to the orientation of the polarisation wave associated with the phonon as it propagates through the lattice.[58] Transverse phonons are created when atoms are oscillating normal to the wave vector and longitudinal phonons are seen when direction of the oscillation is parallel to the wave vector.

Since ZnO is a polar semiconductor possessing a wurtzite symmetry with four atoms per unit cell there are a total of 12 phonon modes (3 acoustic and 9 optical) present. They are summarised in Table 3.1[29]

Table 3.1 Phonons modes in ZnO wurtzite crystal

Mode type	Number of modes
Longitudinal acoustic (LA)	1
Transverse acoustic (TA)	2
Longitudinal optical (LO)	3
Transverse optical (TO)	6

Phonons can couple with electrons, holes and excitons in the same way as photon does. This interaction can lead to equally spaced phonon replicas occurring at lower energies with respect to a zero-phonon transition (ZPL).

For a polar crystal like ZnO, a strong longitudinal electric field created by the oscillating dipole due to the motion of negative and positive ions in the unit cell is expected. Hence, excitons interact more strongly with longitudinal optical (LO) phonons than the transverse optical (TO) phonons.

Generally, when an optical transition occurs one or more phonons can be emitted. The energy of the emitted photon is given by[86]

$$h\upsilon_{m,n} = E_{ZPL} - mE_{LO} - nE_{TO} \qquad (22)$$

where m is the number of LO phonons, E_{LO} is the energy of LO phonons, n is number of TO phonons and E_{TO} is energy of TO phonons. The greater the number of generated phonons the lower the transition probability and the weaker the intensity is. The characteristic minimum optical phonon frequency ZnO is about 72 meV (580 cm^{-1}).[23, 29, 30] The oscillatory structure of the PL spectrum of the ZnO bulk shown in Figure 1.5 has an apparent 72 meV energy periodicity.

The two-electron satellite (TES) transition is another secondary characteristic optical feature associated with the neutral donor bound exciton emission. When an exciton bound to a neutral donor recombines predominantly the donor electron stays in its ground (initial) state (1s). However, there is a possibility that a portion of the excitonic energy may get absorbed by the donor electron promoting the donor to an excited (final) state (2s,2p). The resulting transition, called TES, is red-shifted from the original emission of the bound exciton and appears in the spectrum as a characteristic satellite structure. The energy spacing between the D^oX and the associated TES transition is distinct for individual donors. Figure 3.11 illustrates the TES process.

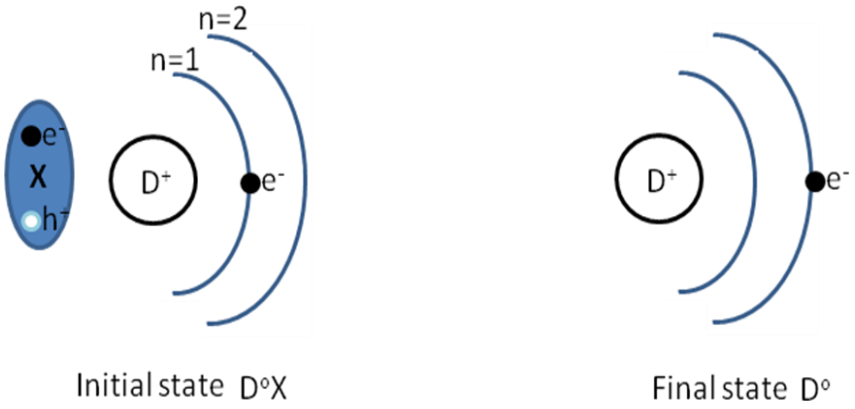

Figure 3.11 Diagrammatic sketch showing the two-electron satellite transition during the neutral-bound-exciton recombination process. Initial state represents an exciton (X) bound to a neutral donor where the donor electron remains in the ground state. In the final state (TES) the electron of the donor is left in an excited state.

Because the partial energy transfer from exciton recombination to the final state of the bound electron is less probable than the direct excitonic transition to the donor ground state the intensity of the TES emission is much weaker in comparison to the intensity of the main bound exciton transition.

Using the hydrogenic effective mass approach the emission energy of a TES line is given by[25, 58]

$$E_{TES}^{n} = E_{Bx} - \Delta E = E_{Bx} - E_d\left(1 - \frac{1}{n^2}\right) \qquad (23)$$

where n is principle quantum number, E_{Bx} is the transition of the bound exciton in its ground state (1s) and E_d is the donor (acceptor) binding (or ionisation) energy which is defined as the energy needed to dissociate the electron (hole) from the donor (acceptor). Using equation (23) the donor excitation energy (ΔE) which is the energy separation when the donor is in its first excited state ($n = 2$) and when it is in its ground state ($n = 1$) equals to $3/4\,E_d$. Therefore, the observation of TES transition is very useful in

determining the donor binding energy. Empirically, it was found that the donor binding (ionisation) energy correlates linearly with the bound exciton localisation (binding) energy as $E_{Loc} = \beta \cdot E_d$ where β is the proportionality factor. This linear dependency can be generally expressed as

$$E_{Loc} = A + B \cdot E_d \qquad (24)$$

where A and B are constants, typically between 0 and 1, and must be determined experimentally. Such a relationship is known as Haynes rule.[87] Because the exciton is electrically neutral the amount of energy that is required for the bound exciton to break free of the donor is less than that needed to liberate the electron (negatively charged) from the donor. This statement agrees well with Haynes rule.

Two different excitation sources were employed to carry out photoluminescence measurements. Above-gap excitation with a Kimmon Koha Co. Helium cadmium (He-Cd) laser operating at 325 nm (3.81 eV) was used to study the near band edge spectrum of ZnO, the host material, as well as to indirectly excite the RE ions since none of the RE-related energy levels are in resonant with 325 nm. The laser output power was approximately 15 mW. In-gap excitation was provided using the 488 nm and 514.5 nm lines of an Ar+ laser (Spectra-Physics model 2085) to directly excite RE ions since these wavelengths closely match some energy levels of RE-related states therefore they can be populated.

Figure 3.12 shows a schematic drawing of the PL set-up where the investigated samples were mounted in a copper holder using a silver paste to provide better thermal conductivity. The sample holder was then screwed to a cold finger and placed inside the optical tail of an Oxford He Microstat. The cryostat is connected to a helium storage dewar with a transfer tube. The samples were cooled by helium gas being continuously flowed over the

back side of the finger. However, before the helium was introduced the cryostat was evacuated with a pump to be thermally insulated from outside. Varying temperatures to carry out PL temperature dependent experiments was achievable through a resistive heater (an Oxford Instrument Intelligent Temperature Controller) which has stability of approximately 0.1 K.

Three different types of spectrometers were employed to detect the emitted PL signals in three different spectral regions. In the visible region the PL spectra were recorded with a high-precision TRIAX 320 spectrometer equipped with a liquid nitrogen cooled CCD detector. The TRIAX 320 spectrometer has a focal length of 320 mm and an F number of F/4.1. The CCD detector consists of a large chip of silicon divided into a two-dimensional matrix of (1024 x 1024) pixels and was cooled using liquid nitrogen to reduce the thermal noise.

In the UV region the PL signals were first collimated by a short focal length lens and the collimated light was focused using a nearly f-matched focusing lens to a high resolution monochromator (1000M HORIBA Scientific).The focal length of the monochromator is 1 m and its F number is F/8. The dispersed PL signal was detected by a water-cooled photomultiplier tube (PMT) operating on a photon-counting mode at 1800 V.

To detect PL signal in the infrared the region, a dewar-type InGaAs detector with a built-in preamplifier (G7754-03) fitted to a single-grating spectrometer (0.25 M Spex Minimate) was utilised. The spectral response range of the detector is (1.2 to 2.4) μm with highest detectivity at 2.0 microns. The laser light was mechanically chopped with a rotary blade chopper and the signal from the detector was sent to a lock-in amplifier before it was recorded. The lock-in amplifier was synchronised at the chopping frequency hence signals only at this frequency was selected in order to reduce the noise level.

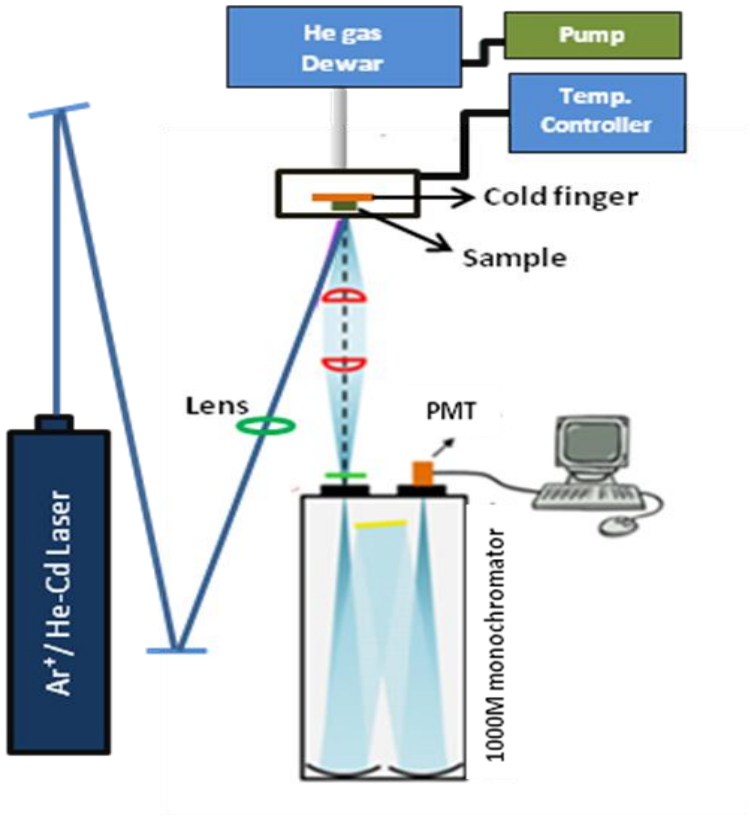

Figure 3.12 The experimental arrangement of the photoluminescence (PL) measurements.

3.7Combined Excitation and Emission Spectroscopy

During a growth process identical doping atoms may occupy a number of different lattice sites which means different charge distribution around the dopants and hence various crystal symmetries are experienced by these dopants. As a result, a specific dopant-related spectral transition will generally be altered and accordingly appear at different energies. A Combined Excitation-Emission Spectroscopy (CEES) technique was employed to identify and investigate the optically active sites of the dopants (Eu and Er). Using such a spectroscopic technique, the time needed for acquiring emission and excitation spectra is greatly shortened since both spectra are synchronously recorded. In the CEES measurements, a tunable radiation source, usually a dye laser, is progressively scanned over

specifically narrow energy levels of the atom, of interest while simultaneously analysing the corresponding PL emissions.

In this work a visible tunable dye laser (Spectra-Physica model 375) was used. A lasing medium, a new batch of an organic dye solution, was prepared as follows: one gram of Pyrromethene 546 was well dissolved in 1.5 litres of a liquid mixture consisting of Benzyl alcohol (BeOH) and Ethylene glycols (EG) where the mixing ratio was (1:4).This yielded a concentration of the Pyrromethene of 2.54 x 10^{-3} mol/L. The dye solution was circulated from a reservoir using a small liquid pump through a specially-designed nozzle to produce a sheet-like stream. The dye laser was optically pumped using the 488 nm spectral line of a high power argon laser (Spectra-Physics model 2080). The wavelength of the dye laser was automatically tuned using a birefringent crystal rotated by a micro stepper a micro-stepper motor which was remotely operated via a computer. The laser tuning range was varied between 520 and 550 nm. The maximum laser output power was approximately 150 mW at 4 Watts of the 488 mn pumping power.

3.8Thickness Measurements

Thickness of the investigated films was determined by a profilometer (Veeco DEKTAK 150) where a stylus is moved across the surface of the film. The height difference between the deposited film and the surface of the substrate gives the thickness of the film. A profile of the surface is recorded and hence an average value of the thickness can be calculated. Figure 3.13 shows a surface profile of a film where its thickness is estimated to be ~ 300 nm. It should be mentioned that the substrate holder in the employed PLD system was specifically designed on the way that no film can be deposited on the corners of the sapphire substrate. This design

is beneficial where no chemical etching is needed to remove part of the grown film.

Figure 3.13 Surface profile of a pure ZnO thin film.

The average thickness values of the deposited films were found to vary between 280 and 410 nm. It should be pointed out that the thickness of the pure ZnO buffer layer was not measured. The buffer layer may get contaminated if it was removed from the chamber to do the thickness measurement, which then would adversely affect the subsequent film.

3.9 Energy-dispersive X-ray Spectroscopy (EDS)

Sintering process is considered one of the most consolidation methods. On a microscopic level, when a material is sintered many chemical and physical changes may take place during the sintering course. For example, chemical reactions between different species, chemical changes through vaporisation and oxidation. Also, inhomogeneity in the chemical composition and non-uniformity in the concentration of impurities can

occur. Physical changes can also happen. For instance, formation of interfaces/grains boundaries, alteration in the pore and grain sizes and phase transformations such as melting and crystallisation can be seen. In order to investigate the chemical composition of surface of the PLD targets after being sintered EDS measurements were performed using .an energy-dispersive spectrometer (Oxford instruments X-Max) attached to SEM (JOEL JSM-6510 LV).

EDS is widely used to quickly obtain localised compositional information of the top layer of a surface of solid sample. The scientific concept of the EDS technique is based on generating characteristics x-rays from the sample under investigation when its surface is irradiated with a tightly focused electron beam with a appropriate energy. These characteristics x-rays are used for chemical identification. In a typical EDS spectrum the horizontal axis corresponds to the x-ray energy while the vertical axis represents the x-ray counts. The integrated intensity, the area under the x-ray peak, is proportional to the concentration of the corresponding element.

The EDS measurements were taken for seven selected ZnO PLD targets. One is pure ZnO. Three targets doped with Er and the remaining three ZnO targets are doped with Eu. The concentration of Eu and Er are 0.025, 1 and 5 at. %. EDS spectra of various sample are shown in Figures 3.14, 3.15 and 3.16. Different characteristics x-ray peaks were identified and clearly labelled in the spectra. The EDS measurements give us the composition and the concentration of the chemical species which reside in the sampled area covered by the X-ray beam (~ 8 microns) as shown in Figure 3.17 of an SEM image of a surface of a PLD target. It should be mentioned that the peak at zero KeV is the “zero noise peak” which is caused by tiny amount of electrical noise and it is not specific to the sample.

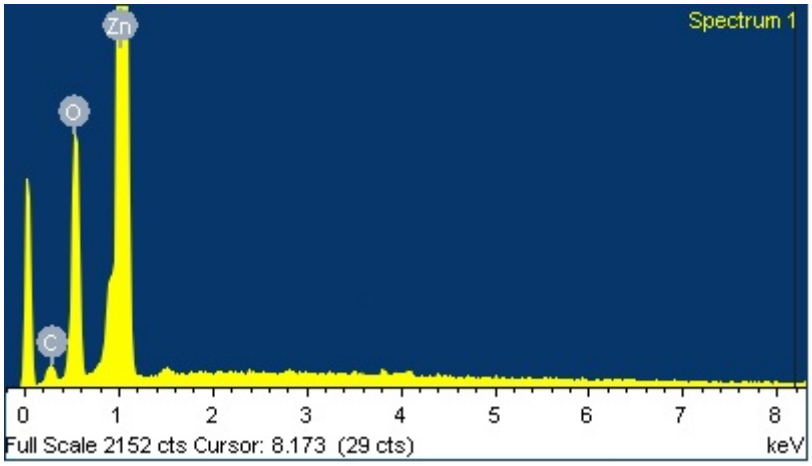

Figure 3.14 EDS spectrum of a Pure ZnO PLD target.

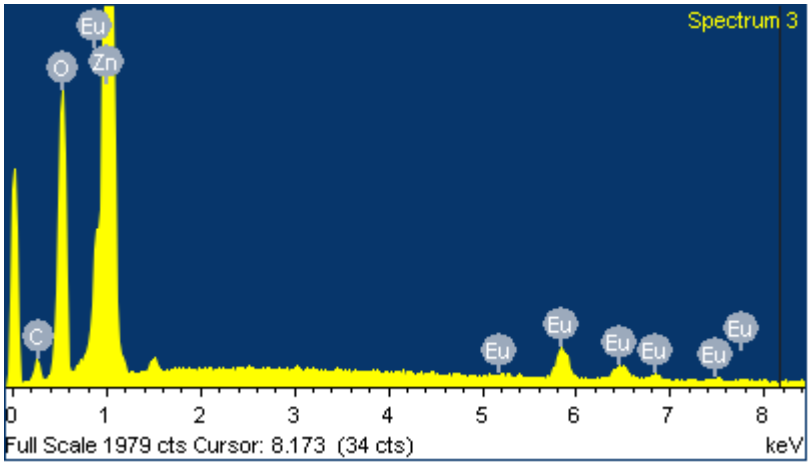

Figure 3.15 EDS spectrum of ZnO:Eu (5 %) PLD target.

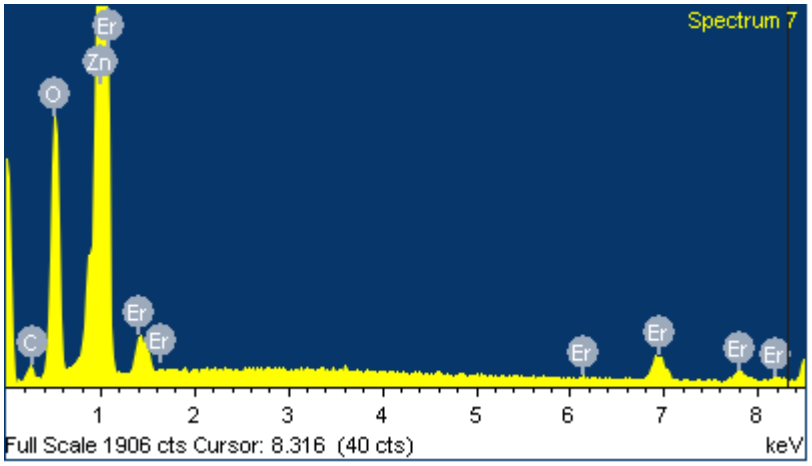

Figure 3.16 EDS spectrum of ZnO:Er (5 %) PLD target.

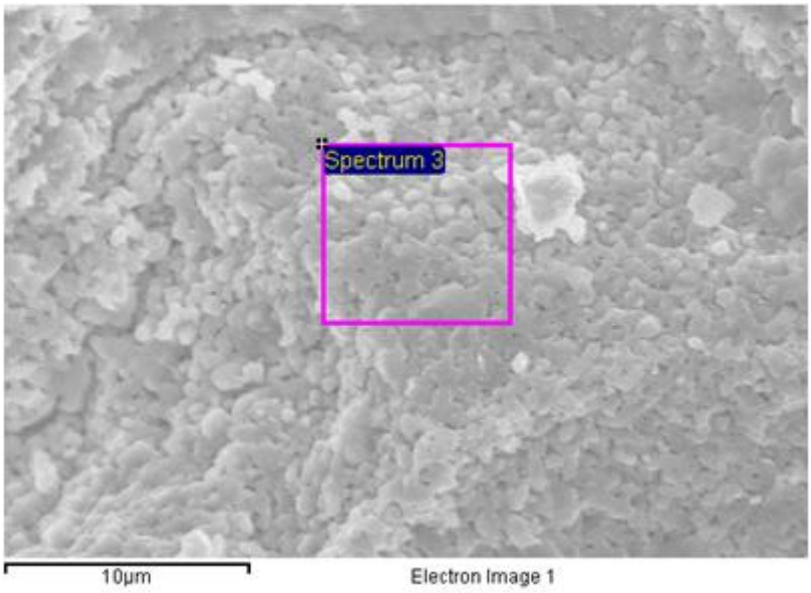

Figure 3.17 SEM image of the ZnO:Eu (5%) PLD target where the sampled area is highlighted by the drawn square.

It should be clearly stated that getting accurate compositional information based on EDS measurements is a very difficult task to perform. For example, a flat-polished standard material of a precisely known concentration of every element present on the sample must be obtained and used under the same experimental conditions when the EDS measurements taken for the PLD targets. However, for the EDS results presented here and shown in Table 3.2 no standards were used. Thus these results are generated by used processing software which cannot be deemed accurate and can only be accepted for stoichiometric comparisons. The used software has a built-in database for a number of standard materials which they were used to calculate the concentration of the element detected in the investigated PLD targets.

Table 3.2 Compositional study based on EDS measurements for various PLD targets.

Target	Nominal concentration of RE (at. %)	Measured concentration of RE (at. %)	Measured concentration of O (at. %)	Measured concentration of Z (at. %)	(Zn/O) ratio
Pure ZnO	0	0	50.25	32.28	0.64
ZnO:Eu	0.025	0	41.42	42.86	1.03
	1	0	46.54	39.81	0.85
	5	1.25	50.52	30.34	0.60
ZnO:Er	0.025	0.88	51.18	33.54	0.65
	1	0.29	50.91	34.47	0.67
	5	1.54	52.36	33.98	0.64

From the results presented in Table 3.2 it can be seen that almost all targets are nonstoichiometric and zinc deficient. Therfore, it can be assumed that sintering has played a role in changing stoichiometry of PLD targets. It is also noted that the measured concentrations of RE atoms do not match the nominal concentrations and it may be due to the fact that EDS is a localised analytical technique. It would have been advantageous if the used EDS has the capability to produce an element map. Such feature would show the spatial distribution of elements.

Chapter 4

RESULTS FOR ZnO: Eu^{3+} SAMPLES

4.1Structural Characterisation

Generally speaking, the total stress found in thin films consists of two components, namely, intrinsic and extrinsic, based on the origin of the stress. Intrinsic stress is caused by impurities, defects and lattice distortions.[67] The extrinsic stress component is caused by differences in some physical parameters of the films and the substrates, such as lattice constants and thermal expansion coefficients.

The lattice mismatch and the difference in the linear thermal expansion coefficients between the sapphire substrate and ZnO are 18.3% and -34% respectively.[69] In this work dopants (Eu and Er) are introduced into the ZnO films. These dopants have different ionic radii and oxidation compared to those of Zn^{2+} ion as previously reported in Chapter One. Therefore, it is assumed that these two components will induce residual strains in the films of various kinds and to varying degrees, leading to degraded structural properties.

To investigate the effect of these strains on the film's properties and to try to minimise the strain by reducing the lattice misfit component, two sets of RE-doped ZnO films were produced, one with and one without a low-temperature pure ZnO buffer layer. The growth procedure was described previously in Section 2.33. Both sets of samples contained the same nominal concentration of Eu dopants.

Generally, residual strain caused by the lattice misfit between a thin film and a substrate, as in the case of ZnO and sapphire, is partly relived by the generation of a high concentration of dislocations at interface region. These

threading dislocations will then propagate towards the thin film, which will adversely affect the film quality.[88] When a thin layer is deposited at a low temperature atoms arriving to the substrate will not have sufficient mobility to move freely. Therefore, high concentration of point defects will be generated. It was reported that theses point defects will interact with the threading dislocations preventing them to reach the thin film so the film quality is expected to improve.[89]

The X-ray diffraction pattern of pure ZnO and Eu-doped ZnO films having different concentrations of Eu are shown in Figure 4.1. All films were found to possess a single-crystal hexagonal structure and to be strongly oriented along the *c*-axis. The nominal Eu concentration for each sample is shown above its spectrum. The (006) diffractive peak of the sapphire substrate is also observable.

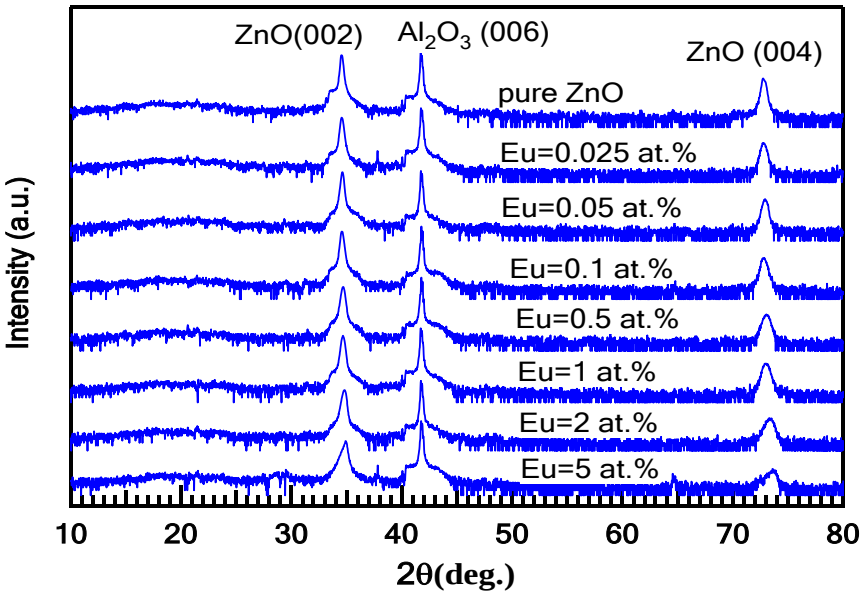

Figure 4.1 XRD spectra of ZnO:Eu samples. The Y-axis is plotted on logarithmic scale and has been vertically offset for clarity.

Importantly, no unwanted diffraction peaks related to the Eu_2O_3 phase were detected. This could imply a successful insertion of Eu atoms into the ZnO

host lattice. According to the powder diffraction file (PDF) 021-0390, the strongest diffraction peaks of Eu_2O_3 are (222) and (400) which they should appear at $2\theta = 28.49$ and 33.01, respectively.

In Figure 4.2 it can be seen that the intensity of the (002) diffractive peaks in general declines as the Eu concentration increases, which would indicate a deterioration in crystallinity because of lattice structure distortion due to residual stress caused by the incorporation of the relatively large Eu ions and caused by the misfit of the lattice constant and of the thermal coefficients between ZnO and sapphire, as previously indicated.

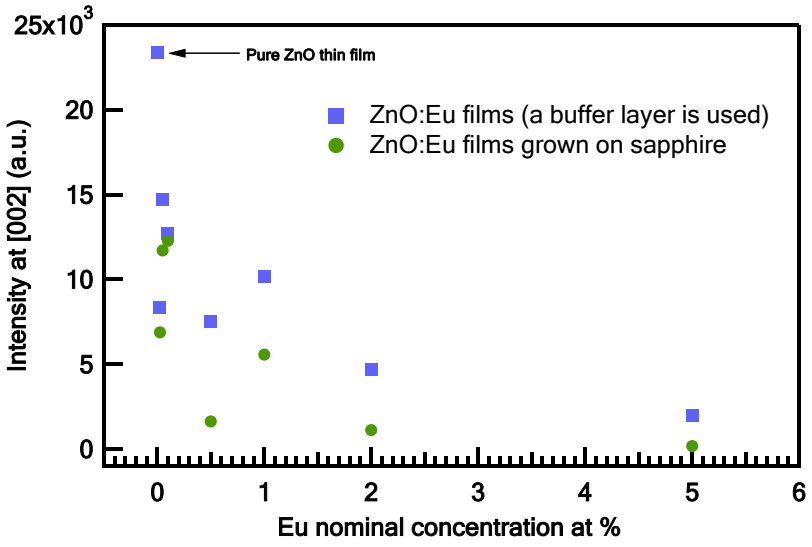

Figure 4.2 Plot of the absolute intensities of (002) peaks various ZnO:Eu samples.

It should be pointed out that comparing intensity count of a specific XRD peak between different samples can be generally accepted as an indication to evaluate the, crystallinity, structure quality. However, in XRD measurements there are many factors which can directly influence the intensity of a diffracted x-ray beam. These factors can be grouped into two categories, instrumental and experimental-related. The x-ray diffraction intensity can be mathematically given by[90]

$$I_{(hkl)\alpha} = \frac{I_0 \lambda^3}{64\pi r}\left(\frac{e^2}{m_e c^2}\right)^2 \frac{M_{(hkl)}}{V_\alpha{}^2}\left|F_{(hkl)_\alpha}\right|^2 \left(\frac{1+\cos^2(2\theta)\cdot\cos^2(2\theta_m)}{\sin^2\theta\cos\theta}\right)_{hkl} \frac{\nu_\alpha}{\mu_s} \qquad (25)$$

Where $I_{(hkl)\alpha}$ = intensity of reflected x-ray from a lattice plane specified by Miller indices *hkl* in phase α. I_0 = the intensity of incident beam. r is the distance between specimen to the XRD detector. λ is x-ray wavelength. $\left(\frac{e^2}{m_e c^2}\right)$ is square of classical electron radius. I_α is volume fraction of phase α. μ_s is the linear absorption coefficient of the specimen. ν_α volume of the unit cell of phase α. $M_{(hkl)}$ multiplicity of reflection *hkl* in phase α. $\left|F_{(hkl)_\alpha}\right|$ is structure factor for reflection of *hkl* in phase α. $\left(\frac{1+\cos^2(2\theta)\cdot\cos^2(2\theta_m)}{\sin^2\theta\cos\theta}\right)$ is Lorentz polarisation and monochromatic correction. $2\theta_m$ is the diffraction angle of the monochromator. θ is Bragg angle.

Importantly, the full width at half maximum (FWHM) of an XRD diffractive peak is more widely accepted as an important parameter to evaluate the degree of crystallinity of materials. Figure 4.3 illustrates the FWHM values of the (002) ZnO diffractive peaks for different films belonging to both sets of samples as a function of the nominal concentration of Eu.

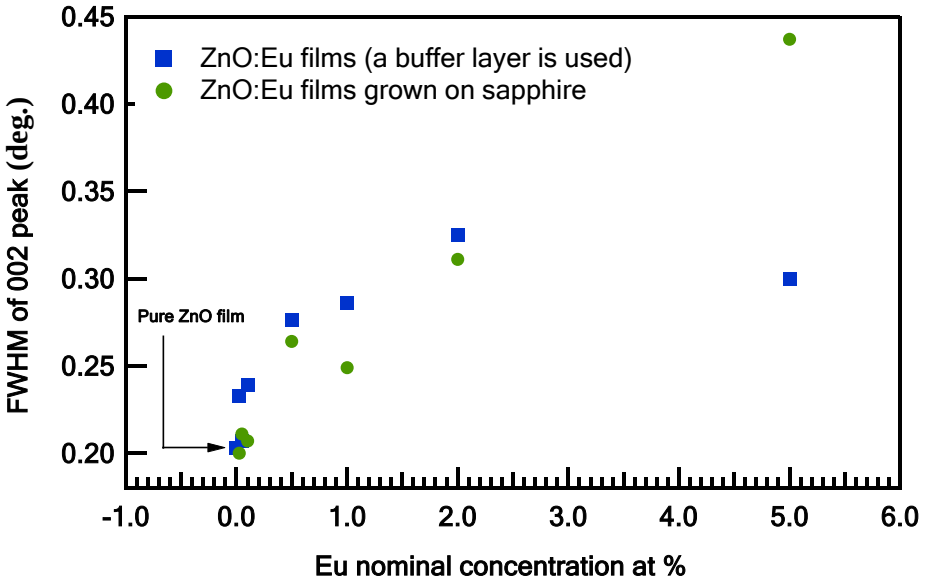

Figure 4.3 The full width at half maximum (FWHM) of (002) diffractive peaks for various ZnO:Eu samples.

As a general trend the FWHM for both series of samples become larger as more Eu ions are added into the films, indicating a reduction in crystallinity. Surprisingly, although the samples with a buffer layer show some improvement in terms of the intensity of (002) XRD peaks in comparison to the intensity of the other samples (without a buffer layer), the FWHM of (002) peaks are slightly wider for the samples with a buffer layer than for those grown on a bare sapphire, except for those samples having the highest concentration (5 %) of Eu atoms. Thus, the conclusion that can be drawn is that a low-temperature ZnO buffer layer is important to fabricating doped ZnO films containing high concentrations of rare earth ions that needed for devices.

Interestingly, the (002) XRD peak positions exhibit gradual changes when more Eu atoms are added into the films, as evident in Figures 4.4 and 4.5. The decrease in the intensity of the diffractive peak can also be clearly seen.

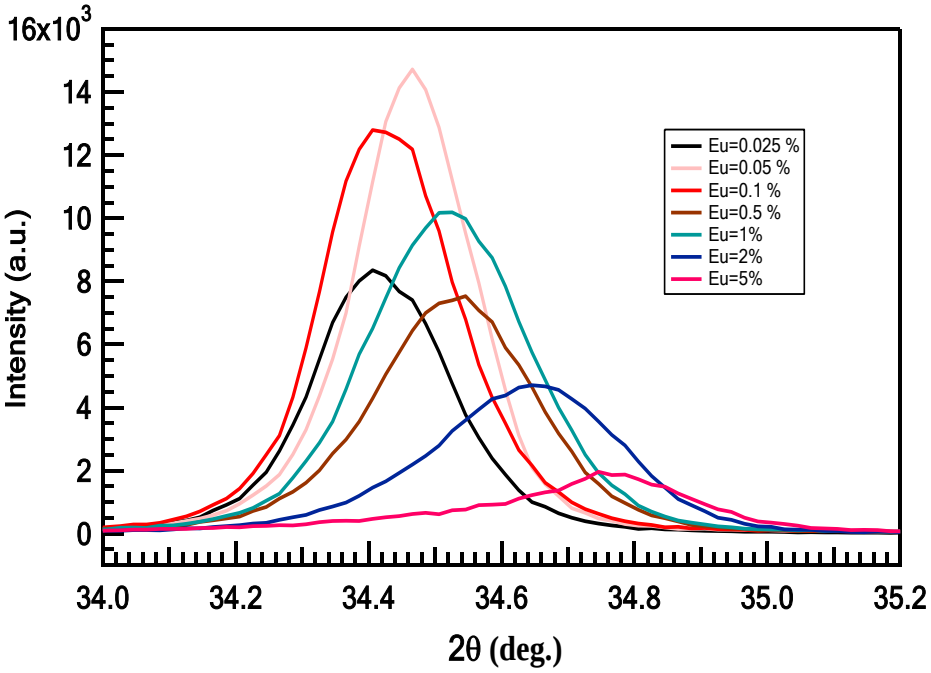

Figure 4.4 (002) XRD peak shifts for ZnO:Eu samples grown on a buffer layer.

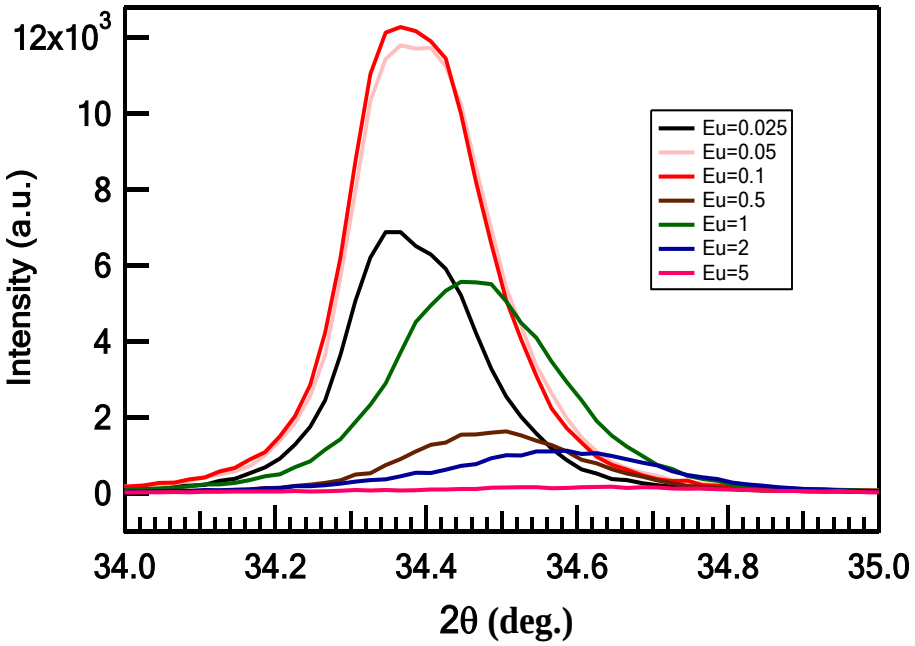

Figure 4.5 (002) XRD peak shifts for ZnO:Eu samples grown on bare sapphire.

For the sake of better clarity the data shown in Figure 4.4 and Figure 4.5 are re-plotted and presented in Figure 4.6 and Figure 4.7, respectively.

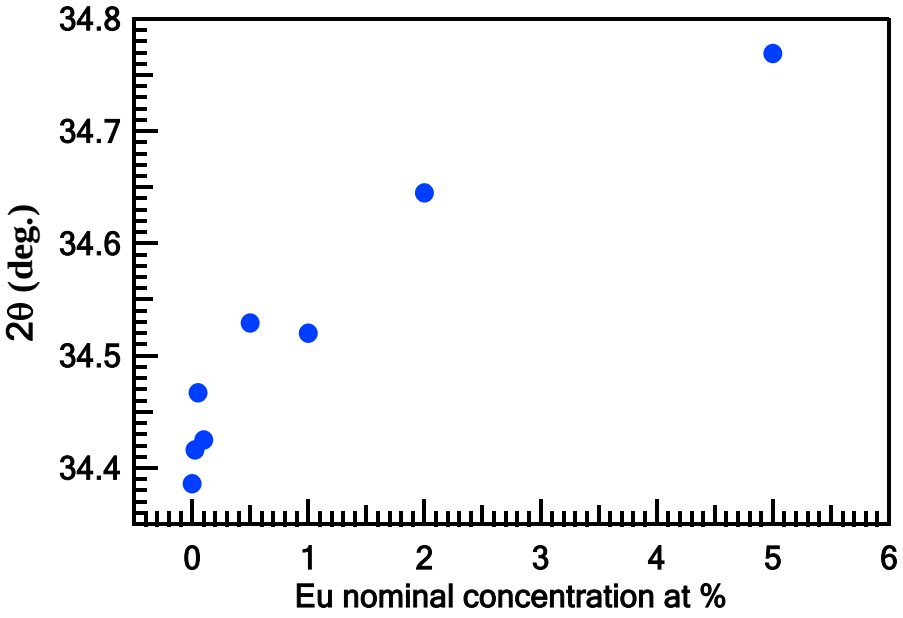

Figure 4.6 (002) ZnO XRD peak position for ZnO:Eu samples grown on a buffer layer.

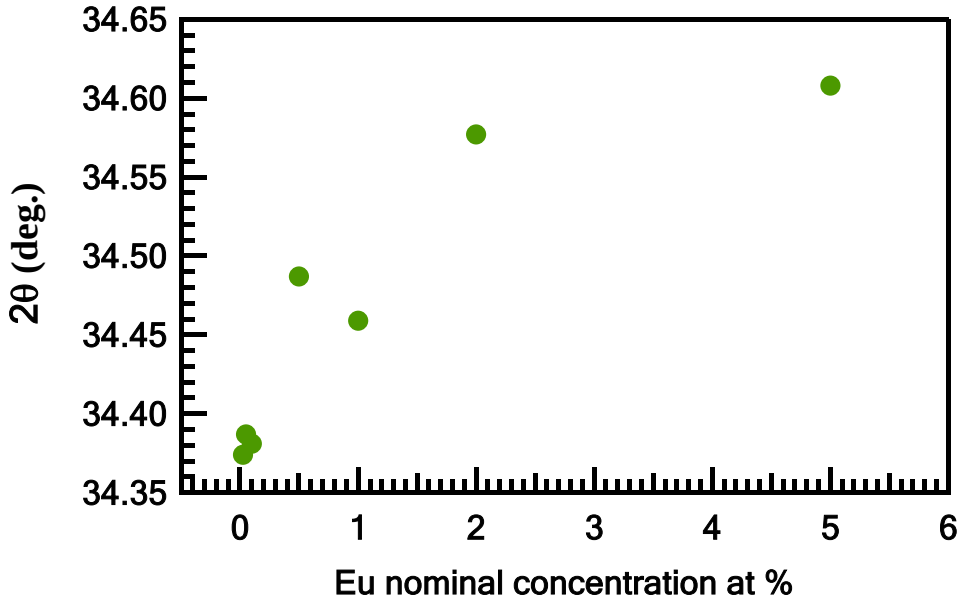

Figure 4.7 (002) ZnO XRD peak position for ZnO:Eu samples grown on a bare sapphire substrate.

It is known that residual strains cause a shift in the position of XRD diffractive peaks and induces structural disorders, mainly through an

increase in the grain boundary density which, leads in turn to a reduction in crystallite size. However, crystallite size can also be affected by other factors such as impurities and defects.[91] Figures 4.8 and 4.9 illustrate a reduction in crystallite size, as calculated by using Scherrer's formula, in relation to the nominal concentration of europium for both series of samples. It is evident that crystallite size decreases as more Eu atoms are doped. Scherrer's formula is given by[18]

$$d = \frac{0.9.\lambda}{B.\cos(\theta)} \qquad (26)$$

where d is average crystallite size, λ is X-ray wavelength, B is the full width at half maximum [(FWHM) in radians] of the diffractive peak and θ is the diffraction angle. The broadening of the diffractive line due to the XRD instrument was corrected by obtaining the diffraction spectrum of sapphire bulk (stress-free).

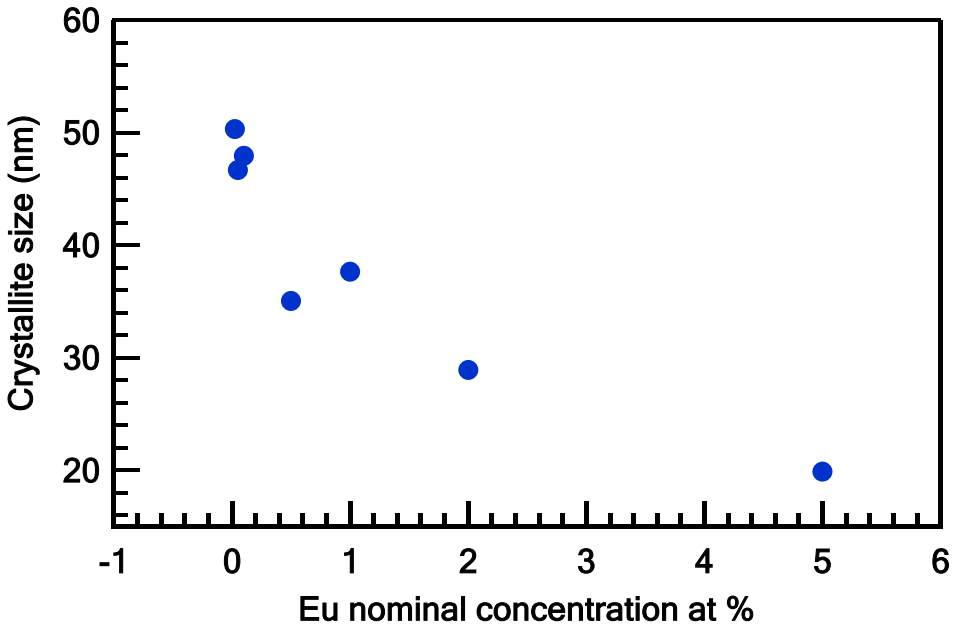

Figure 4.8 Crystallite size plot as a function of Eu nominal concentration for films grown on a bare sapphire substrate.

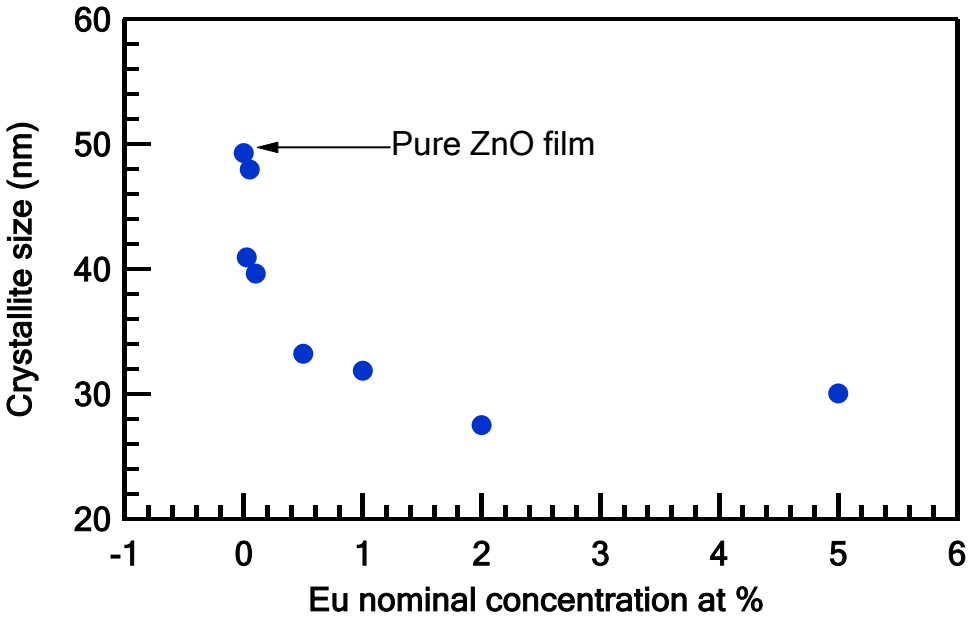

Figure 4.9 Crystallite size plot as a function of Eu nominal concentration for films grown on a low-temperature pure ZnO buffer layer.

The observed shift in the (002) XRD diffractive peaks can be reasonably interpreted if the lattice constants of ZnO are and the residual strain are determined. They can be readily calculated as described previously in Section 3.1 using equations (6), (7), (8) and (10).

Tables 4.1 and 4.2 summarise the calculated values of lattice constants, residual strains, crystallite sizes and unit cell volumes for all films from both sets of samples. Films with low concentrations of Eu from both sets exhibited tensile strain but became compressively strained as the Eu concentration increased. For example, from the data presented in Tables 4.1 and 4.2 the calculated stresses for film grown on a buffer layer at the nominal Eu concentration of 0.025 at.% rose from ~ -0.13 GPa to ~ 4.5 GaP as the Eu concentration increased to 5 at.% while the calculated stress for films grown on a bare substrate increased from ~ -0.7 GaP to ~2.3 GaP.

Surprisingly, films deposited on a pure ZnO buffer layer showed high tensile stress than films grown on bare sapphire. This observation does not

agree with what was expected. However, further study is absolutely needed to investigate this unexpected result. For example, it has been reported that growth parameters such as temperature plays an important role in the employment of a buffer layer whereby a high degree of strain relief was obtained when the temperature was optimised.[92]

Table 4.1 Lattice constants, strain and unit cell volume calculated values for samples with different nominal concentrations of Eu grown on a pure ZnO buffer layer.

Eu (at.%)	**FWHM (deg.)**	**Lattice constants (Å)**		**Unit cell volume ($Å^3$)**	**Crystallites size (nm)**	**Strain (%)**	**Stress (GPa)**
		c	***a***				
Pure ZnO	0.203	5.212	3.191	45.97	49.30	0.113	-0.525
0.025	0.233	5.207	3.189	45.85	40.95	0.028	-0.132
0.05	0.207	5.200	3.184	45.66	47.98	-0.115	0.536
0.1	0.239	5.206	3.188	45.82	39.65	0.003	-0.014
0.5	0.276	5.191	3.179	45.42	33.24	-0.290	1.348
1	0.286	5.162	3.179	45.45	31.87	-0.264	1.230
2	0.325	5.174	3.168	44.98	27.52	-0.616	2.866
5	0.301	5.156	3.157	44.51	30.05	-0.965	4.489

Table 4.2 Lattice constants,strain and unit cell volume calculated values for films with various nominal concentrations of Eu grown on sapphire.

Eu (at.%)	FWHM (deg.)	Lattice constants (Å)		Unit cell volume (Å^3)	Crystallites size (nm)	Strain (%)	Stress (GPa)
		c	*a*				
0.025	0.200	5.213	3.193	46.02	50.36	0.147	-0.682
0.05	0.211	5.211	3.191	45.97	46.71	0.11	-0.512
0.1	0.207	5.212	3.192	45.99	47.97	0.127	-0.591
0.5	0.264	5.197	3.182	45.58	35.06	-0.172	0.798
1	0.249	5.201	3.185	45.69	37.66	-0.093	0.431
2	0.311	5.184	3.174	45.23	28.93	-0.425	1.976
5	0.437	5.179	3.172	45.12	19.90	-0.512	2.382

Figures 4.10 and 4.11 illustrate the evolution of the residual strain in Eu-doped ZnO films deposited on a pure ZnO buffer layer and a bare sapphire substrate, respectively. It is worth mentioning that pure ZnO films produced by PLD typically suffer from a relatively high residual compressive stress up to (-0.5 GPa).[93] However, this typically found compressive stress became tensile and its magnitude increased as more Eu ions are added.

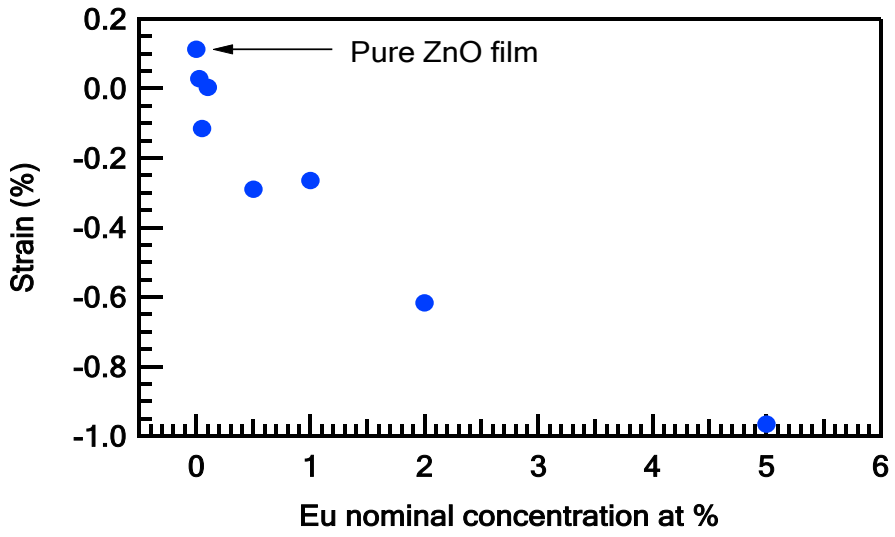

Figure 4.10 The strain trend in ZnO samples deposited on a pure ZnO buffer layer as a function of Eu concentration.

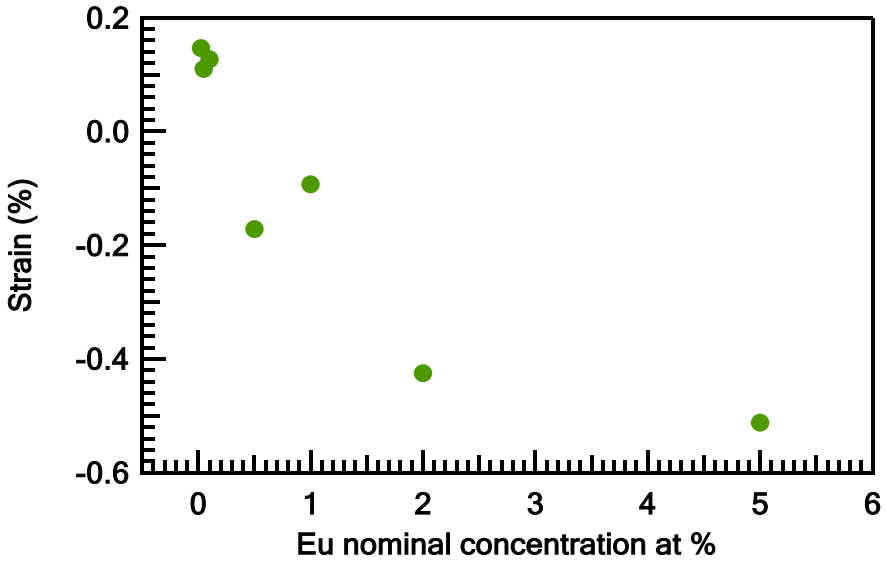

Figure 4.11 The strain trend in ZnO samples deposited on a bare sapphire substrate as a function of Eu concentration.

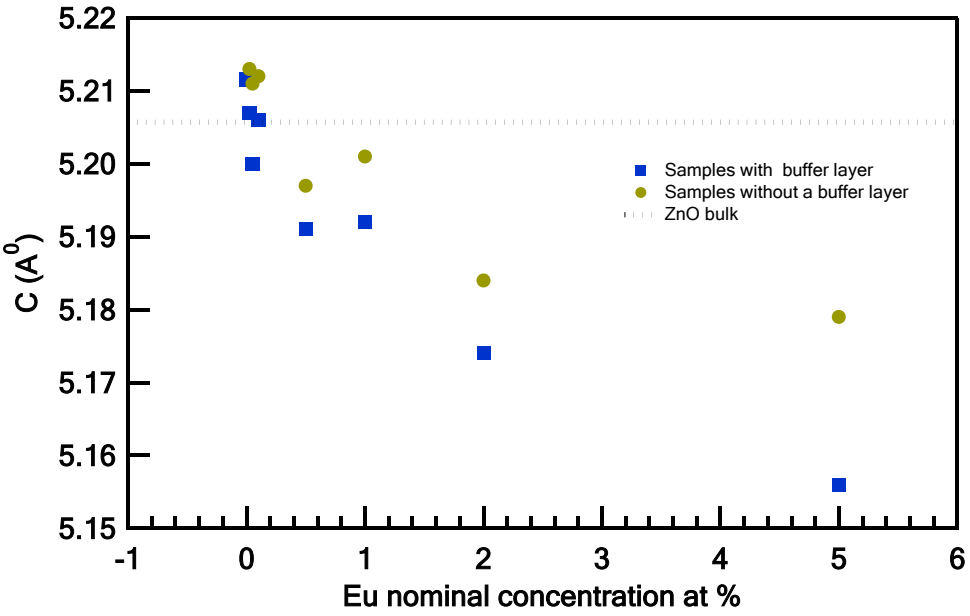

Figure 4.12 The *c*-axis lattice constant of ZnO films doped with Eu atoms and of strain-free ZnO bulk.

Surprisingly, as can be clearly seen in Figure 4.12, the *c* values become smaller as more Eu atoms are added. This finding is in contrast to the expected increase since the ionic radius of Eu^{3+} is bigger than that of Zn^{2+},

as indicated previously in Chapter One. A similar decrease in the *c* parameter was reported by Pérez-Casero et al.[94] when they doped a number of ZnO thin films produced by PLD with erbium atoms. The reduction in *c* values could be tentatively explained as follows: when Eu^{3+} ions substitute for Zn^{2+} ions, cationic vacancies are created in order to maintain the electrical neutrality of the ZnO crystal. This could be represented by the following equation: $3\ Zn^{2+} \rightarrow 2\ Eu^{3+} + V_{Zn}{}^{2+}$. These vacancies would cause shrinkage in the crystal network and subsequently lead to a reduction in the unit cell constant, as can be clearly observed in Tables 4.1 and 4.2. Obviously, the number of vacancies would grow as more Eu ions are inserted into the films. The gradual change in (002) XRD peak position and the interesting variation in the lattice constant (*c*) as the concentration of Eu ions changes provide further evidence for the successful incorporation of Eu^{3+} ions inside the ZnO matrix.

4.2Surface analysis

The morphology and the roughness of the surface of the ZnO films were investigated. SEM images of selected Eu-doped films from both series are shown in Figure 4.13. Images in the first row are for those samples with a pure ZnO buffer layer, whereas samples in the second row were grown on a bare substrate. These images reveal that films with low Eu concentrations exhibit slight porosity and are covered with irregularly shaped grains (crystallites) showing well-defined boundaries. Conversely, samples with the highest nominal concentrations of Eu show no clearly defined crystallites, which is in agreement with XRD results where crystallinity tends to degrade with increasing Eu content. Interestingly, the films containing < 0.5 at.% of Eu atoms and deposited on a ZnO buffer layer show a granular texture whereas samples grown directly on a bare sapphire substrate exhibit a columnar texture.

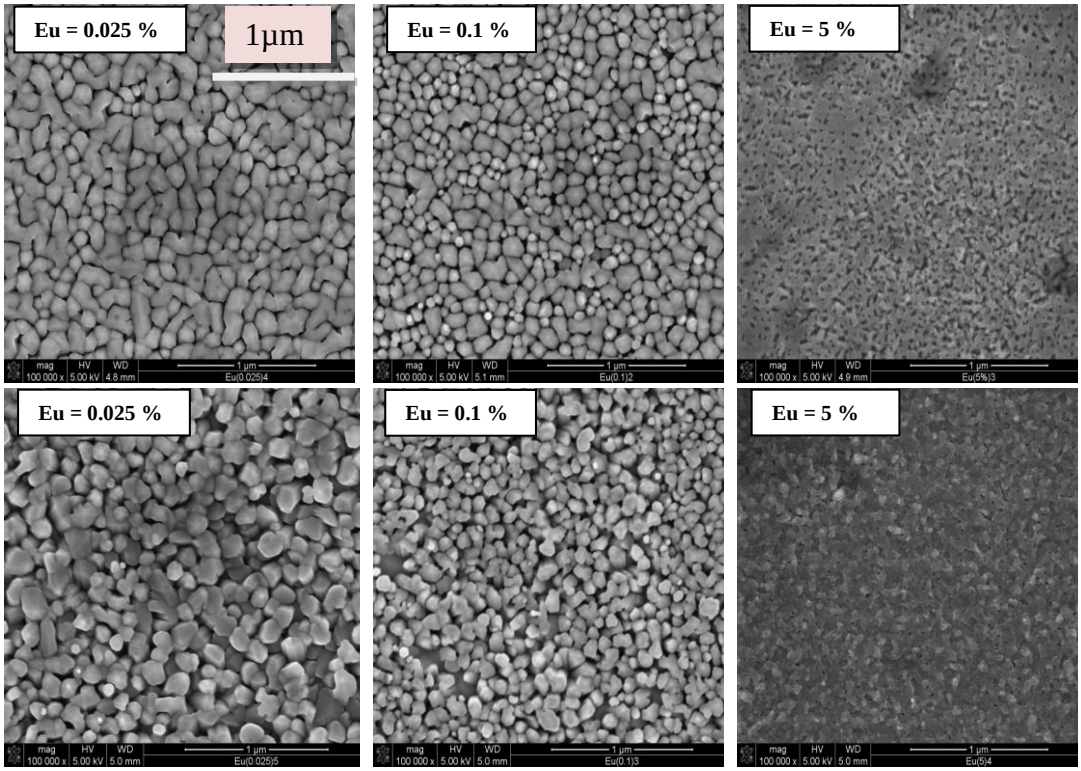

Figure 4.13 SEM images of some ZnO:Eu films from both series of samples containing the same amount of Eu nominal concentrations. The top row has the buffer layer.

The values of the root mean square (RMS) surface roughness of Eu-doped ZnO films are reported in Table 4.3.

Table 4.3 RMS surface roughness values of all films from both series of samples.

Nominal Eu concentration (at %)	RMS roughness (nm) (with buffer layer)	RMS roughness (nm) (without buffer layer)
0.025	4.0	13.5
0.05	7.0	8.50
0.1	5.8	8.00
0.5	4.5	16.0
1	7.0	10.5
2	6.4	3.30
5	5.0	5.40

Although it seems that there is no clear influence of the dopant (Eu) concentration on the surface roughness, samples with a ZnO buffer layer tend to be smoother than the films grown on a bare substrate.

4.3XPS Measurements

The surface elemental composition, stoichiometry and bonding state of Zn, O and Eu atoms were investigated by XPS measurements for both sets of ZnO:Eu thin films. The first set of samples containing different concentrations of Eu atoms were deposited on bare *c*-axis cut-sapphire substrates, while the other set were grown on a pure ZnO buffer layer deposited on the sapphire wafer at low temperature.

Survey XPS scans were performed to identify the surface constituents and their relative abundance. A typical survey scan (or alternatively called a wide-range scan) of ZnO doped with Eu ions is displayed in Figure 4.14. It was recorded with a large energy step, typically 160 eV. Various photoelectron peaks are identified and labelled as shown in the spectrum.

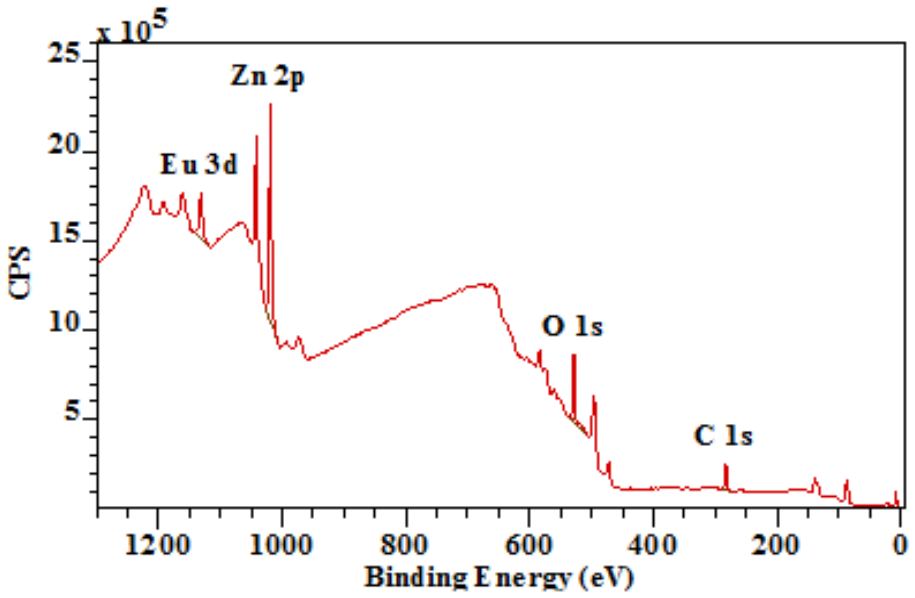

Figure 4.14 A typical XPS survey spectrum of ZnO:Eu thin film.

Figure 4.15 reveals the concentrations of dopants (Eu) at the surface of different films from both series of samples in comparison to the nominal concentrations of Eu in the corresponding PLD targets. The integrated area under the Eu 3d peak was used to estimate the europium concentration.

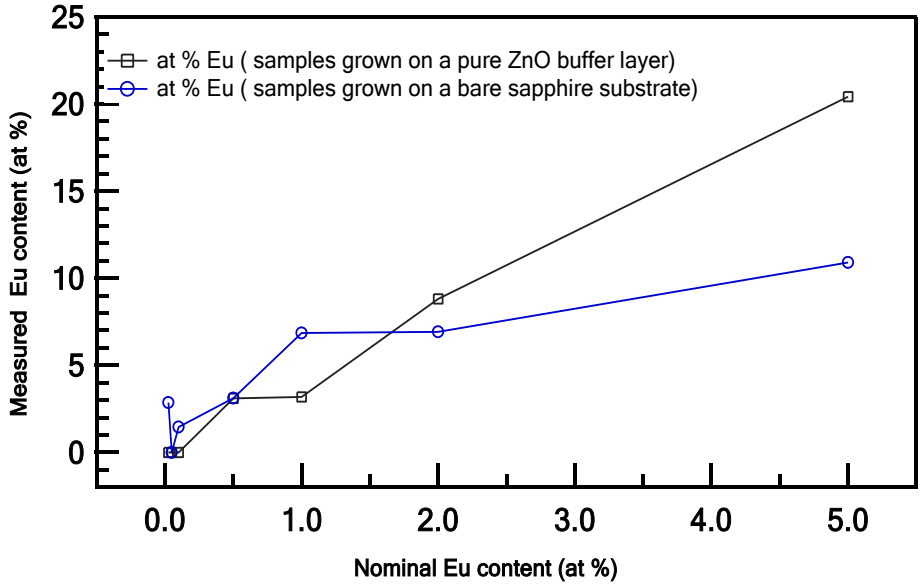

Figure 4.15 Concentration of Eu atoms on the surface of both series of films.

Although this measurement gives us the concentration of Eu atoms which reside in the sampled area covered by the X-ray beam (~ 500 microns) and up to a depth of 10 nm within the top layers of the film (as previously explained in Section 3.2), it shows that the measured Eu content is greater than the nominal concentrations in the PLD targets. This can be reasonably accounted for by considering that the large lattice energy difference between bulk ZnO (4142 kJ/mol) and Eu_2O_3 (12945 kJ/mol)[95] would tend to make the Eu atoms segregate and the high diffusivity feature of Eu atoms would cause them to migrate towards the surface region.[96, 97]

These two phenomena may have taken place during the sintering process of the PLD targets. It has been reported that in-depth profile Rutherford backscattering spectrometry **(**RBS) measurements on sintered RE-doped

ZnO PLD targets show a non-uniform in-depth distribution of RE species.[97] To a large extent such a heterogeneity issue can be avoided by systematically and carefully performing a pre-ablation step before the actual film growth takes place.[94]

Stoichiometry of the surface of the samples was calculated from the survey XPS spectra by integrating the areas under the O 1s and Zn 2p core peaks and taking their corresponding relative sensitivity factors from the Kratos library as saved in CasaXPS processing software. Ideally, stoichiometric samples should have a 1:1 atomic ratio between Zn and O atoms. Figures 4.16 and 4.17 depict the atomic ratios of different films from both series of samples. Interestingly, ZnO:Eu thin films deposited directly on the sapphire substrates are non-stoichiometric and generally O-rich. When a pure ZnO buffer layer is introduced on top of the substrate, the deposited films seem to be stoichiometric.

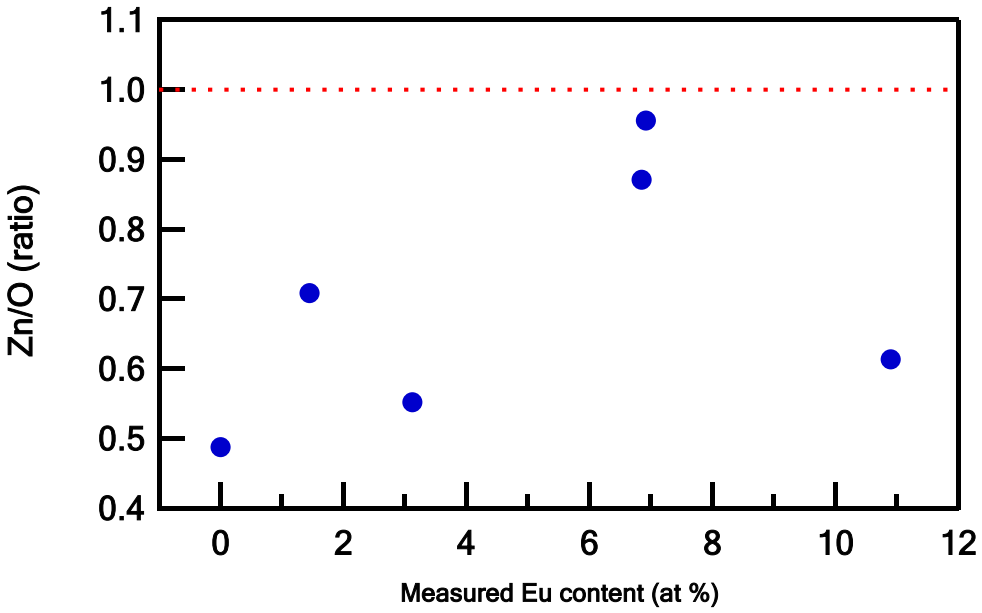

Figure 4.16 The stoichiometry of ZnO:Eu thin films deposited on bare sapphire.

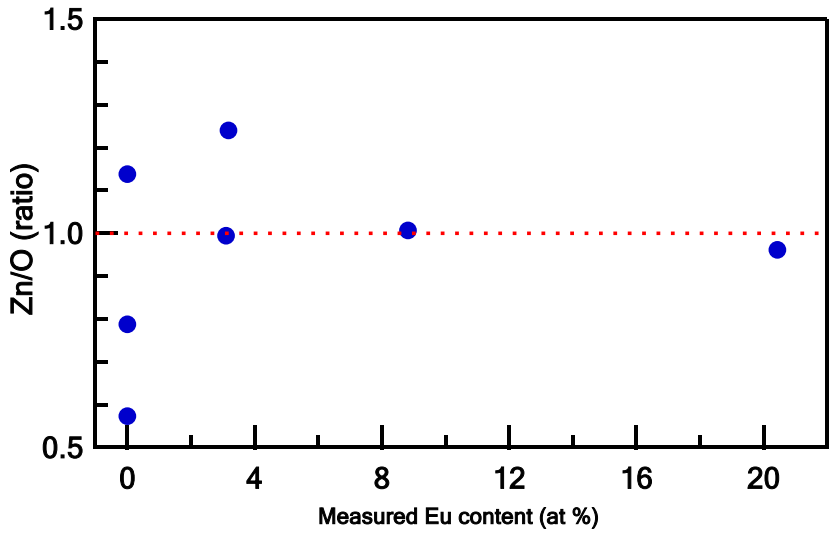

Figure 4.17 The stoichiometry of ZnO:Eu thin films deposited on a pure ZnO buffer layer.

Position shifts in XPS peak and close inspection of its shapes indicate the oxidation state of the related atom and the chemical environment around it. Therefore, high-resolution XPS scans were performed for the Zn 2p, O 1s and Eu 3d peaks. Figure 4.18 illustrates the XPS spectrum of the Zn 2p doublet peaks of different samples containing various concentrations of Eu dopants.

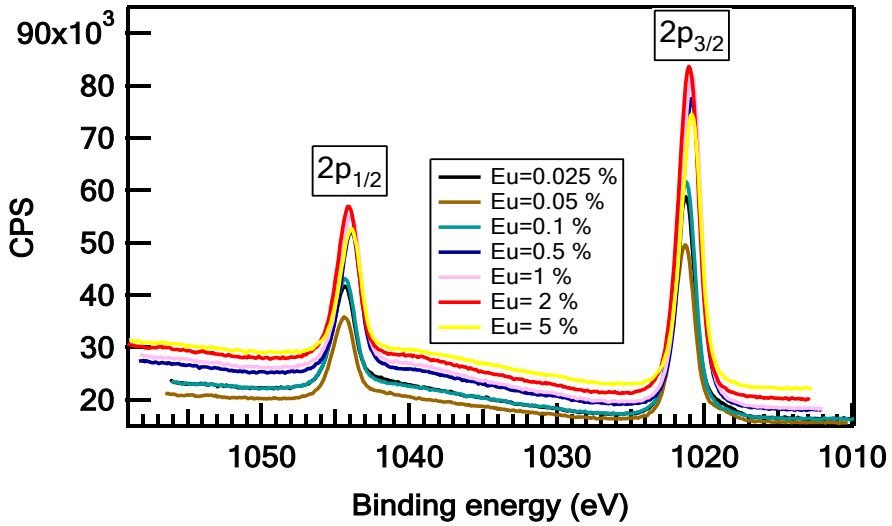

Figure 4.18 Zn 2p level XPS spectrum of Eu-doped ZnO films.

The Zn 2p peak appears as a doublet due to the interaction of the spin and orbital magnetic moments, the so-called spin-orbit effect, yielding a spin-orbit coupling of 23.1 eV. This is a characteristic value of the Zn(II) oxidation state present in an oxide environment and is in good agreement with literature data (23.06 eV) for ZnO.[98]

It should be pointed out that the binding energy of the Zn 2p doublet peak randomly shifts among the samples as shown in Figure 4.19. The binding energy of the Zn $2p_{3/2}$ peak is not consistent for all the samples. For example, it changes from 1020.9 eV to 1021.3 eV as the nominal concentration of Eu varies from 5 % to 0.025 %. Such a subtle shift in the binding energy presumably does not indicate a change in the oxidation state of Zn (as from Zn^0 (metal) to Zn^{2+}) since zinc is known not to be overly sensitive to a variation in the oxidation state.[99] Thus such a shift is possibly due to an inhomogeneous electrostatic charging effect of the sample surface. More explanation will be in the next paragraph.

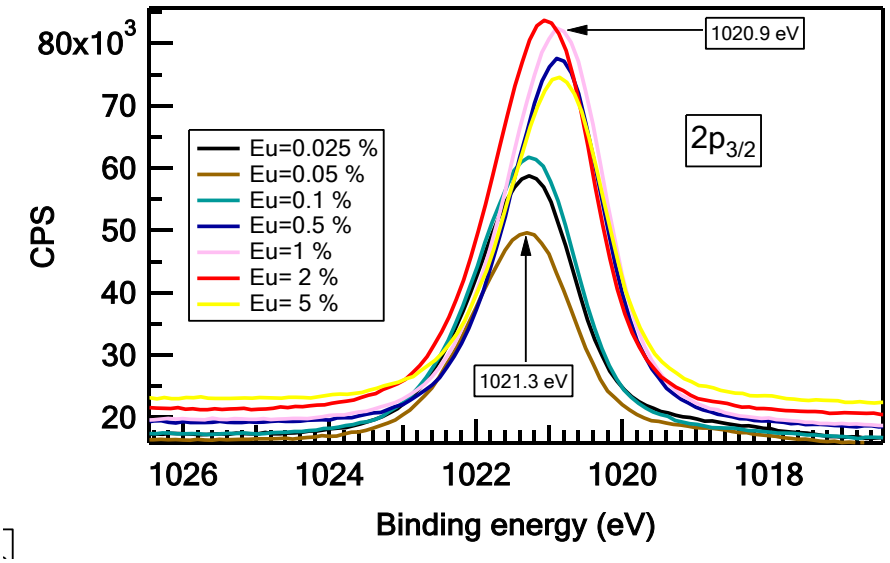

Figure 4.19 Variation in binding energy value of Zn 2p XPS peak of different Eu-doped ZnO samples containing different amounts of europium.

Eu_2O_3 is known to be an electrical insulator, which means more positive electrostatic charges will accumulate at the surface of the film due to the charging effect explained in Section 3.2. Moreover, if Eu ions are not uniformly distributed throughout the ZnO host, the induced positive charges will inhomogeneously accumulate on the surface of the film, which in turn will make it difficult to precisely use the charge neutralizer system to correct for the built-up charges. Thus, such an energy shift appears in the XPS spectra.

The high-resolution XPS spectra of O 1s core-level peaks obtained from pure ZnO, Eu-doped and Eu_2O_3 samples are shown in Figure 4.20. It can be clearly seen that the O 1s peak of Eu-doped films is asymmetric consisting of two components; a principal peak located at a low binding energy of 530.06 eV and a shoulder located at 531.4 eV. They are attributed to oxygen ions in the ZnO lattice and to O^{2-} in a chemical environment similar to Eu_2O_3, respectively.[95, 100-102] Furthermore, when their energy locations were compared with those obtained from a pure ZnO thin film and Eu_2O_3 a good match is obtained.

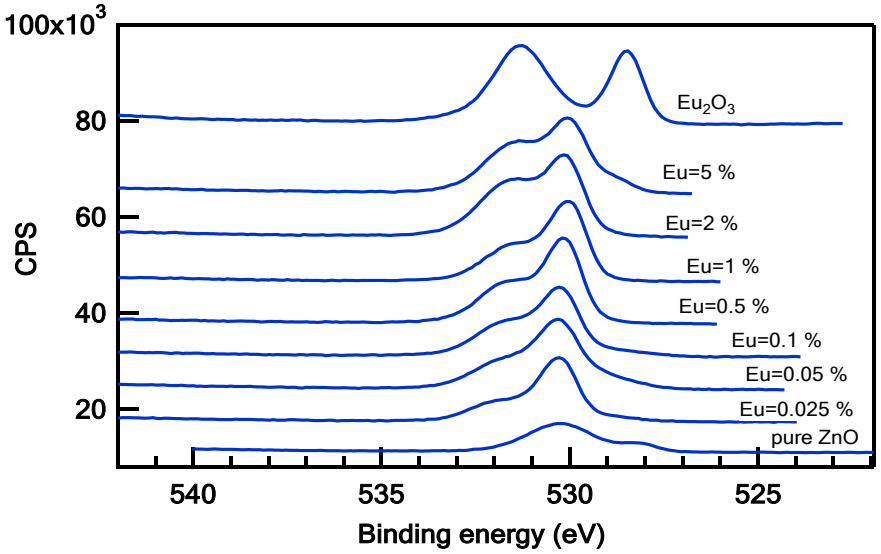

Figure 4.20 High-resolution XPS spectra of O 1s core level for Eu-doped ZnO, pure ZnO and Eu_2O_3 samples.

It should be pointed out that the binding energy of 531.4 eV, which has been ascribed to O^{2-} present in Eu_2O_3 matrix, also coincides with the binding energies of other species, such as loosely bound oxygen atoms and (Zn-OH) hydroxyl groups.[70, 103, 104] Thus, the possibility that these species contributed to this XPS peak cannot be completely ignored.

The valance state of europium present on the surface of the films was investigated. A high-resolution XPS scan of the Eu 3d region for both Eu-doped ZnO thin films and pure Eu_2O_3 are given in Figure 4.21 and Figure 4.22, respectively. It has been reported that the photoelectron spectrum of divalent Eu (as in Eu metal or in $EuAl_2$) considerably differs from the spectrum of Eu in the trivalent state such as in Eu_2O_3.[105] By inspecting the Eu 3d XPS spectrum obtained from the thin film, the binding energies of both doublet peaks of the 3d level ($3d_{5/2}$ and $3d_{3/2}$) were found to be 1133.7 eV and 1163.2 eV, which are very close to those obtained from Eu_2O_3 and in good agreement with values published in the literature.[95, 100, 101, 106] This result confirms that Eu ions in the film presents in a chemical environment similar to Eu_2O_3 where the Eu ion is surrounded by seven O ions and has a (3+) valance state.[107] It is expected that when Zn^{2+} ions in a ZnO crystal are replaced by a larger ions with different valance states such as europium the local environment would undergo some changes in symmetry and in the coordination number of oxygen around the Eu ion. Based on the extended X-ray absorption fine structure (EXAFS) measurements, it was concluded that the oxygen coordination number changed from four to seven when a ZnO crystal was doped with europium to form an EuO_7 complex.[11]

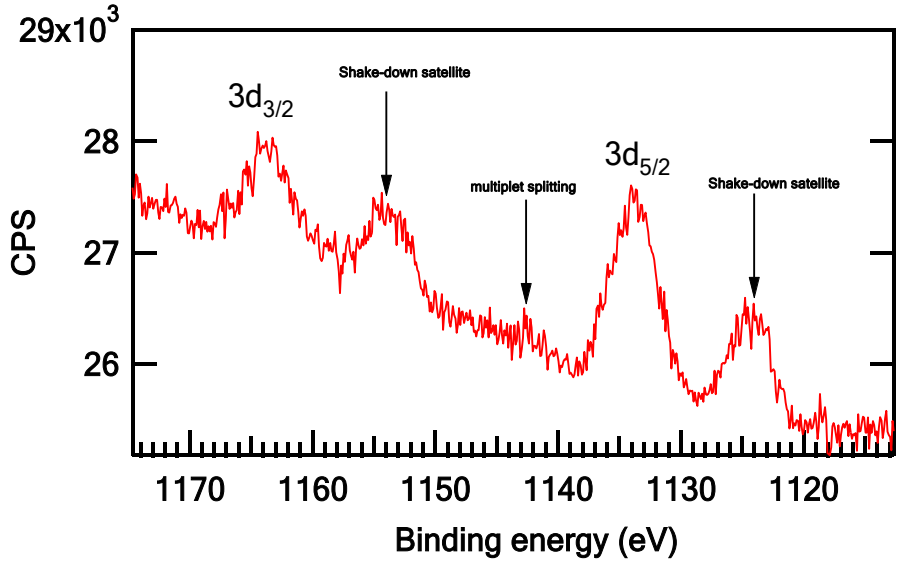

Figure 4.21 Eu 3d XPS region of Eu-doped ZnO sample.

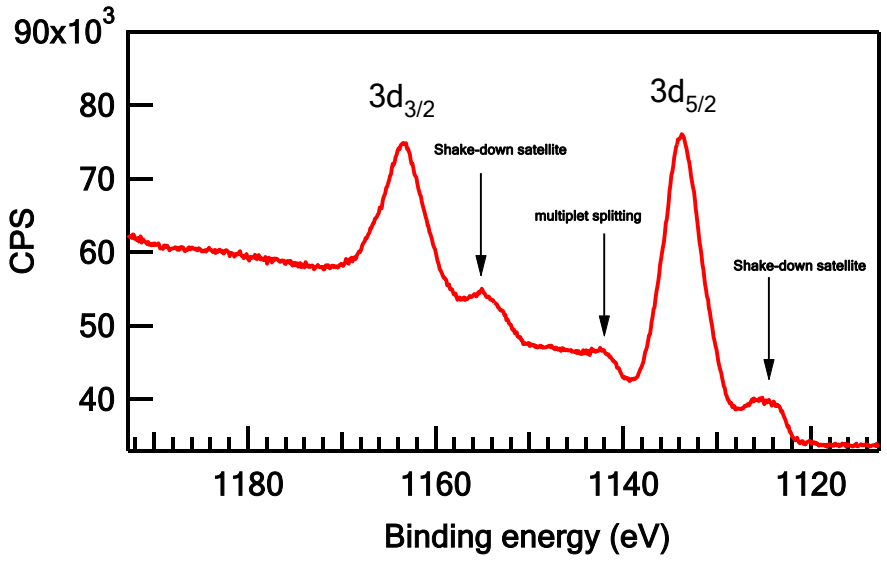

Figure 4.22 Eu 3d XPS region of Eu_2O_3 sample.

Besides the conventional doublet peaks additional spectral structures (the so-called satellites) are observed, namely, shake-down and multiplet splitting. These secondary features are commonly seen in the XPS spectrum of RE materials. The underlying physical mechanism of such secondary features has been attributed to final state effects and/or to charge transfer coexcitation, mainly from the 2p orbital of oxygen to the4f of RE.[95, 105, 106]

4.4Transmission Measurements

The optical transmittance spectra of ZnO films with various concentrations of Eu from both series of samples are shown in Figure 4.23 and Figure 4.24.

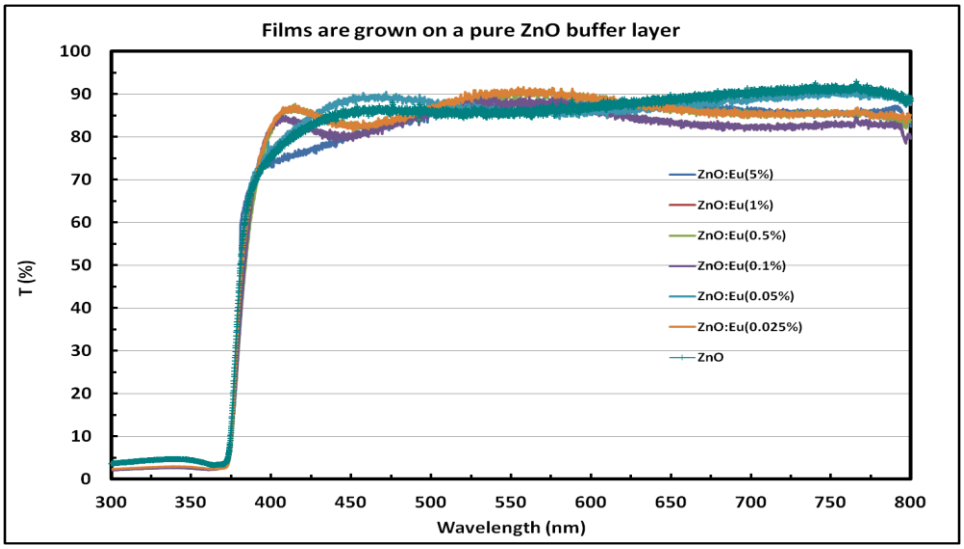

Figure 4.23 Transmittance spectra of ZnO films doped with Eu and grown on a pure ZnO buffer layer. The nominal Eu content is shown in brackets.

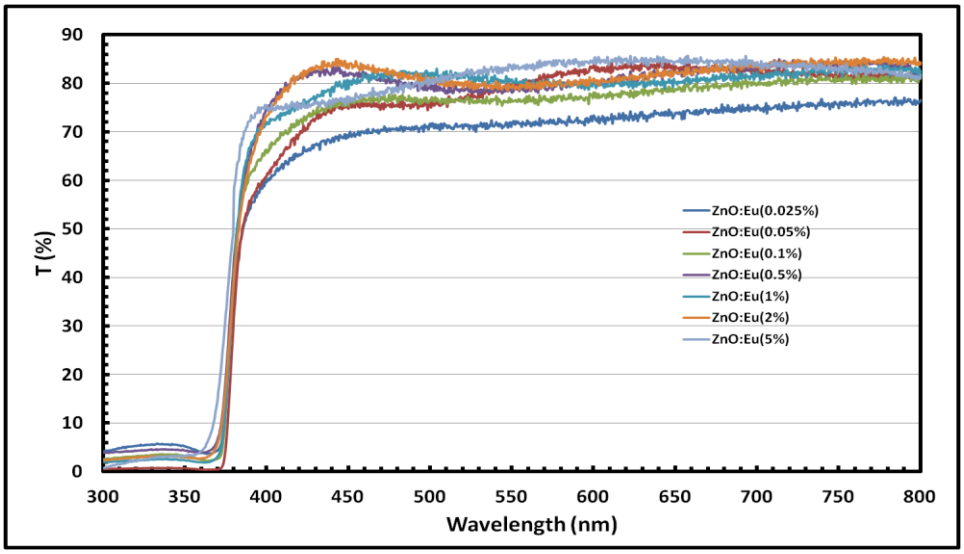

Figure 4.24 Transmittance spectra of ZnO films doped with Eu and grown on a bare sapphire substrate. The nominal Eu content is shown in brackets.

These spectra were not corrected for reflection. All films are highly transparent in the visible region, with a sharp absorption edge at 373 nm.

High transmittance of about 85% on average is obtained. The transmission property of a material is influenced by absorption and reflectivity of the surface of the material. Chemicals additives are usually used to modify some of the optical properties of materials. For example, the refractive index and transmission range of fused silica glass can be changed by adding specific impurties during the fusion process. However, Eu ions as impurities are assumed not to alter the optical transmission since their energy levels are localised which would only appear as discrete narrow absorption bands in the transmission spectrum.

The optical band gap energies of different Eu-doped films from both groups of samples were estimated from the transmittance data, as previously explained in Section 3.3, and are shown in Figure 4.25 and Figure 4.26.

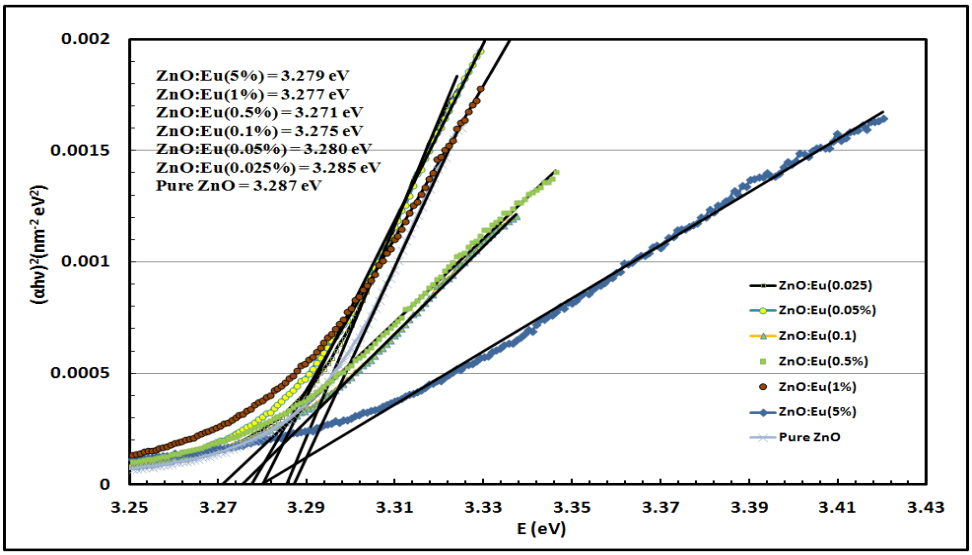

Figure 4.25 The band gap energy of ZnO:Eu thin films calculated from the spectral dependence of absorbance. These films were grown on a pure ZnO buffer layer.

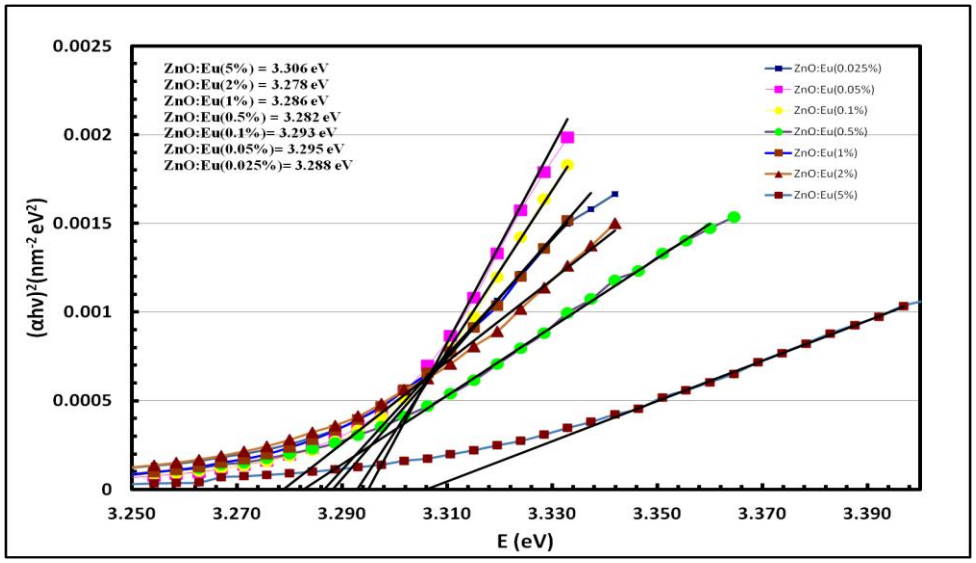

Figure 4.26 The band gap energy of ZnO:Eu films calculated from the spectral dependence of absorbance. These films deposited on a bare sapphire.

The band gap energy values of different films from both series of samples are presented in Figure 4.27 and Figure 4.28 as a function of the calculated stress. In general, it can be said that the gap energy decreases as the samples become more stressed. It should be noted that samples with a buffer layer have gap energy values closer to the band gap energy (3.4 eV at RT) of strain-free ZnO bulk.

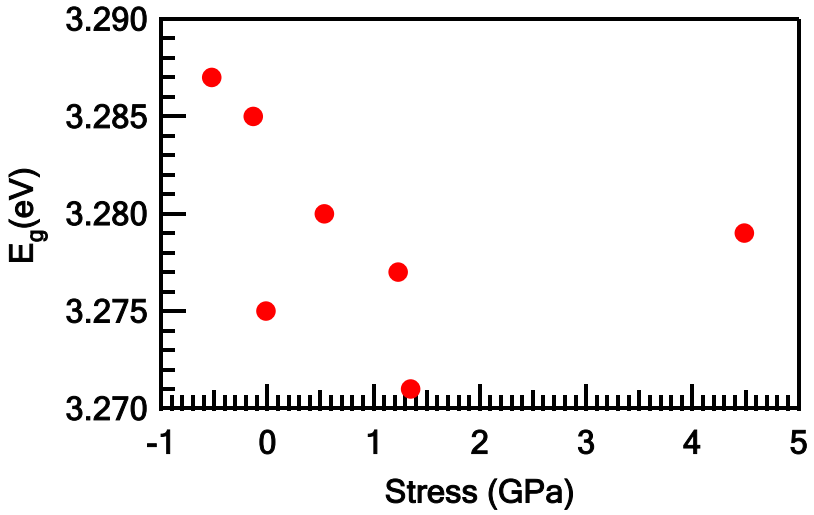

Figure 4.27 The band gap energy of ZnO:Eu films grown on a ZnO buffer layer.

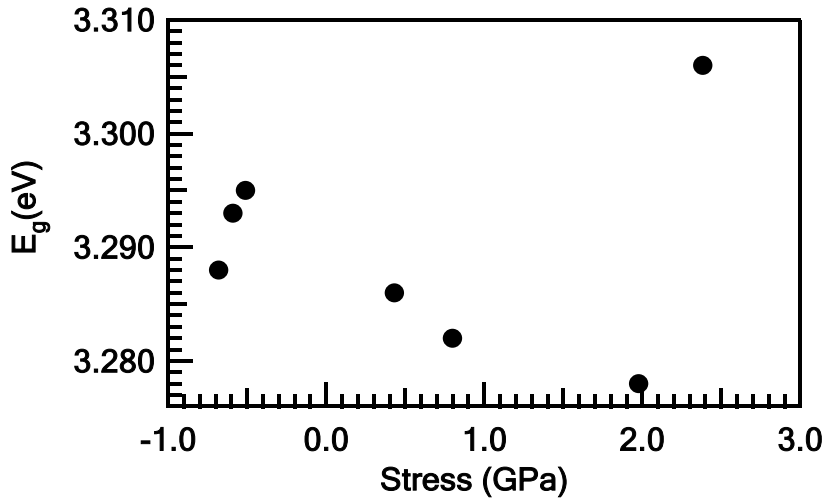

Figure 4.28 The band gap energy of ZnO:Eu films grown on bare sapphire.

4.5Optical Studies

Photoluminescence measurements of Eu-doped ZnO films were performed utilising two different excitation sources. Above-gap excitation with a He-Cd laser operating at 325 nm was used to study the near band edge luminescence of the host ZnO and to try to indirectly excite the europium ions. Also, in-gap excitation was provided using 488 and 457.9 nm lines of an Ar+ laser to resonantly excite europium ions where these wavelengths match some specific energy levels of 4f states of Eu^{3+}. Surprisingly, no ZnO-related emission was detected for those samples doped with Eu^{3+} ions at concentrations of 0.5 at. % or higher when the He-Cd laser was used. Such an observation has also been reported in the literature.[108, 109] This quenching in luminescence could be ascribed to the degradation in crystallinity already noted from XRD measurements and/or to some other defect states acting as energy traps (i.e., non-radiative centres). However, it seems certain that inserting relatively large ions such as europium into the matrix of ZnO would introduce extrinsic defect levels in the band gap which might create non-radiative (de-excitation) pathways leading to reduced or even completely quenched ZnO-related emissions.

Figure 4.29 depicts the near-band edge PL spectra taken at 5 K of a pure ZnO thin film and three doped films containing less than 0.5 % of Eu^{3+} ions. For the undoped sample, a strong characteristic ZnO PL emission peaking at 3.368 eV is observed with a full width at half maximum of ~ 6 meV. However, the doped films exhibit two peaks located at approximately 3.363 eV and 3.332 eV. These can be attributed respectively to donor bound excitons and to the recombination of excitons, which is commonly observed in semiconductor material, localised at a structural defect.[110]

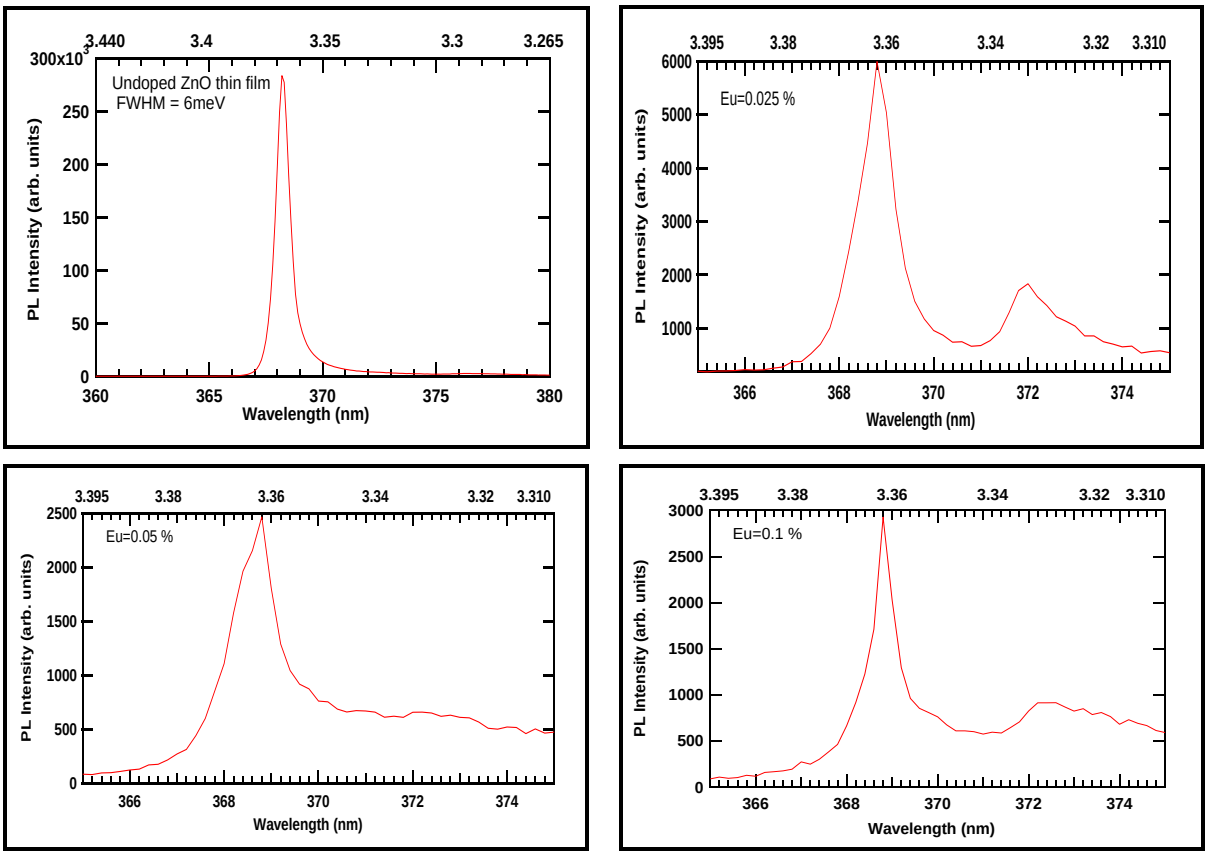

Figure 4.29 Low-temperature PL spectra of Pure ZnO and Eu-doped ZnO films excited with a 325 nm He-Cd laser.

Figure 4.30 displays the emission spectra of various samples in the visible region under UV excitation at 5 K carried out by an He-Cd laser. Two distinct optical features can be seen. Firstly, an asymmetric broad band stretching from 520 nm to over 750 nm is observed. Such an emission could be due to ZnO intrinsic defects and/or some other extrinsic defects due to

incorporation of Eu ions. This red broad band was also detected by Ebisawa K. et. al., who suggested where a deep defect to be responsible.[111] Other research has reported the observation of this broad band in the studied samples which were prepared by Pechini method.[14] It was assumed that this emission band is due to a transition from the ZnO conduction band or shallow levels to deep levels.

Secondly, as the concentration of Eu^{3+} ions increases other narrow emissions appear and are found to be superimposed on top of the broad band. These emissions were identified as the transitions from the $^5D_0$ state of Eu^{3+} to the various levels of the ^7F_J ground multiplets. Interestingly, the relative intensity of the broad band decreases with increasing europium content and the Eu-related emissions become dominant.

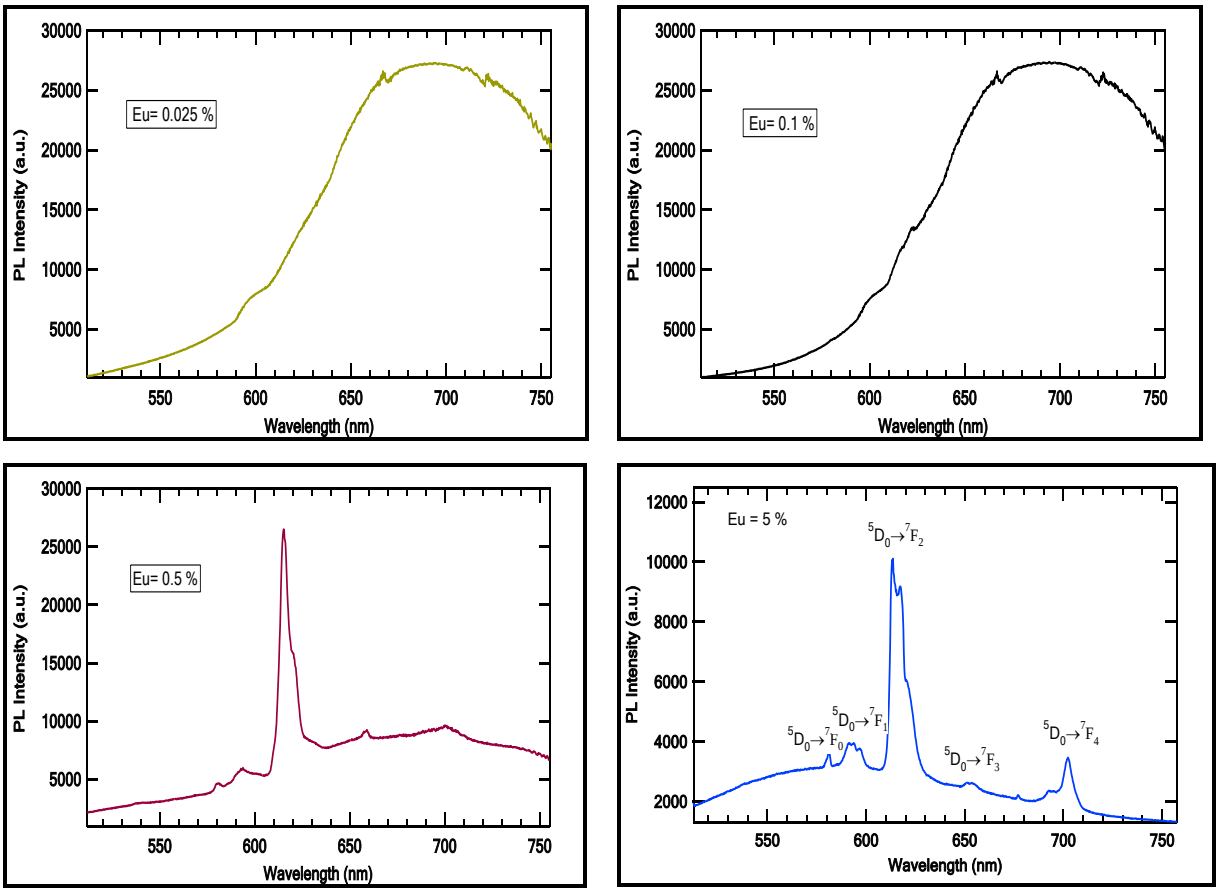

Figure 4.30 PL spectra of Eu-doped ZnO samples at 5 K excited with 325 nm.

This could tentatively explain the possible mechanism responsible for the efficient energy transfer process between ZnO and Eu^{3+} ions which could occur via these defect states. This process will be discussed later.

Figures 4.31 and 4.32 show two low-temperature PL spectra of the same ZnO:Eu thin film excited by two different Ar+ laser lines. Unexpectedly, no optical transitions of Eu ions were detected. This complete PL quenching may have been caused by defects acting as energy traps. However, an asymmetrically broadened band peaking at 590 nm as well as a strong sharp emssion located at 693.6 nm were detected.

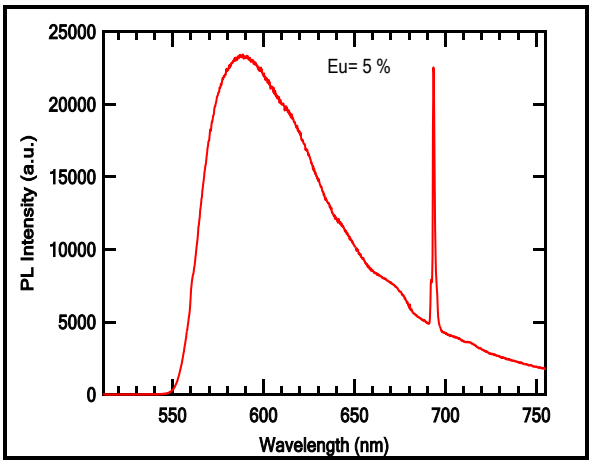

Figure 4.31 PL spectrum of Eu-doped ZnO excited with 488 nm.

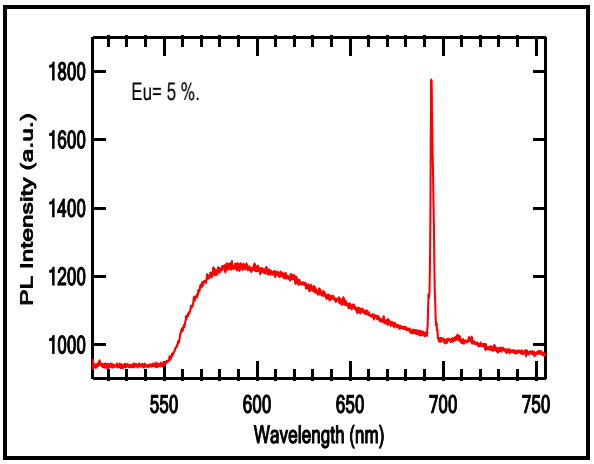

Figure 4.32 PL spectrum of Eu-doped ZnO excited with 457.9 nm.

Both shape and the location of the broad band are noticeably different to those obtained under the excitation of 325 nm. This could imply that the origins of the bands are different. However, the sharp line was confirmed to be unrelated to the europium ions as it was also seen in the PL spectrum of the ZnO:Er samples and in the PL of pure ZnO. This means it must be associated with the host material. Based on its energy location and its estimated lifetime it is assumed to be associated with iron impurities as has been observed in other researcher done on undoped ZnO bulk crystal found

to have some Fe impurities.[112] In this work some of the iron atoms are assumed to come from trace impurities which, according to the certificate of analysis produced by the supplier, were present in the Er_2O_3 and Eu_2O_3 powders.

The spectrum shown in Figure 4.33, taken at room temperature, consists of a sharp emission peaking at 1.7874 and two distinctive vibronic side bands. The sharp emission is attributed to the zero phonon line (ZPL) of the $^4T_1$ to $^6A_4$ transition of Fe^{3+}, while the vibronic bands, the so-called Stoke and anti-Stoke bands, are due to phonon scattering.

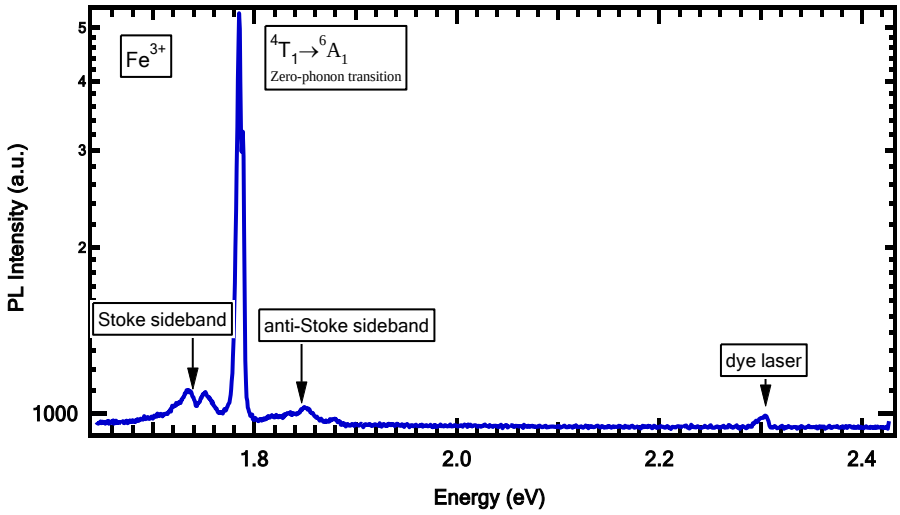

Figure 4.33 PL spectrum of the Fe^{3+} impurity in ZnO films excited with the dye laser at room temperature.

The lifetime measurement of the ZPL transition was performed using a chopper wheel for generating pulses of light. Hence, the lifetime can be reasonably estimated using the following equation

$$I(t) = I_o \exp(\frac{-t}{\tau}) \qquad (27)$$

where $I(t)$ is the intensity of the emission at any time, τ is the lifetime and I_o is the intensity at time zero. Since the ZPL, $^4T_1 \rightarrow {}^6A_1$, is theoretically not

allowed due to the spin selection rules, a long radiative lifetime is expected. The lifetime plot is displayed in Figure 4.34. The lifetime was found to be 27.7 ms, which agrees well with the reported value in the literature (25.2 ms).[112, 113]

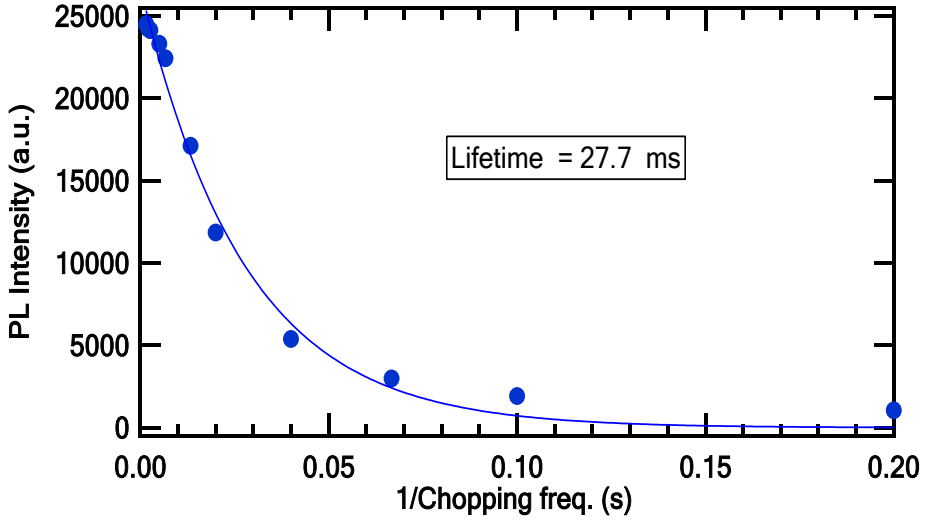

Figure 4.34 Intensity decay plot used to estimate the lifetime of the Fe^{3+} ZPL.

The temperature dependence plot of the ZPL PL is illustrated in Figure 4.35, where the ZPL shows a red shift of 3 meV when temperature increases from 3.5 to 295 K. It is also noted that the ZPL intensity declines as temperature increases while the intensity of the additional weak peak located on the high-energy side in the spectrum increases up to 150 K. Such an additional emission is assumed to be due an electronic transition from a higher sublevel of the excited state, caused by the crystal field of ZnO, to the ground state. When temperature increases, a higher sublevel of the excited state, $^4T_1$, is increasingly populated with electrons from the lowest sublevels of the excited state. Hence the intensity becomes high. However, when the temperature is raised above 150 K, the intensity starts to drop, indicating the presence of additional relaxation channels such as strong photon-phonon interactions. It is known that the 3d orbital of transition metal ions such as Fe^{3+} has a relatively large radius and are not screened by

the outer electronic shells. Thus the 3-d electrons are exposed to the crystal field and a strong ion-lattice coupling is expected.

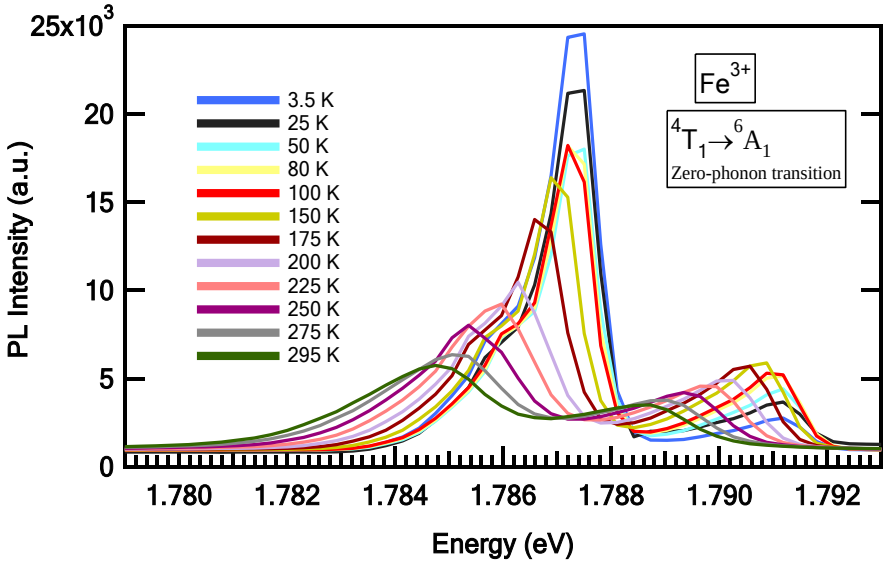

Figure 4.35 Temperature dependence of PL spectra of the ZPL transition.

The temperature dependence of the ZPL emission was mathematically modelled by a single-path Arrhenius equation as shown in Figure 4.36.

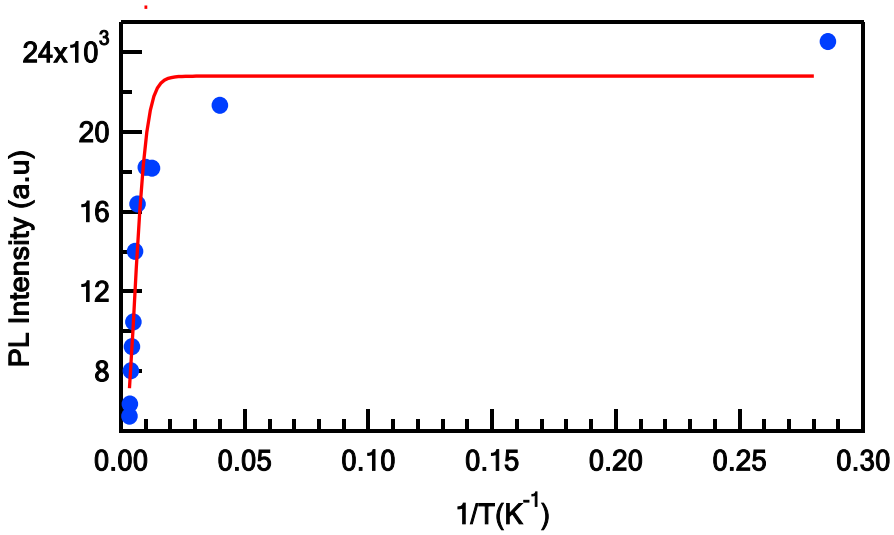

Figure 4.36 The PL intensity of the ZPL emission as a function of temperature. The data was fitted using Eq. (26) as shown by the solid line.

The Arrhenius equation is given by

$$I(T) = \frac{I(0)}{1 + Ae^{(\frac{-E_a}{k_b T})}} \tag{28}$$

where $I(T)$ & $I(0)$ are the integrated intensity of a radiative transition at temperature T and at absolute zero, respectively. A is a constant describing the efficiency of nonradiative process depleting the emission while E_a is the thermal activation energy of the depletion process. k_b is the Boltzmann constant. There are many reasons by which luminescence can be thermally quenched. For example, the intensity of the emission of an electronic transition between 4f states of rare earth ions can be depleted when temperature is increased since the vibrational levels of the ground and the excited states of the ions are populated so that these vibrational states can participate in PL emission leading to its quenching. In the case of semiconductor materials where excitonic emissions are dominant thermal ionisation is usually the main mechanism for the intensity depleting process.

By using applying Arrhenius equation the activation energy (E_a) the PL intensity of the ZPL emission from the single-path fit was estimated to be 33 meV, which is higher than the value reported in the literature (~ 9 meV)[113] and may be attributed to the presence of an additional non-radiative channel.

Combined Excitation-Emission Spectroscopy (CEES) measurements were carried out to investigate the optical centres of Eu^{3+}. Two distinctive optical centres were detected and are referred to as A and B. A contour plot of these centres is shown in Figure 4.37. Centre A is thought to be associated with Eu^{3+} ions, which enter substitutionally for Zn^{2+} in a crystalline

environment and hence exhibit narrow PL and PLE peaks as shown in Figure 4.38 and Figure 4.39, respectively.

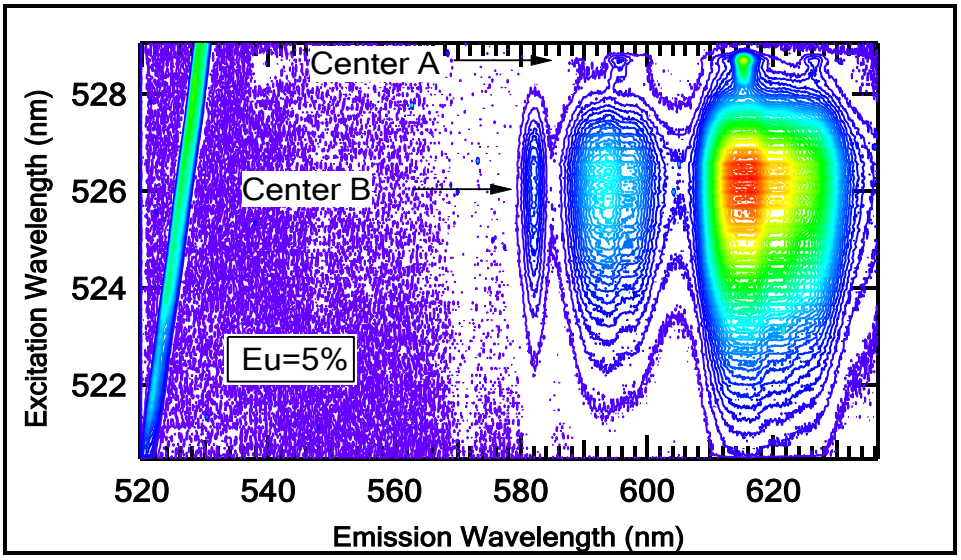

Figure 4.37 A contour plot of CEES of Eu^{3+} optical centres.

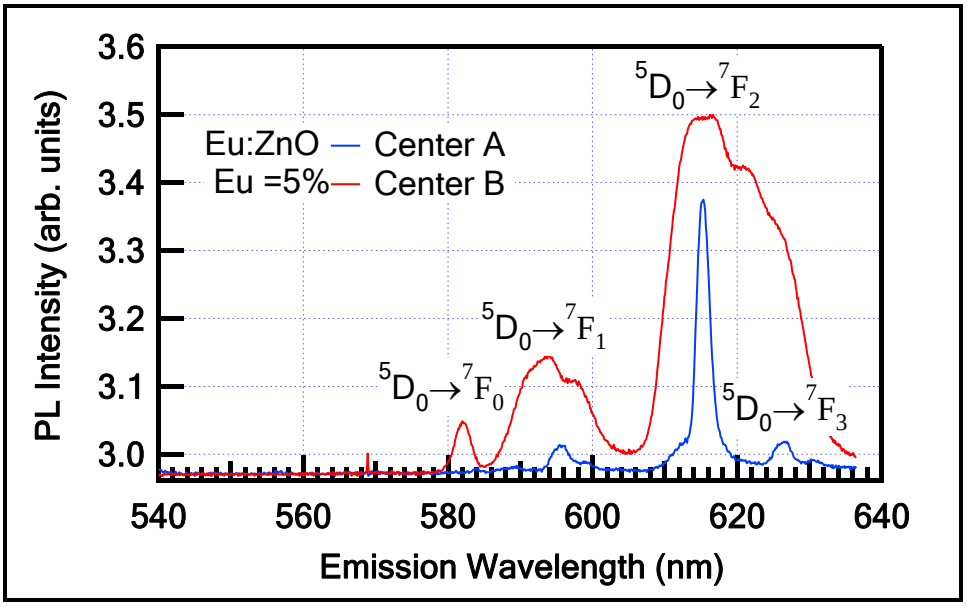

Figure 4.38 PL spectra of the Eu^{3+} related optical centres.

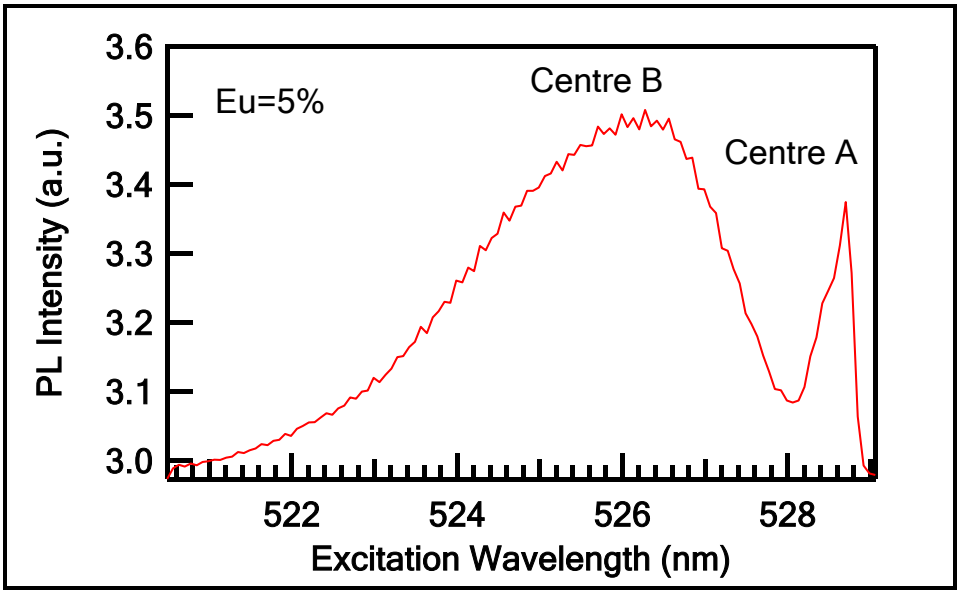

Figure 4.39 The excitation spectrum of the $^5D_1$ multiplet from the Eu^{3+} in a ZnO:Eu film monitored at 615.55 nm.

In contrast, centre B shows broad PL and PLE signatures, which speculatively attributed to Eu^{3+} ions located in a variety of distorted lattice sites of very similar symmetries and local fields, as in a glass-like material. In such an environment each Eu^{3+} ion would experience slightly modified crystal-field interactions, leading to the existence of a broad emission.

Surprisingly, the absorption band of centre B exhibits a gradual shift towards the lower energy side with increasing nominal concentrations of europium as shown in Figure 4.40. It has been reported that the absorption transition of Eu^{3+} doped into ZnO-SiO_2 binary glass systems changes when the concentration of ZnO increases. Such an observation was assumed to be due to Eu-O-Zn bond formation.[114]

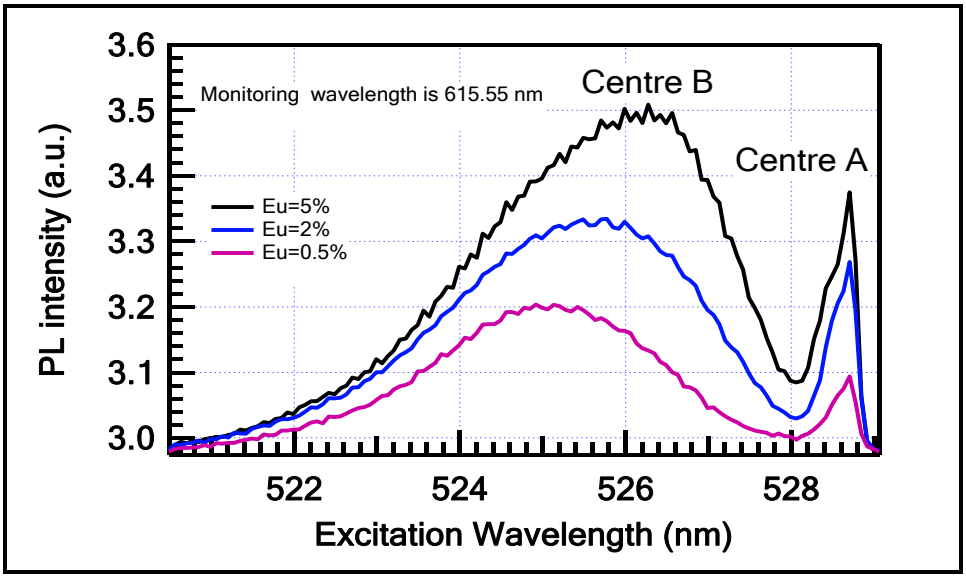

Figure 4.40 Excitation spectra of ZnO:Eu samples containing different Eu concentarions.

According to the group theory, the spectral fine structure of a dopant embedded in a crystalline host material is largely affected by its lattice location and, hence, the local environment (i.e., the nearest neighbouring, so-called ligand, ions) in ways that rely on the symmetry (structural arrangement) of these ions.

For example, energy levels can split and shift with changes in the actual environmental symmetry. Moreover, forbidden electronic transitions may be allowed. A free-ion state with a total angular momentum (J) has (2J+1) fold degeneracy, which can be partly or totally lifted depending on the dopant's local crystal symmetry. However, the maximum number of split levels is 2J+1 for integer J or J+1/2 for half-integer J, according to the so-called Kramers theorem.

ZnO possesses a hexagonal crystal structure and has a trigonal (C_{3v}) site symmetry. When Eu^{3+} ions are incorporated into a ZnO matrix and substituted for Zn^{2+}, its standard unit cell will undergo some structural departure and experience some degree of strain, causing a distortion effect

to the local C_{3v} symmetry or perhaps destroying it. The observation of the $^5D_0 \rightarrow {}^7F_0$ transition in the centre B spectrum supports this assumption because such a transition is, in principle, forbidden due to both spin and parity selection rules and cannot occur if Eu^{3+} ions reside in a site with a perfect C_{3v} symmetry. Furthermore, the observation of more Eu-related transitions from centre B in comparison with site A indicates that centre B is associated with a site of a lower symmetry, i.e., no inversion symmetry.

The effect of thermal annealing on the optical centres was investigated by Alex Neiman, a student at the Department of Physics and Astronomy, University of Canterbury, to fulfil the requirements of the PHYS391 course. Figure 5.41 illustrates a contour plot of an annealed ZnO:Eu sample heated to 700 K (i.e., 426.85 ^oC). Although such a temperature is considerably less than the growth temperature (750 ^oC), it has a pronounced effect where centre B, which is anticipated to be in a glass-like environment, is split into new additional optical centres. Such splitting is attributed to an improvement in crystal structure with low symmetry.

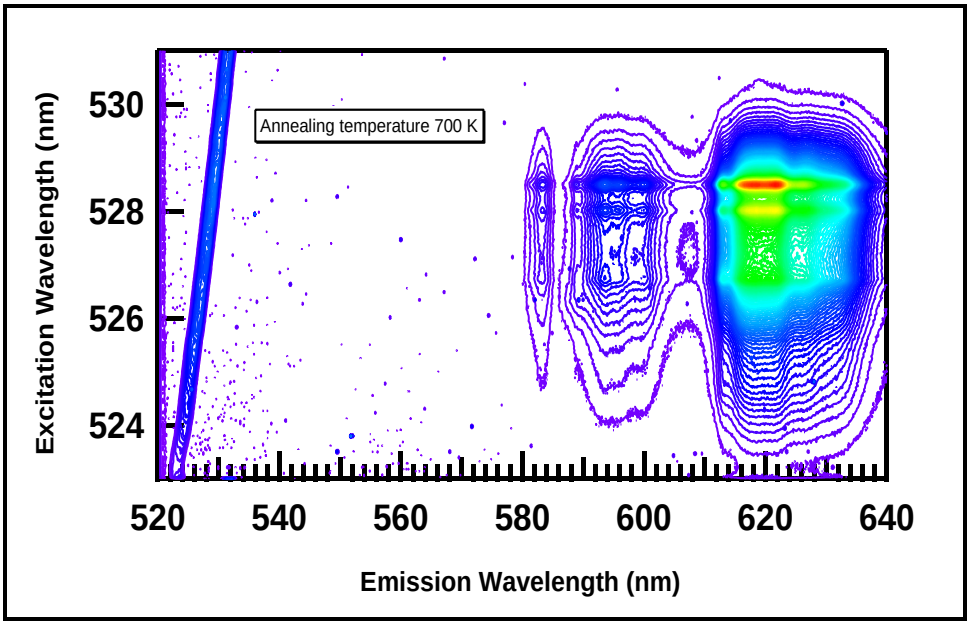

Figure 4.41 A contour plot illustrating the annealing effect on the optical centres of a ZnO:Eu^{3+} thin film.

To account for the observed optical emissions of Eu^{3+} ions when indirectly excited with UV radiation, and to give an explanation for the complete quenching of the near-band edge luminescence of the ZnO sample doped with high concentrations of Eu atoms ($\geq$ 0.5 at. %), a plausible energy transfer mechanism based on an intermediate (defect) state in the band gap of ZnO is proposed. Figure 4.42 shows a simplified schematic representation where the energy levels of Eu^{3+} ions and the defect state are displayed with respect to the band gap of ZnO. There are two possible sources of defect-related states. They could be created during the incorporation of Eu^{3+} ions and/or could be related to intrinsic defects in the host material. Such induced states could possibly act as energy trap centres and intermediate channels to assist the energy transfer process.[109, 115, 116]

When the ZnO host material is excited with UV light, valence electrons will be excited to the conduction band and holes will be left in the valence band. Some of these excited electrons will recombine with the holes in the valence band producing the commonly seen near-band edge emissions. However, if a defect state exists in the band gap of ZnO, it may capture some of these excited electrons, leading to a defect-related emission.

For the ZnO:Eu samples with low concentration of europium (< 0.5 at.%) the ZnO near-band edge emission and a defect-related broad emission are clearly seen in Figure 4.29 and Figure 4.30, respectively. However, as the concentration of europium increases, the number of trap centres is expected to increase, causing complete quenching of ZnO-related emission. At the same time because there are more Eu^{3+} ions, an efficient energy transfer process between the intermediate state and the $^5D_0$ multiplet of Eu^{3+} is expected, leading to the observation of $^5D_0 \rightarrow {}^7F_J$ emissions of Eu^{3+} where J = 0,1,2,3 and 4.

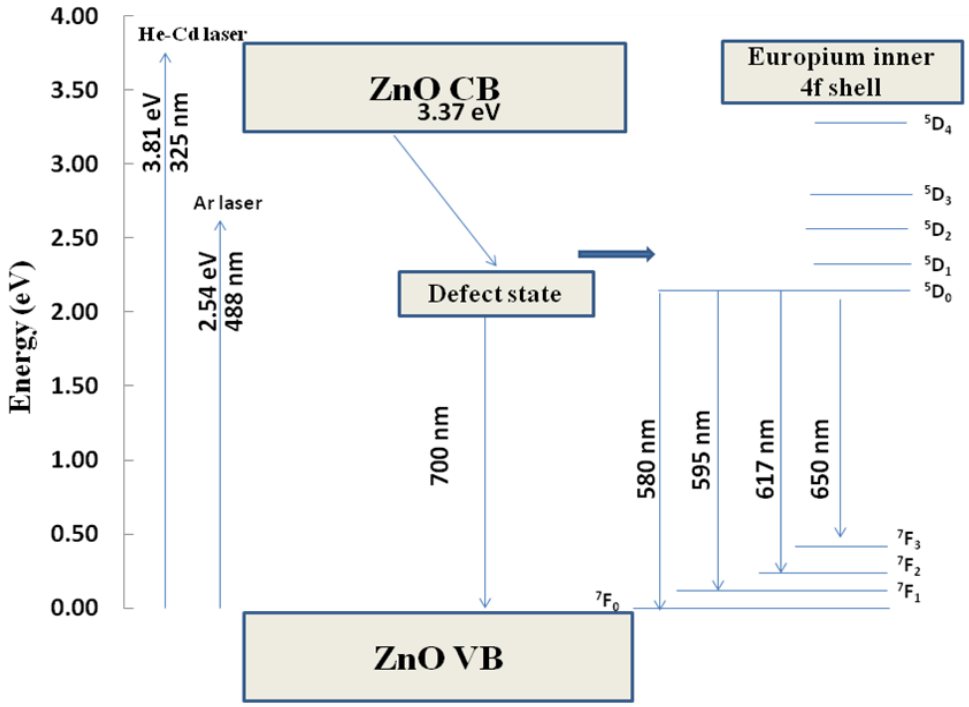

Figure 4.42 A simplified schematic drawing illustrating a possible energy transfer mechanism between ZnO and Eu ions.

Chapter 5

Results for ZnO: Er^{3+} Samples

5.1Structural Characterisation

The crystal structure of the Er-doped ZnO thin films were studied by X-ray diffraction. Figure 5.1 depicts the XRD pattern of a number of ZnO films doped with different quantities of Erbium. All films exhibit a single-crystal hexagonal structure and show high orientation along the *c*-axis. The nominal concentration of Er in each film is shown above the XRD spectrum of each film.

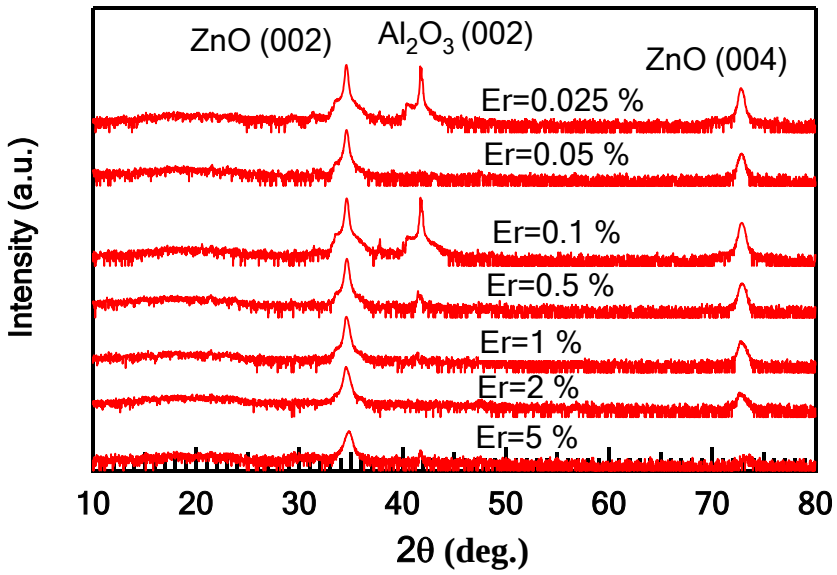

Figure 5.1 XRD patterns of different samples of ZnO:Er. The Y-axis has been vertically offset for clarity.

Significantly, no Er_2O_3-related XRD diffraction peaks were observed in the spectra, indicating that Er atoms were successfully doped into the ZnO matrix. Furthermore, as was observed in the ZnO:Eu samples the intensity of the (002) ZnO diffractive peaks of the samples generally decreases with increasing concentrations of Er ions. Replacing zinc ions with relatively

large ions such as erbium would surely cause structural distortion; hence some deterioration in crystallinity is expected. As more erbium ions are incorporated the extent of deterioration is more likely to rise. It should be pointed out that the sapphire-related XRD peak is missing in some some the diffraction spectra which could de due to misalignment of the sample holder causing the sample not to be properly placed in the focusing area of the x-ray beam. Hence the intensity count of the diffractive peaks decreases.

To quantitatively assess the structural quality of the samples, the full width at half maximum (FWHM) of the (002) ZnO diffractive peak for all samples was studied as a function of the nominal concentration of the Er ions. Figure 5.2 and Figure 5.3 show the FWHM and the intensity of the (002) ZnO diffractive peaks for two sets of samples. Both samples contain the same nominal concentration of Er atoms; however, one set was grown on a bare sapphire substrate while the other set was deposited on a low-temperature pure ZnO buffer layer.

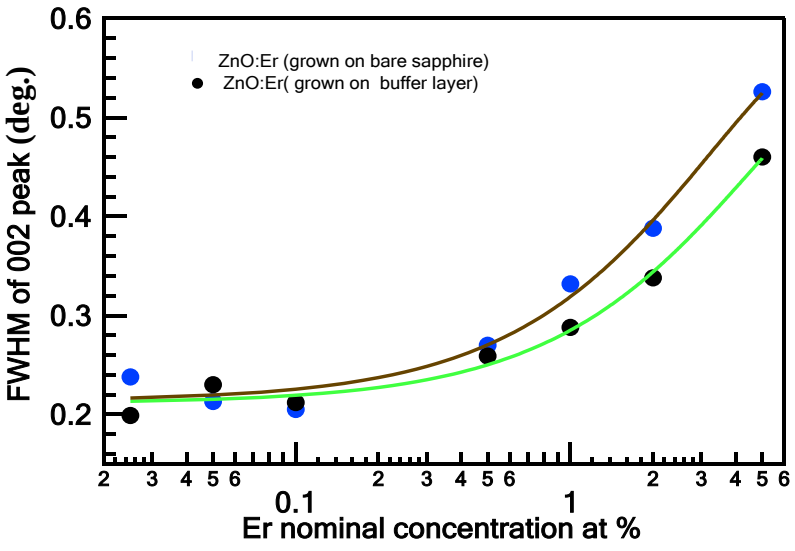

Figure 5.2 The full width at half maximum (FWHM) of (002) ZnO diffractive peaks for the two series of samples where each series contains various concentrations of Er atoms.

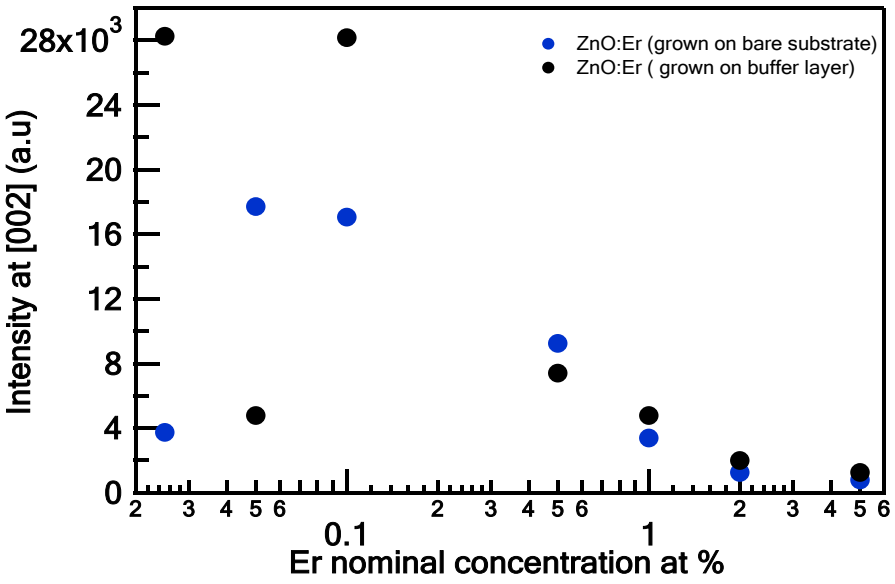

Figure 5.3 Absolute intensity of (002) ZnO diffractive peaks of different films from both set of samples as a function of Er nominal concentration.

As expected, samples deposited on a pure ZnO buffer layer have diffractive peaks that are generally narrower and more intense than those of samples grown without a buffer layer, indicating an improvement in their crystalline structure.

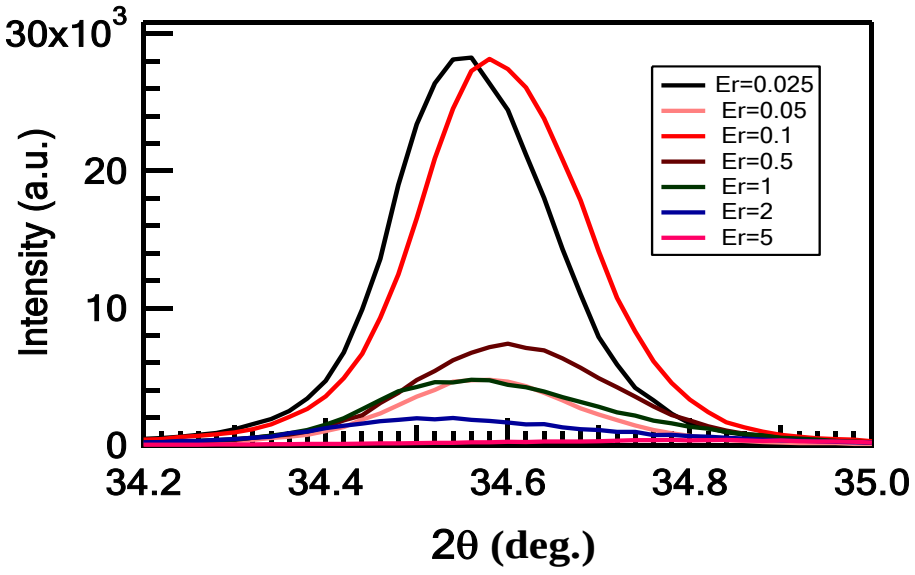

Figure 5.4 (002) ZnO XRD peak shifts for ZnO:Er films grown on a buffer layer.

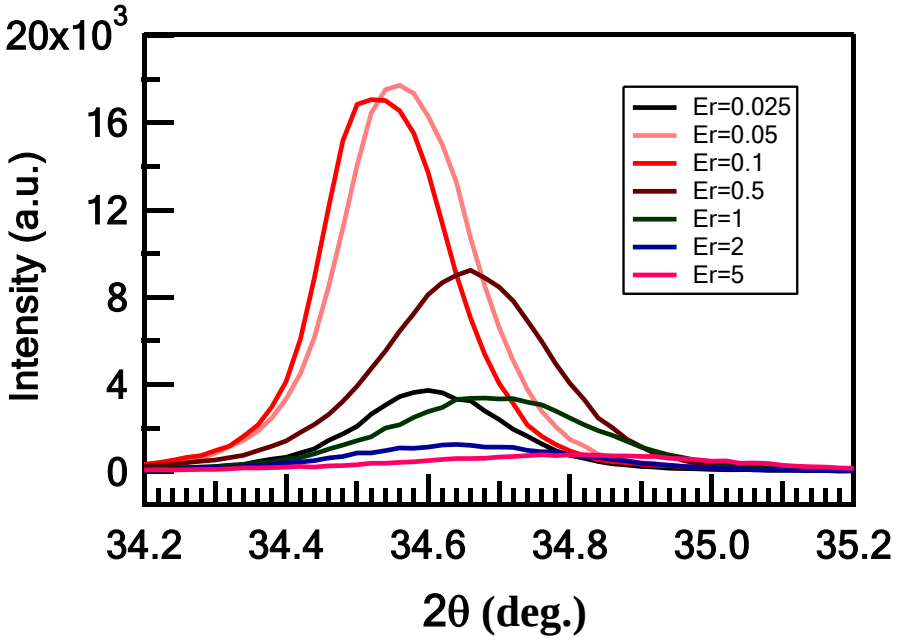

Figure 5.5 (002) ZnO XRD peak shifts for ZnO:Er films deposited on sapphire.

In general, the (002) ZnO XRD position changes to higher angles as more Er atoms are doped into the ZnO matrix, as shown in Figure 5.4 and Figure 5.5 for both sets of samples. However, this change appears in a less systematic way than in ZnO:Eu films.

This shift in the position along with the broadening of the (002) ZnO XRD peak is likely caused by the inhomogeneously residual strains in the films. For the sake of better clarity and easy comparison the data reported in Figure 5.4 and Figure 5.5 were reworked and are shown in Figure 5.6 and Figure 5.7, respectively.

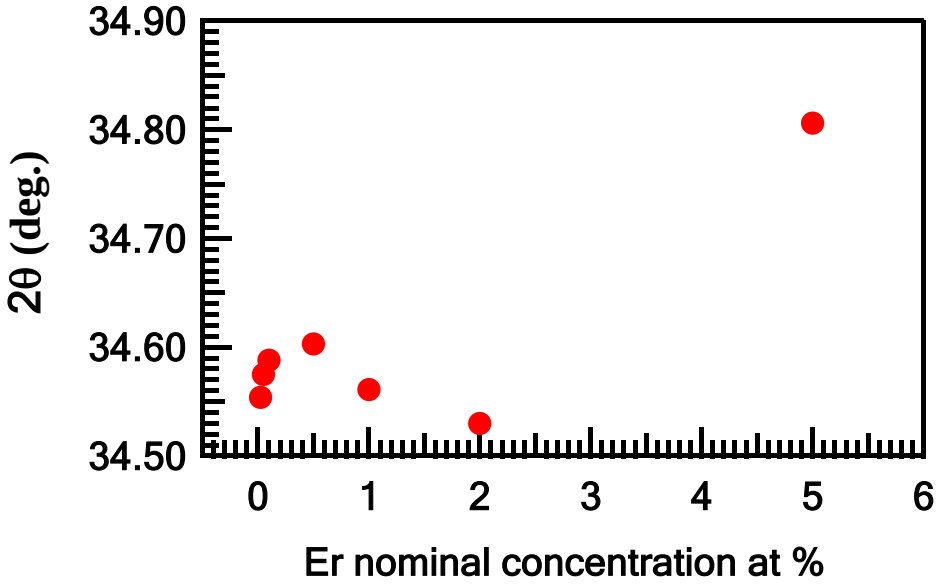

Figure 5.6 (002) XRD peak position for ZnO:Er samples grown on a buffer layer.

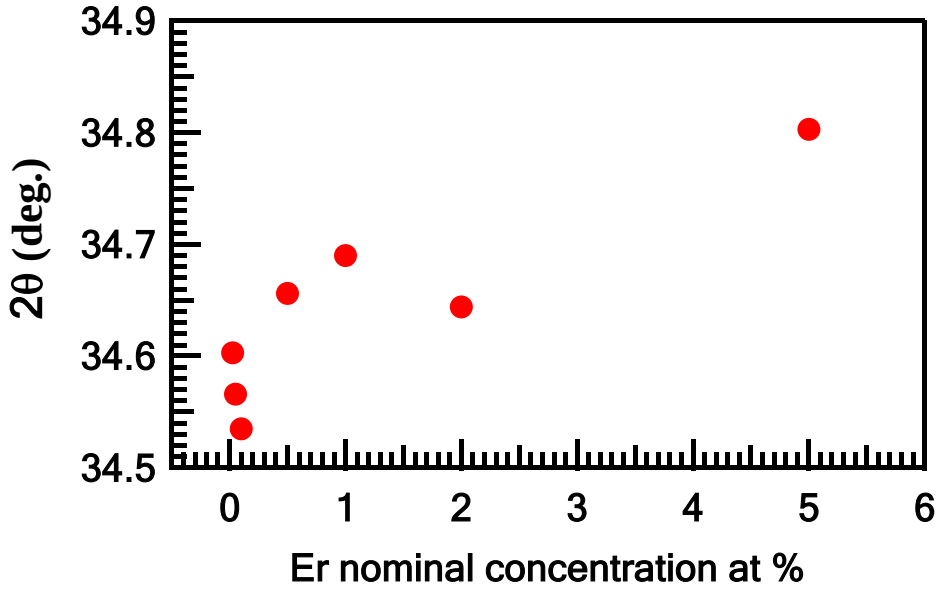

Figure 5.7 (002) XRD peak position for ZnO:Er samples deposited on sapphire.

Table 5.1 and Table 5.2 summarise the calculated values of lattice parameters, residual strain in the *c* direction, unit cell volume and crystallite size for films from both set of samples.

Table 5.1 Some crystal-related physical values calculated from XRD measurments for ZnO:Er films grown on a buffer layer.

Er (at %)	FWHM (deg.)	Lattice constants (Å)		Unit cell volume ($Å^3$)	Crystallites size (nm)	Strain (%)	Stress (GPa)
		c	*a*				
0.025	0.199	5.210	3.190	45.92	50.70	0.073	-0.342
0.05	0.23	5.206	3.188	45.83	41.63	0.014	-0.067
0.1	0.212	5.205	3.187	45.78	46.40	-0.022	0.103
0.5	0.259	5.202	3.186	45.73	35.86	-0.064	0.300
1	0.288	5.209	3.190	45.89	31.60	0.054	-0.250
2	0.338	5.213	3.192	46.01	26.31	0.141	-0.656
5	0.460	5.173	3.168	44.95	18.84	-0.636	2.958

Table 5.2 Some crystal-related physical values calculated from XRD measurments for ZnO:Er films deposited on bare sapphire.

Er (at %)	FWHM (deg.)	Lattice constants (Å)		Unit cell volume ($Å^3$)	Crystallites size (nm)	Strain (%)	Stress (GPa)
		c	*a*				
0.025	0.238	5.202	3.186	45.73	39.84361	-0.065	0.300
0.05	0.213	5.208	3.189	45.87	46.09884	0.040	-0.185
0.1	0.205	5.212	3.192	45.99	48.60226	0.127	-0.591
0.5	0.270	5.195	3.181	45.52	34.1086	-0.214	0.994
1	0.332	5.190	3.178	45.39	26.85147	-0.310	1.439
2	0.388	5.196	3.182	45.57	22.60291	-0.180	0.837
5	0.526	5.173	3.168	44.96	16.35738	-0.628	2.919

Figure 5.8 and Figure 5.9 show the development of the residual strains in ZnO:Er films as a function of Er concentration. Although there are some scattered data points, the films generally experience more compressive strain as more Er atoms are incorporated. Unlike ZnO:Eu samples ZnO:Er

films deposited on buffer layer and contained low concentration of Er atoms seeme less strained than those ZnO:Er samples grown on bare sapphire.

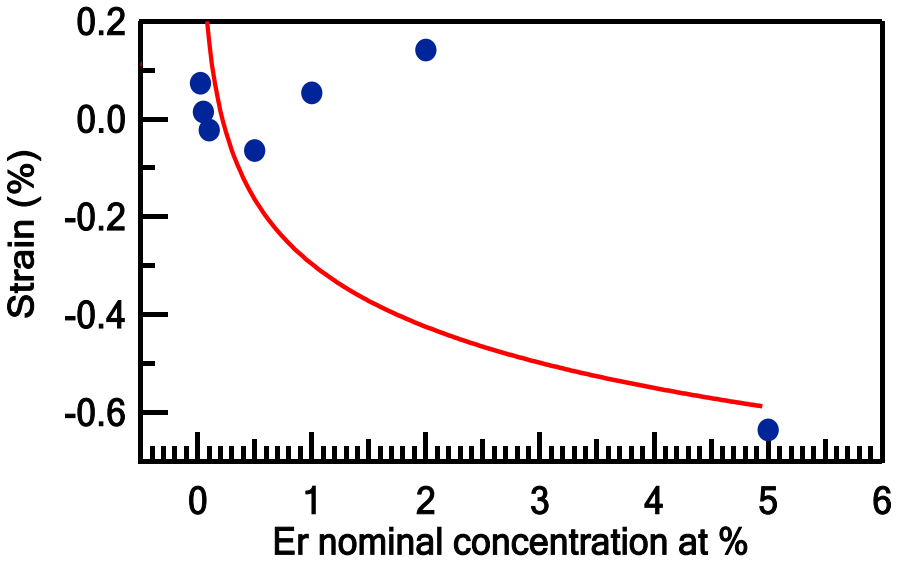

Figure 5.8 Strain trend seen in ZnO:Er samples deposited on ZnO buffer layer.

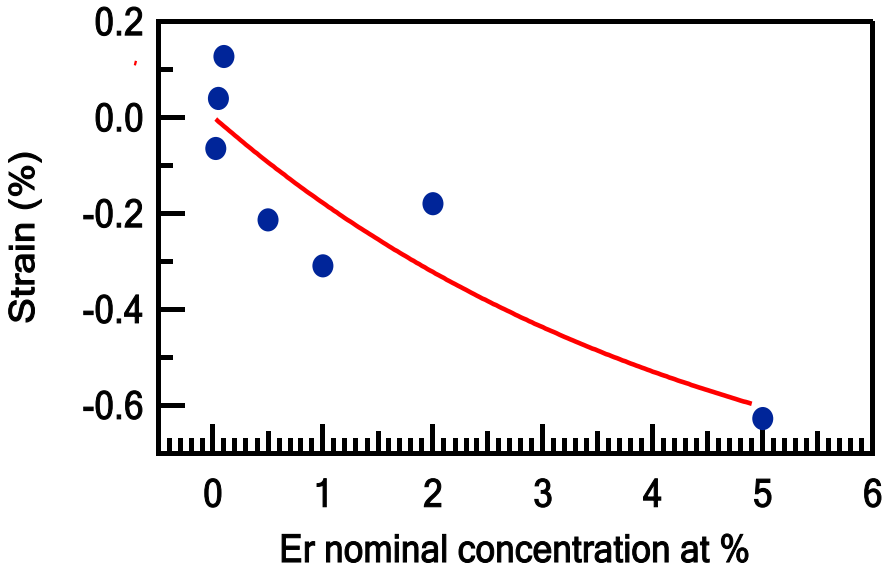

Figure 5.9 Strain trend seen in ZnO:Er samples deposited on a bare sapphire substrate.

Interestingly, as was observed in the ZnO:Eu samples, the lattice parameter (*c*) decreases with increasing concentrations of Er atoms, as shown in Figure 5.10.

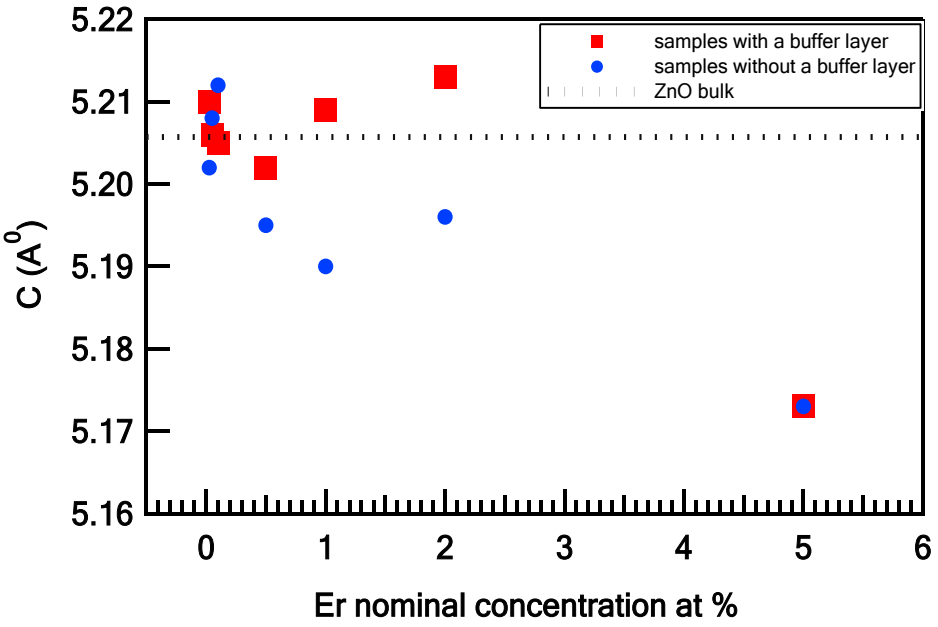

Figure 5.10 The lattice constant (*c)* of ZnO:Er films for both series of samples.

Crystallite sizes of all films belonging to both series of samples are presented in Figure 5.11 and Figure 5.12. It can be clearly seen that the crystallite size declines, as in the ZnO:Eu samples, as additional Er atoms are incorporated into the ZnO crystal.

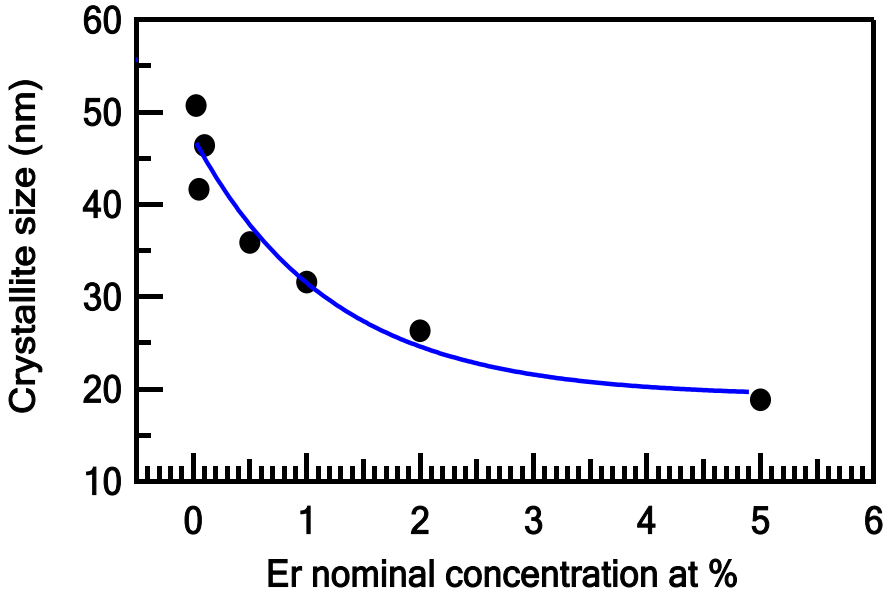

Figure 5.11 Crystallite size plot of ZnO:Er films grown on a ZnO buffer layer.

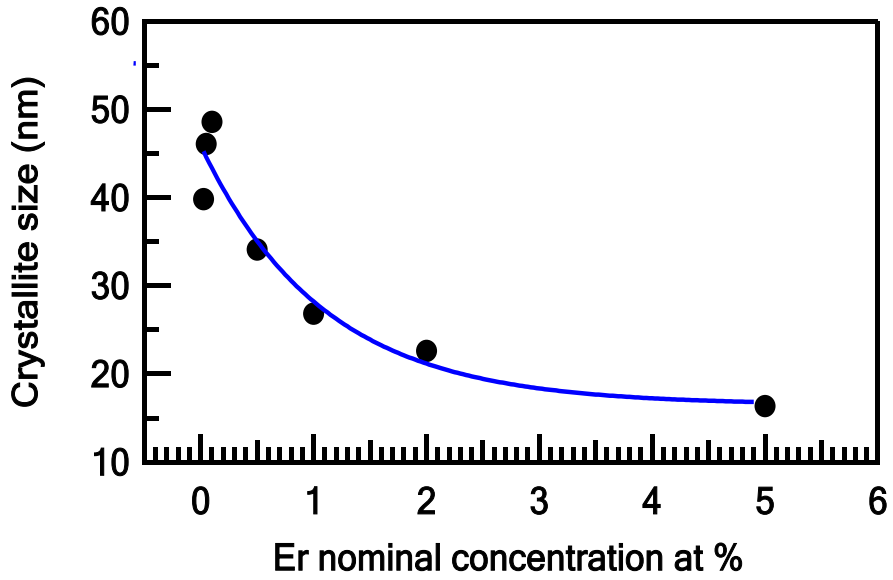

Figure 5.12 Crystallite size plot of ZnO:Er as a function of Er nominal concentration where films were grown on a bare sapphire substrate.

5.2Surface analysis

The surface morphology and roughness of ZnO:Er films were studied. SEM images of selected samples are displayed in Figure 5.13. Images for films

deposited on a low-temperature ZnO buffer layer are shown in the first row while those grown on a bare sapphire substrate are displayed in the second row. Films doped with 0.025 at.% of Er exhibit high porosity whereas films doped with higher concentrations of Er atoms show high density of crystallites. However, similar to what was observed in ZnO:Eu samples, theses grains (crystallites) become less clear as Er concentration reaches 5 at.% , which would account for the observed deterioration in crystallinity as proved by XRD measurements.

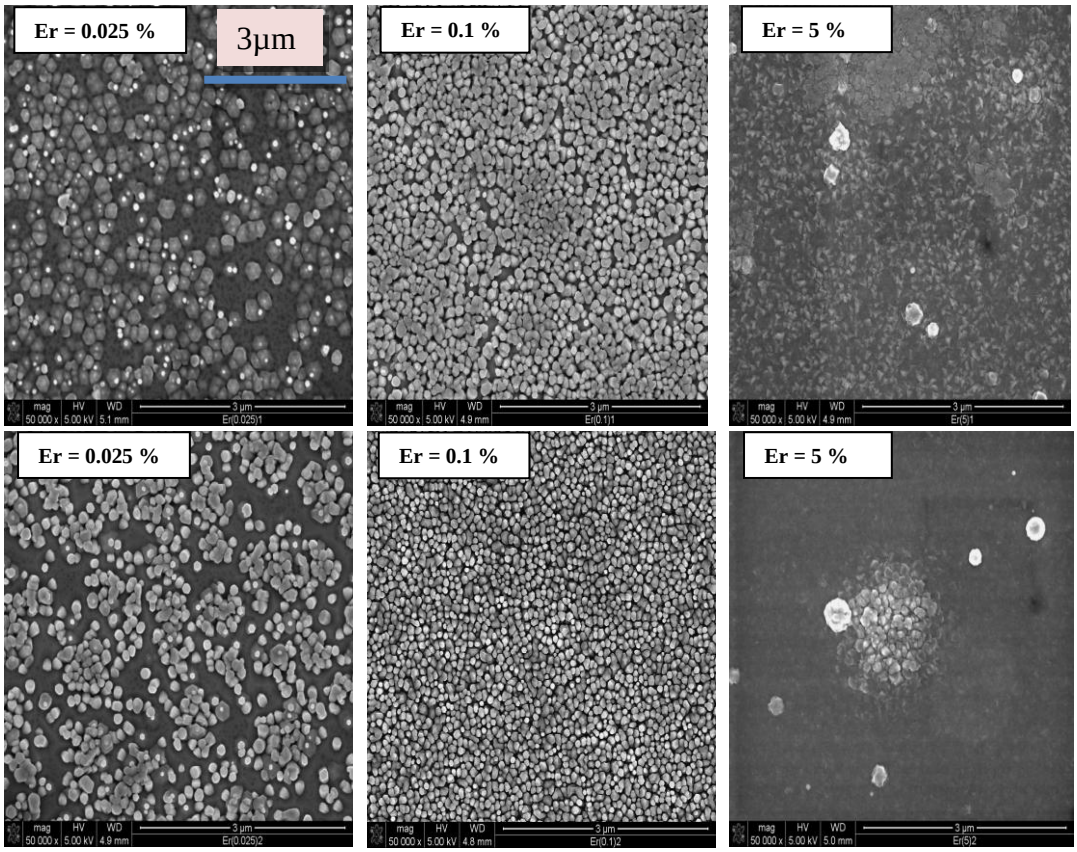

Figure 5.13 SEM images of some ZnO:Er films from both series of samples containing the same nominal concentrations of Er. Films shown in the top row have a pure ZnO buffer layer while films in the second row were deposited on bare sapphire.

The roughness data were obtained using an atomic force microscope (AFM) and are summarised in Table 5.3. Because the values are randomly scattered, it is difficult to draw any conclusions regarding the influence of Er-doping concentration on the film roughness. However, films grown on a low-temperature ZnO buffer layer generally tend to be smoother than films deposited directly on sapphire.

Table 5.3 RMS surface roughness values of ZnO:Er films from both series of samples.

Nominal concentration (at %)	RMS roughness (nm) (with buffer layer)	RMS roughness (nm) (without buffer layer)
0.025	7.40	14.0
0.05	7.50	11.0
0.1	8.50	4.50
0.5	6.40	6.80
1	6.30	5.20
2	11.0	23.6
5	7.50	10.0

5.3XPS Measurements

Wide-range XPS scans were carried out on ZnO:Er films to determine the elemental composition and relative abundance of each element on every films surface. A typical wide-range XPS spectrum of a ZnO:Er film is given in Figure 5.14. The core electron peaks used to quantify the surface of the scanned film are displayed in the wide spectrum. The estimated concentration of Er atoms on the surface of all films from both series of samples is shown in Figure 5.15, where the integrated area under both peaks of Er 4d was used to estimate the erbium concentration. In contrast to

the result from ZnO:Eu samples the estimated concentrations of Er atoms were found to be less than the nominal concentrations. The reason for this discrepancy is not known yet. However, employing an analytical technique such as RBS to investigate the compositional depth profile of europium and erbium atoms in the PLD targets may provide an explanation.

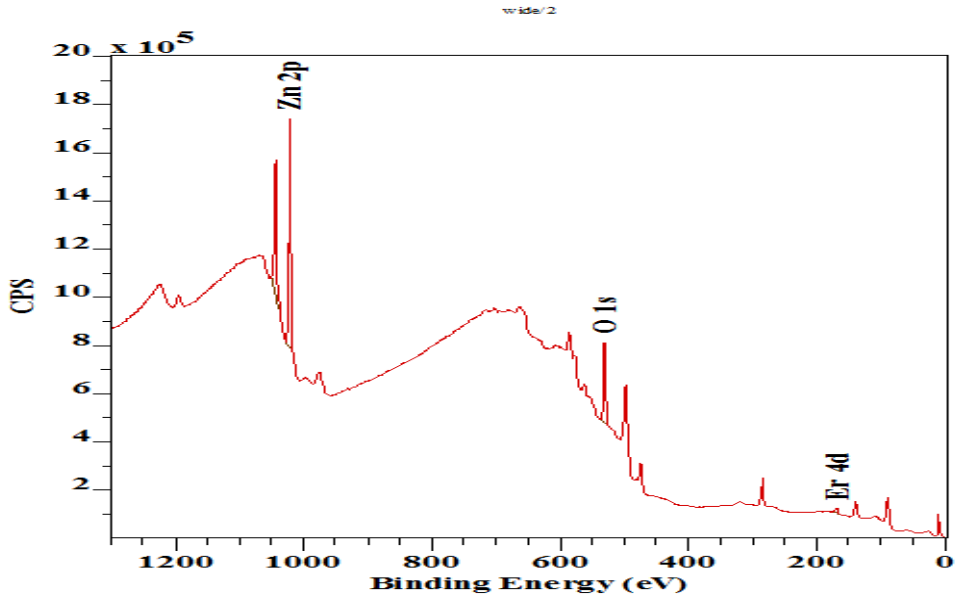

Figure 5.14 A typical XPS survey spectrum of ZnO:Er thin film.

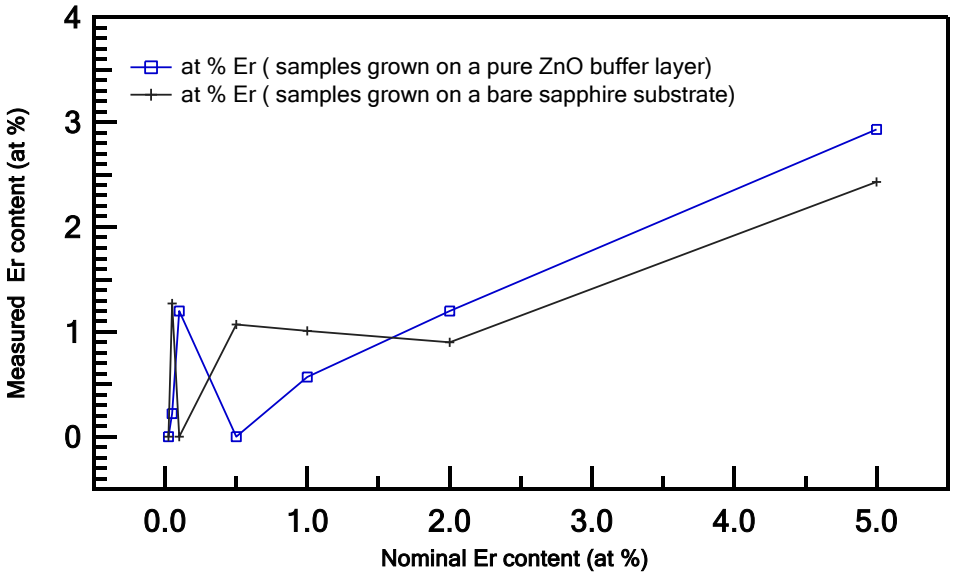

Figure 5.15 Concentration study of Er atoms on the surface of ZnO:Er films.

The stoichiometry of the ZnO:Er films was evaluated by integrating the areas underneath the O 1s and Zn 2p peaks and using their relative sensitivity factors as given in the Kratos library in the used CasaXPS processing software. Figure 5.16 and Figure 5.17 show the atomic ratios between Zn and O atoms for all ZnO:Er films considered in this thesis.

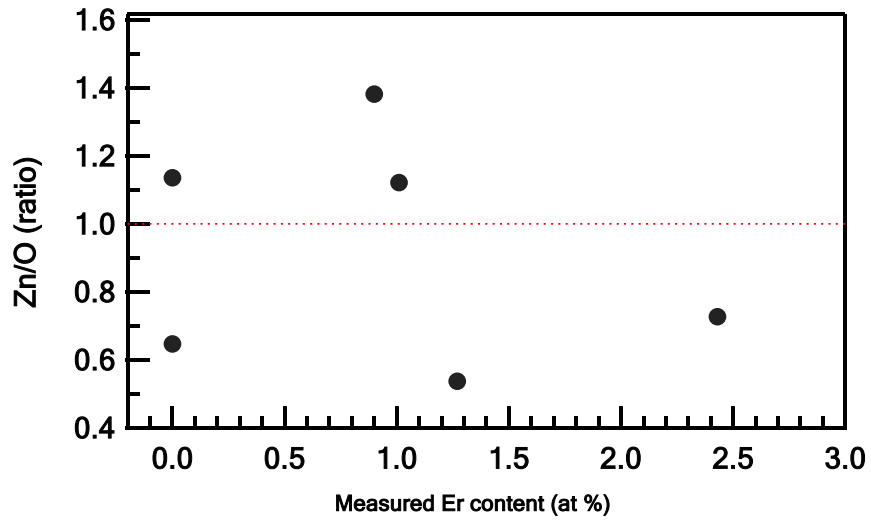

Figure 5.16 Stoichiometry study of ZnO:Er samples grown on a bare sapphire substrate.

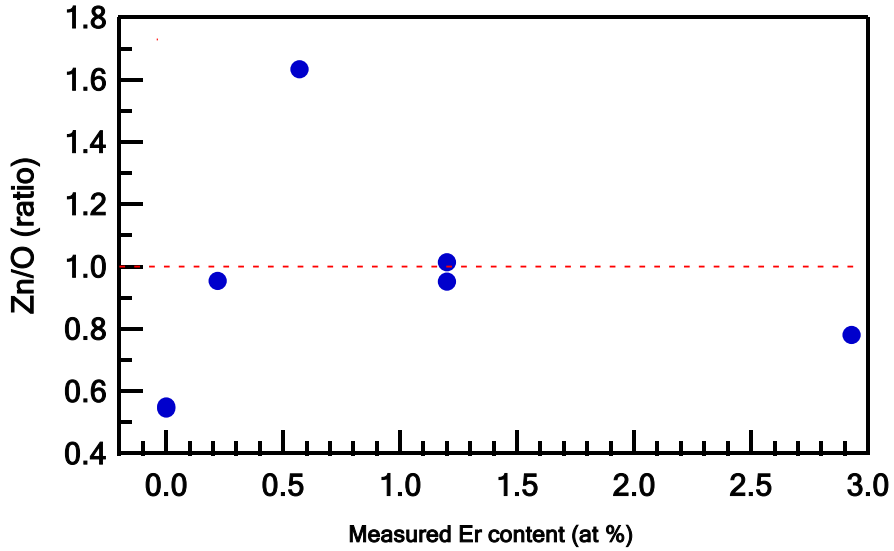

Figure 5.17 Stoichiometry study of ZnO:Er samples grown on a ZnO buffer layer.

To identify the chemical bond and oxidation state of erbium, zinc, and oxygen atoms, high resolution XPS scans were conducted. Figure 5.18 shows XPS spectra for the O 1s photoelectron peak of two doped samples containing two different nominal concentrations of erbium. It can be clearly seen that each XPS spectrum of O 1s exhibits two peaks, one in the low binding energy side at ~530.1 eV and another at ~ 531.7 eV. The first peak is attributed to O^{-2} ions in a ZnO crystal lattice while the second peak is assumed to be due to O^{-2} ions in a chemical environment similar to erbium oxide.[117] Since the binding energy of 531.7 eV matches the reported values both of loosely bound oxygen atoms residing on the surface of the film and of (Zn-OH) hydroxyl groups, it could be expected that these species are contributing to this peak.

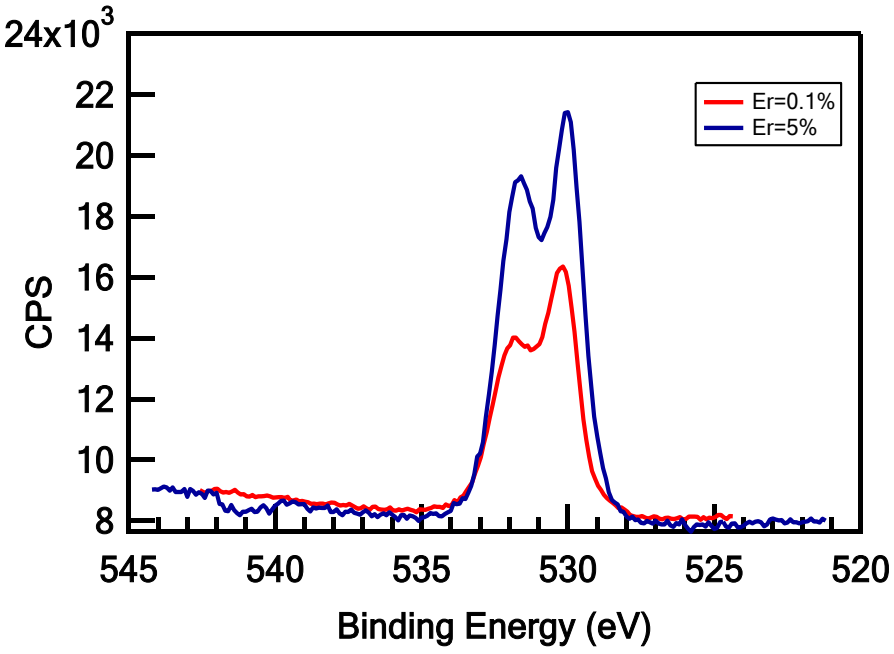

Figure 5.18 High resolution O 1s photoelectron peak.

The high resolution XPS spectra of the Zn 2p doublet peaks (Zn 2p3/2 and Zn 2p1/2) of two different ZnO:Er samples are displayed in Figure 5.19. The binding energies of Zn 2p3/2 and Zn 2p1/2 peaks are 1021.1 and

1044.2 eV, respectively. These values are typical for Zn^{2+} ions present in a ZnO crystal.

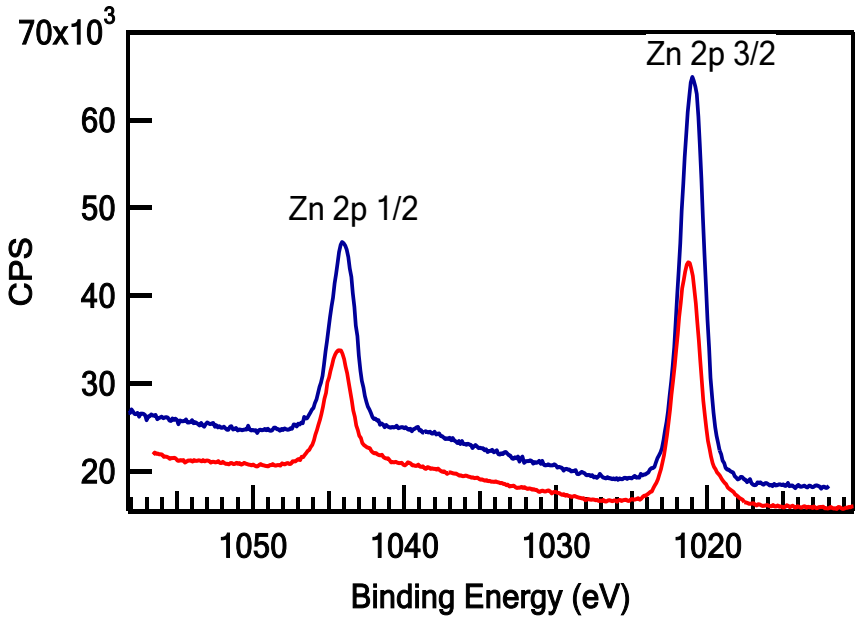

Figure 5.19 High resolution XPS scan of Zn 2p doublet peak.

The high resolution XPS spectrum of photoelectrons from the Er 4d core level is shown in Figure 5.20, where the doublet at 168.9 and 167.9 eV is characteristic of Er trivalent ions with a six-fold O coordination environment, as in Er_2O_3.[63, 118] This finding is consistent with the reported optically active Er^{3+} centre in ZnO (ErO_6), where the Er ion is located in the centre of a quasi-octahedral 6-fold oxygen coordination as evidenced by x-ray absorption fine structure analysis.[119] The broad peak, which is located at approximately 183 eV, has been ascribed to a satellite peak.[120]

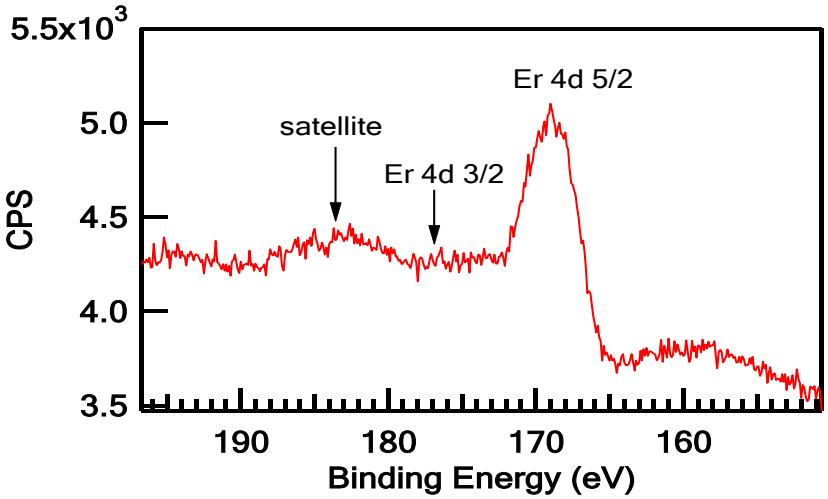

Figure 5.20 High resolution XPS spectrum of Er 4d core level.

5.4Transmission Measurements

The optical transmittance measurements for ZnO:Er films were taken at RT using the CARY 14 spectrometer. The transmissions spectra are illustrated in Figure 5.21 and Figure 5.22 for ZnO:Er samples deposited on a ZnO buffer layer and on bare sapphire, respectively. All films exhibit high optical transparency (~ 80 %) in the visible region with a sharp absorption edge at ~374 nm.

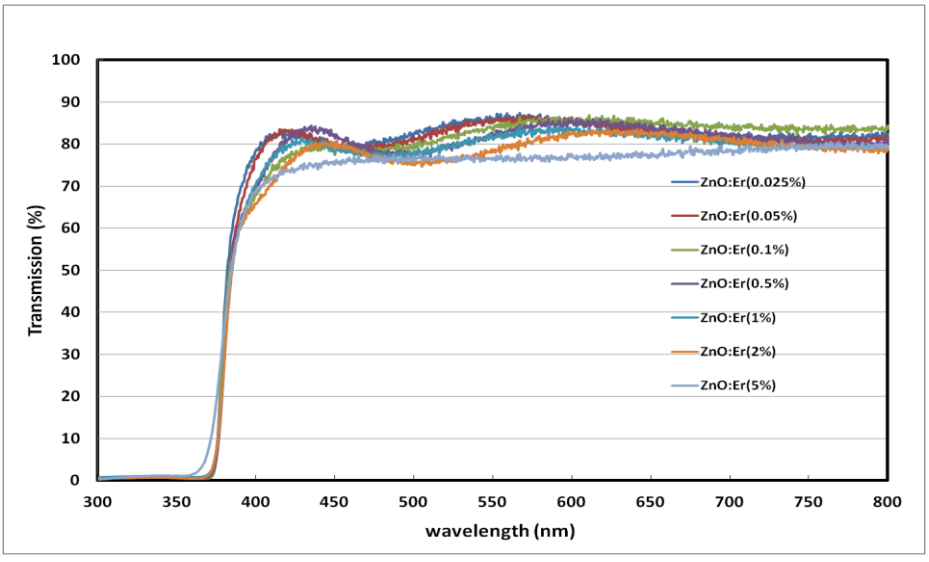

Figure 5.21 Transmission spectra of ZnO:Er films deposited on ZnO buffer layer.

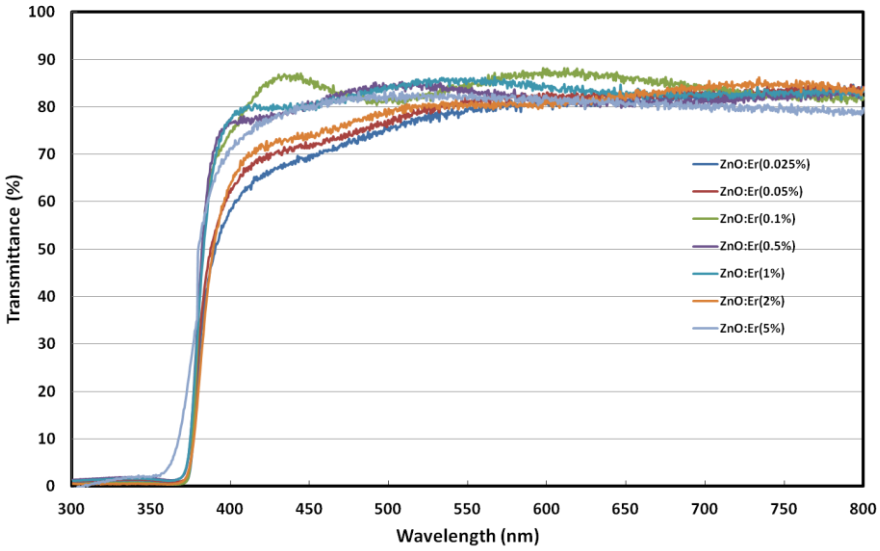

Figure 5.22 Transmission spectra of ZnO:Er films grown directly on a sapphire substrate.

The band gap energies of all ZnO:Er films were determined from the transmission spectra. Figure 5.23 and Figure 5.24 depict the determination of the band gap energy using the Tauc relation for samples grown on a ZnO buffer layer and for those grown on a sapphire substrate, respectively.

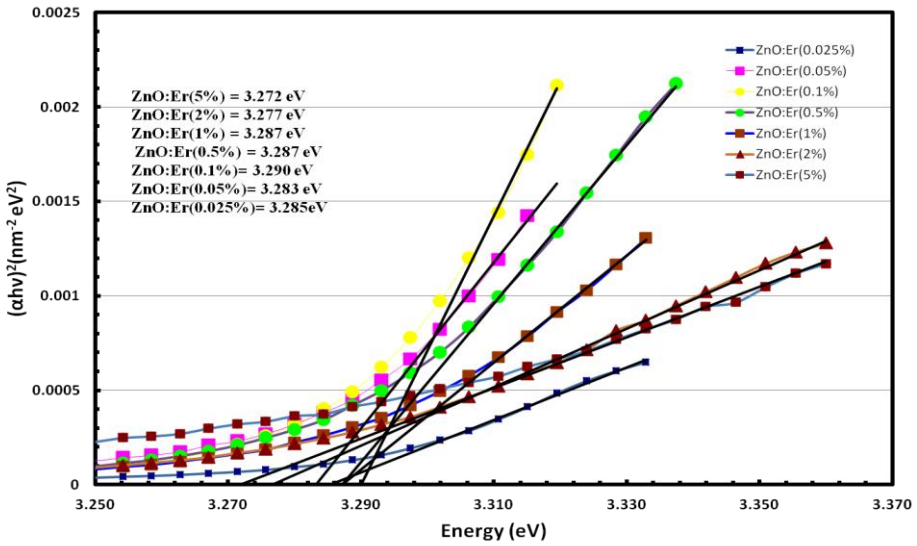

Figure 5.23 The band gap energy determination for ZnO:Er films grown on ZnO buffer layer.

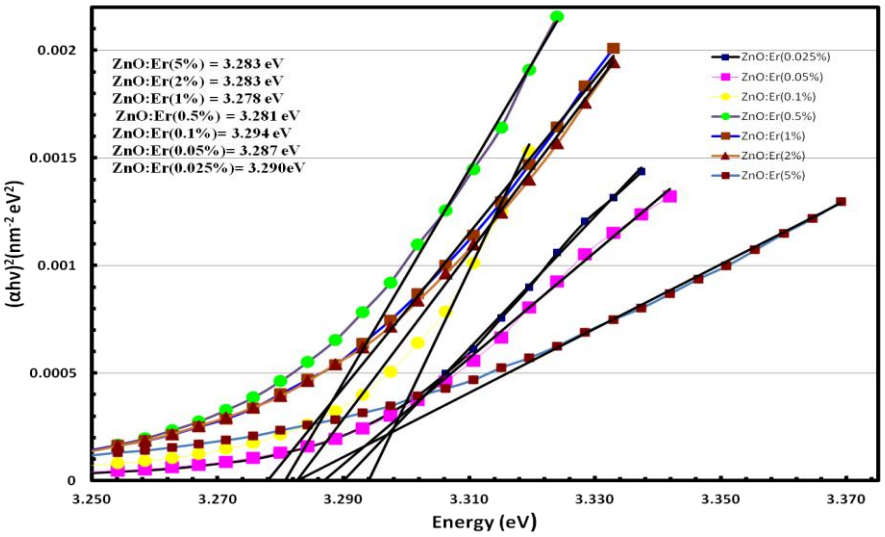

Figure 5.24 The band gap energy determination for ZnO:Er films grown on a bare sapphire substrate.

The band gap energy values of all ZnO:Er films from both sets of samples verses the residual stress values are shown in Figure 5.25 and Figure 5.26. As was observed in the ZnO:Eu samples, the samples grown on a ZnO buffer layer possess gap energies closer to the gap energy (3.4 eV at RT) of strain-free ZnO bulk.

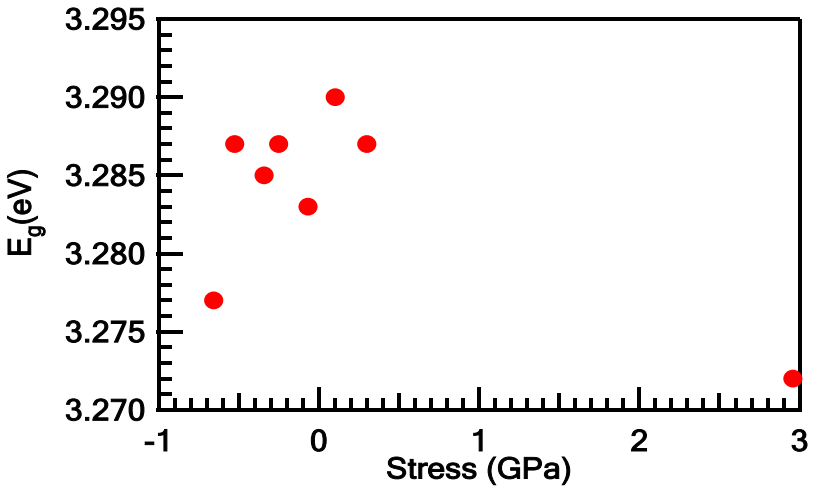

Figure 5.25 The band gap energy of ZnO:Er films grown on a buffer layer as a function of residual stress.

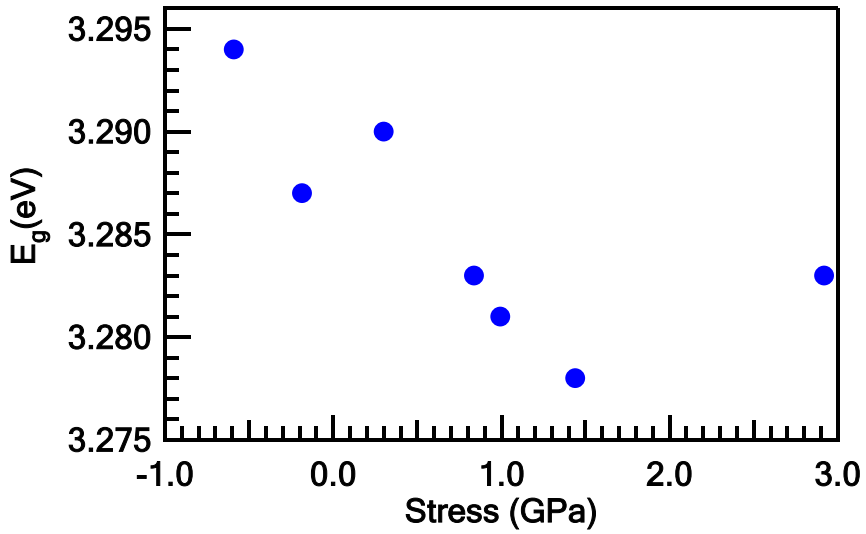

Figure 5.26 The band gap energy of ZnO:Er films grown on a bare sapphire substrate as a function of residual stress.

5.5Optical Studies

Low-temperature near band-edge PL spectra of different samples of ZnO:Er are shown in Figure 5.27. Three peaks are clearly observed. The first peak at 3.377 eV is attributed to a free exciton (I_{Fx}) and the dominant peak (I_x) is due to a bound exciton.The third peak, located at 3.331 eV and denoted by I_s, is ascribed to an exciton localised at a structural defect. However, as was previously found in ZnO:Eu samples, no PL emission in the UV region could be detected from ZnO:Er samples where the nominal concentration of erbium was greater than 0.1 at.%.

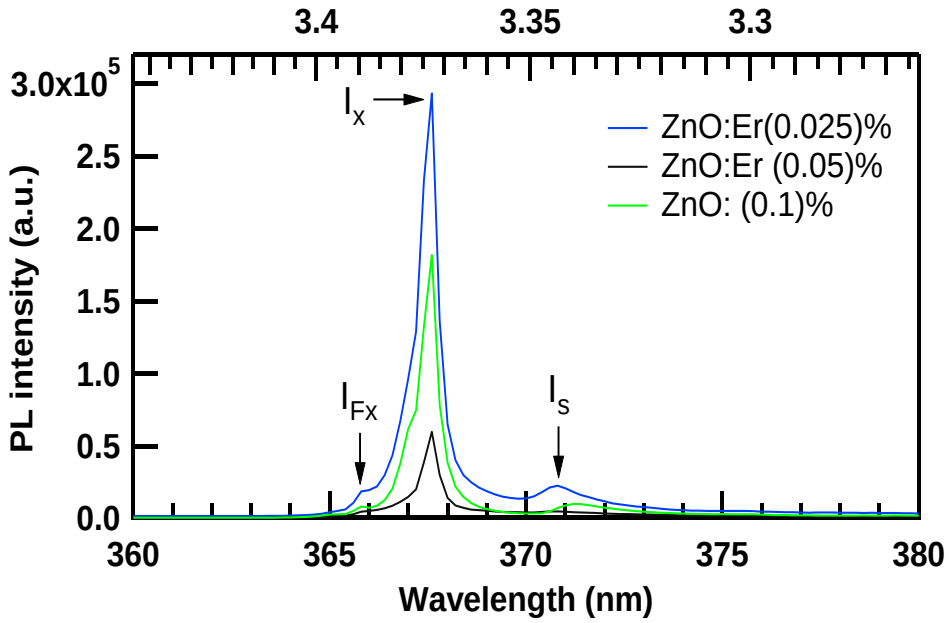

Figure 5.27 PL spectra of different ZnO:Er films having different concentration of Er atoms as shown in parentheses.

Temperature dependent photoluminescence measurements were performed on ZnO:Er (0.025%), shown in Figure 5.28, both to study the behaviour of the PL when temperature is raised and also to correctly assign the detected PL features. It is anticipated that the PL intensity of the free exciton will be enhanced by increasing the temperature because more bound excitons will be thermally dissociated into free excitons at higher temperatures.

The data in Figure 5.28 exhibit exactly this behaviour. The free-exciton peak starts out being of minor intensity at the lowest temperature, but then relatively increases with respect to I_x and even becomes dominant at temperatures above 80 K. Interestingly, I_s dies away very quickly in comparison to the other excitonic features, suggesting a smaller localisation energy. However, because this feature is observed over only a very short range of temperatures, no peak shift could be detected.

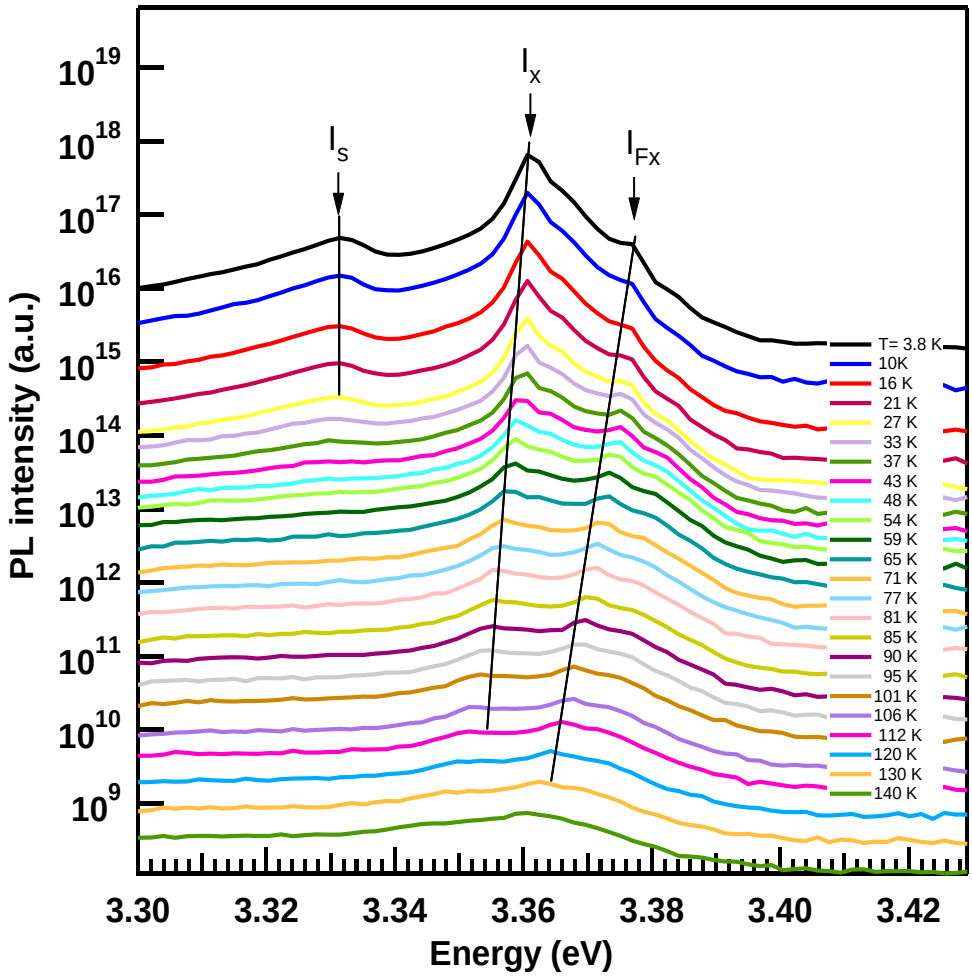

Figure 5.28 PL spectra of ZnO:Er (0.025 %) taken at different temperatures. All spectra have been vertically offset for clarity.

A curve-fitting analysis for the temperature dependent PL measurement was carried out. The thermally activated luminescence quenching behaviour of the optical features as a function of reciprocal temperature was mathematically modelled by equation (28), a single–path Arrhenius formula as shown in Figures 5.29, 5.30 and 5.31. Fitted parameters, along with the uncertainties given by the 95% confidence intervals as calculated by the IGOR curve-fitting software, are displayed in the associated figures.

The estimated E_a value for the bound exciton (I_x) was found to be ~ 12 meV, which is in reasonably good agreement with the binding energy

calculated from the energetic difference (16.4 meV) between the free and the bound excitons at 10 K. This value is also consistent with other published values for binding energies of donor bound exciton complexes of bulk ZnO lying range of (10-20 meV).[24, 110, 121-123] The donor binding energy (E_d) can be estimated by applying the Haynes Rule, equation (23), and by taking the constants A= -3.8 meV and B= 0.365 from reference [105] which gives an E_d of 43.3 eV.

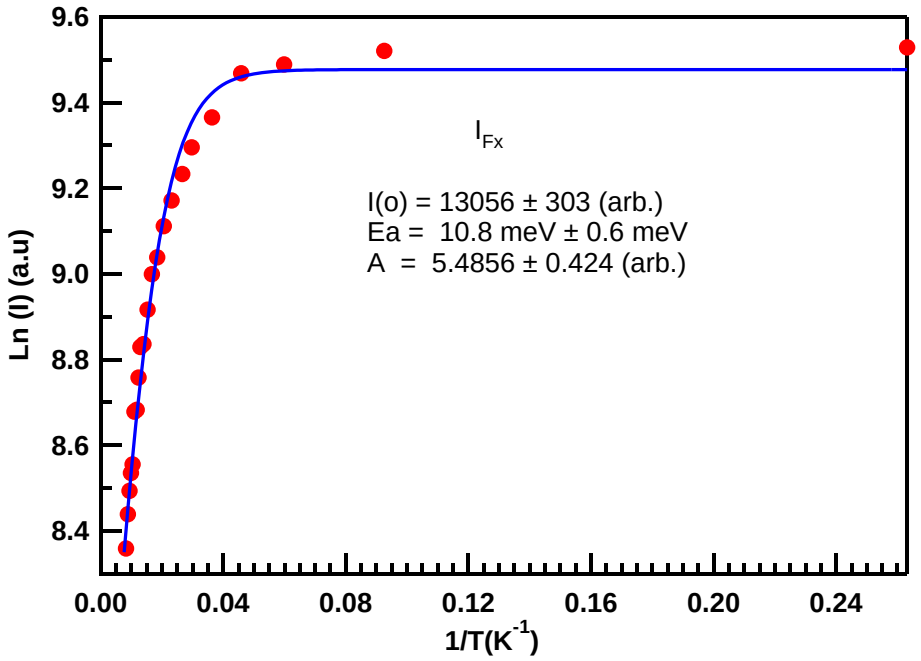

Figure 5.29 Arrhenius plot of the PL peak intensity of the recombination of the free exciton (I_{Fx}).

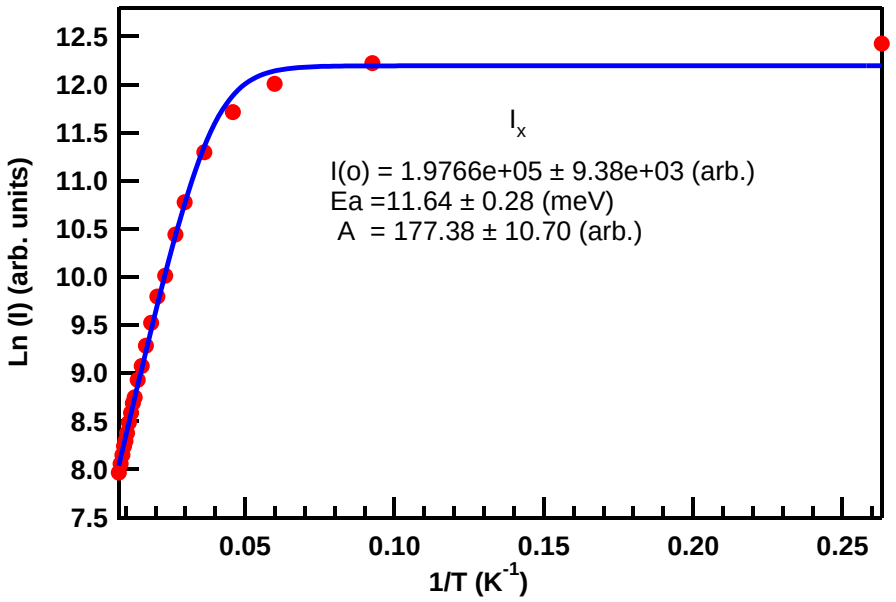

Figure 5.30 Arrhenius plot of the PL peak intensity of the recombination of the neutral donor bound exciton (I_x).

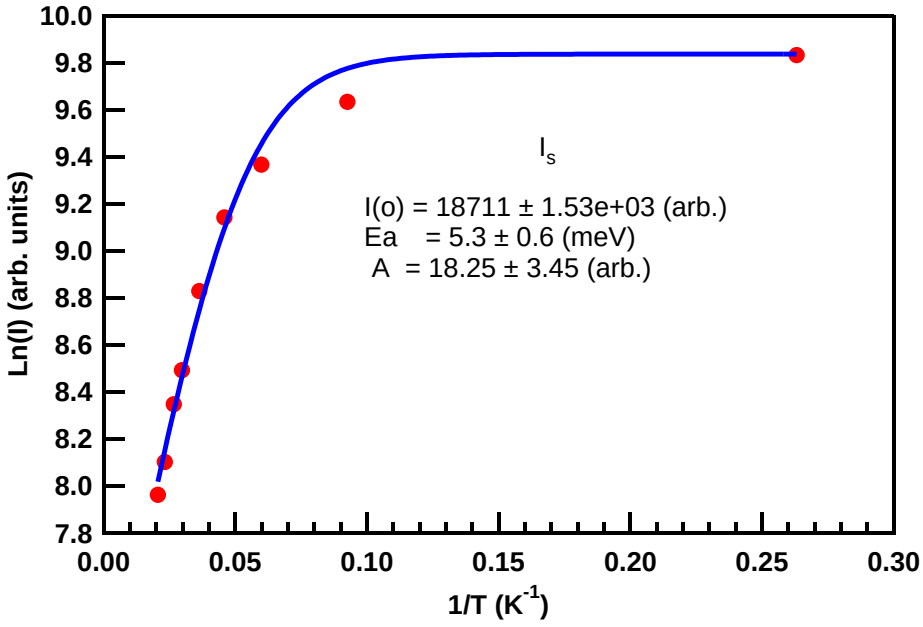

Figure 5.31 Arrhenius plot of the PL peak intensity of the bound exciton (I_s) localised at a structural defect.

An empirical equation widely used to describe the temperature dependence of the luminescent peak energy position is called the Varshni equation and is given by[124]

$$E(T) = E(0) - \frac{\alpha T^2}{\beta + T} \qquad (29)$$

where *E(0)* is the energy at T = 0 K and α and β are empirical parameters, with β being proportional to the Debye temperature T_D. At lower temperatures, β can be considered to be approximately equal to T_D. Figure 5.32 shows the temperature dependence of energy positions of I_{Fx} along with the fitted parameters.

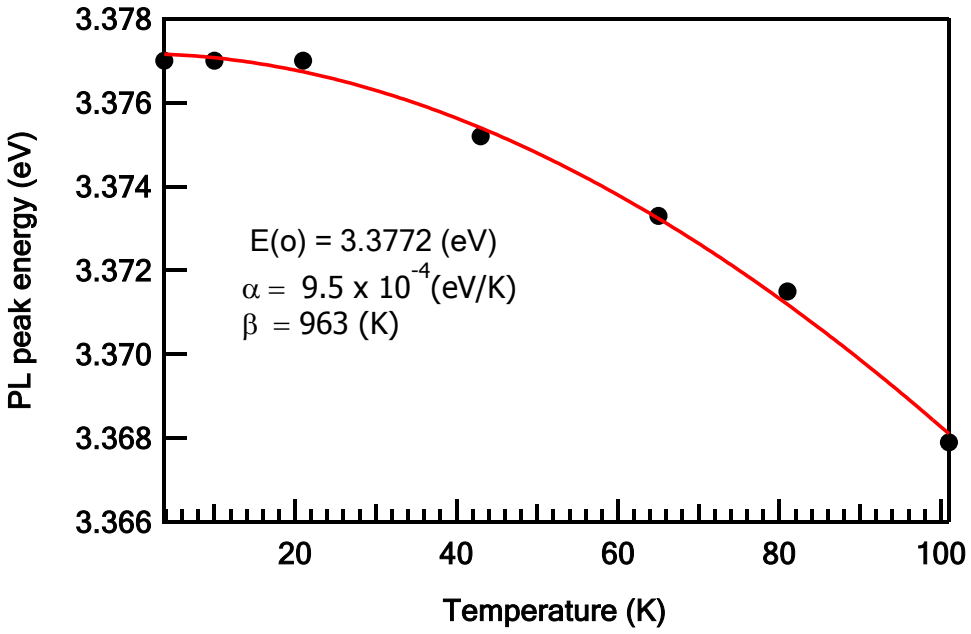

Figure 5.32 Temperature dependence of the free exciton I_{Fx} energy. The solid line shows the fit according to Varshani's relation.

The obtained fitting parameters are comparable to those reported in the literature.[125, 126]

To study the possibility of an energy transfer process between the host material (ZnO) and the dopants (Er), a He-Cd laser operating at 325 nm was used to indirectly excite Er ions doped into ZnO:Er samples. The PL spectra shown in Figure 5.33 depict the Er-related emissions from excited states. It can be seen that various emissions from Er^{3+} ions are detected and that

these are superimposed on the unstructured broad band. This band was also observed in ZnO:Eu samples as reported in Section 4.5.

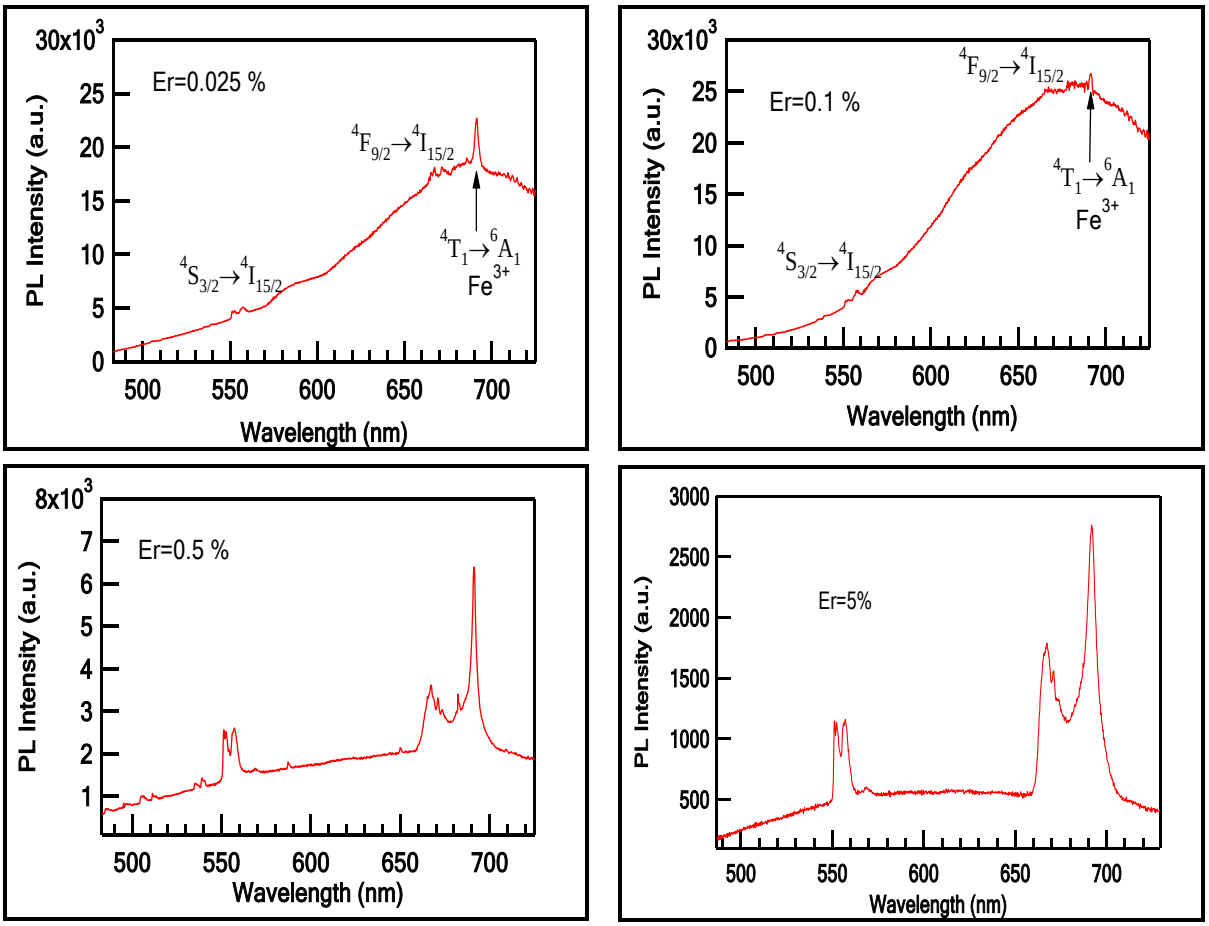

Figure 5.33 PL spectra of ZnO:Er samples at 5K excited with 325 nm.

The Er ions were directly excited using a 488 nm line of Ar^+ laser. The detected PL spectra of the $^4I_{13/2} \rightarrow {}^4I_{15/2}$ transition, taken at RT and 5 K , respectively, are displayed in Figure 5.34 and Figure 5.35. It should be recalled that this electronic transition of Er^{3+} corresponds to an emission near the 1.5 µm wavelength, which is the important region for fibre-optic telecommunication. These figures clearly show Er-related emission can be enhanced by increasing the concentration of erbium and by lowering the temperature. This emission looks relatively broad and smooth. Such broadening is attributed to the low resolution of the small monochromator

utilised in the measurements and not due to distorted crystal structure around Er^{3+} ions.

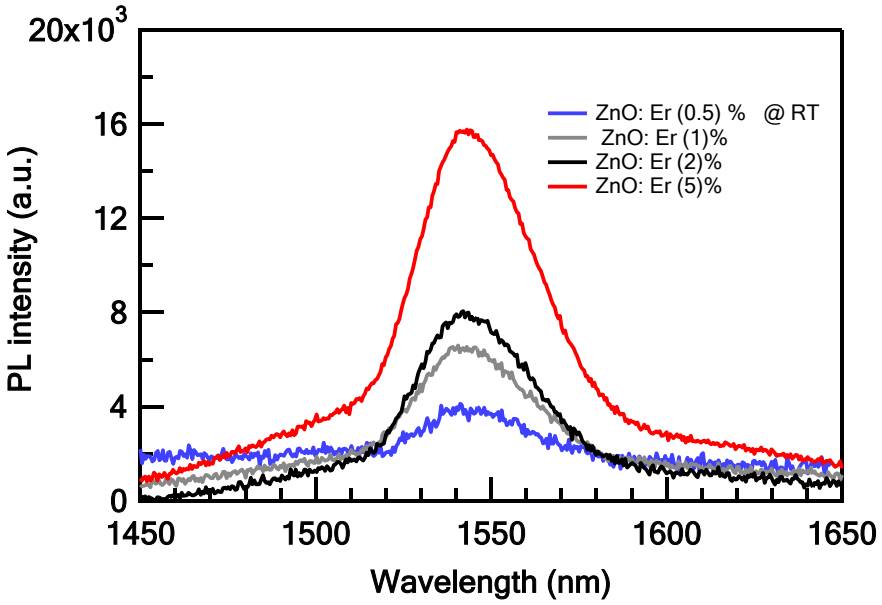

Figure 5.34 Room-temperature emission spectra near 1.54 µm of ZnO:Er samples containing different nominal erbium concentrations.

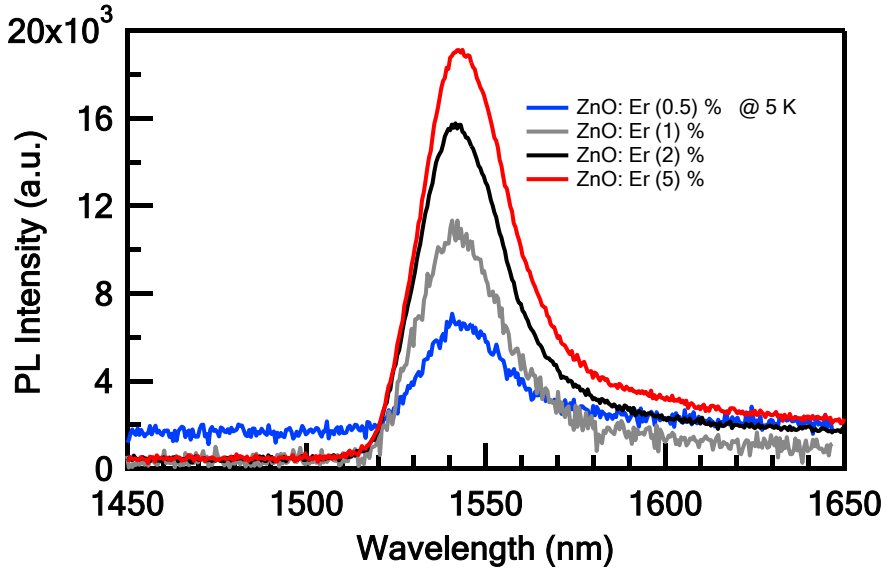

Figure 5.35 Low-temperature emission spectra near 1.54 µm of ZnO:Er samples containing different nominal erbium concentrations.

The InGaAs detector was then fitted to a high resolution monochromator (1000M HORIBA Scientific) in order to resolve any splitting of the $^4I_{13/2} \rightarrow$

$^4I_{15/2}$ transition caused by the crystal field of ZnO matrix as shown in Figure 5.36

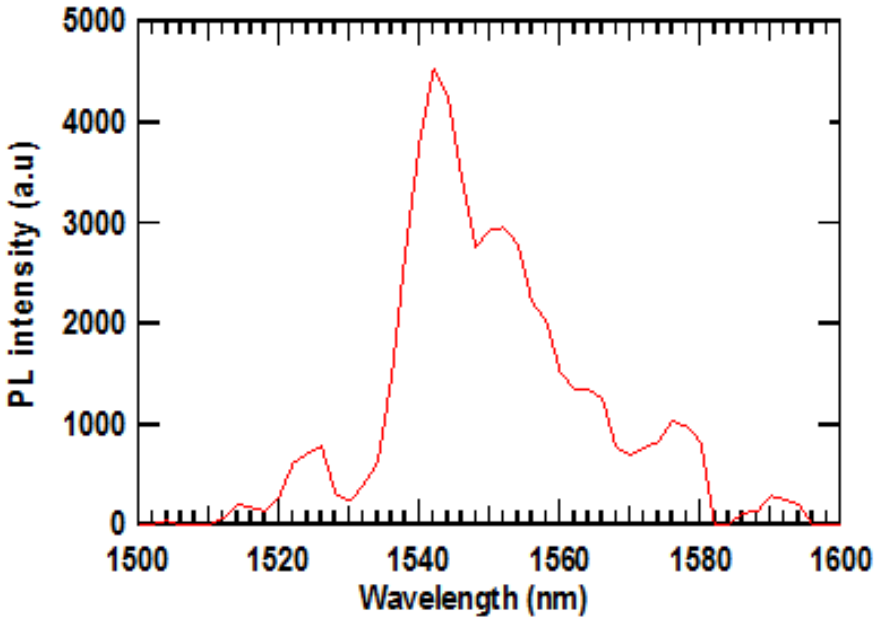

Figure 5.36 Low-temperature PL spectra near 1.54 μm of ZnO doped with 5 at.% of Er ions obtained by 1000M HORIBA monochromator.

The optically active centres of Er^{3+} ions in ZnO films were determined by Combined Excitation-Emission Spectroscopy (CEES) measurements. A Contour plot of a representative sample is shown in Figure 5.37. The nominal concentration of erbium ions is shown in the figure. The dye laser was scanned over the $^4S_{3/2}$ multiplet of Er^{3+} ions and the PL emission was detected for the $^4S_{3/2} \rightarrow {}^4I_{15/2}$ transition. As can be clearly seen from this figure, four optical centres, labelled as A, B, C and D, are identified. Centres A, B and C are believed to belong to the same site with small variation of the ligand environment around them. The PL spectra of theses optical centres are shown in Figure 5.38.

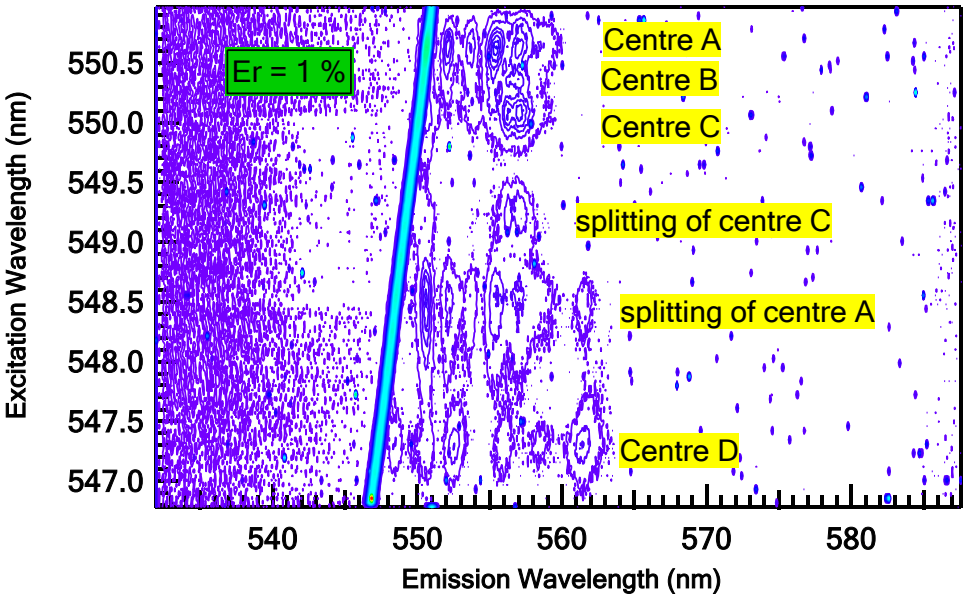

Figure 5.37 2-D contour plot of Er^{3+} centers in the ZnO film taken at ~ 4 K when pumped with the dye laser as a continuous excitation source.

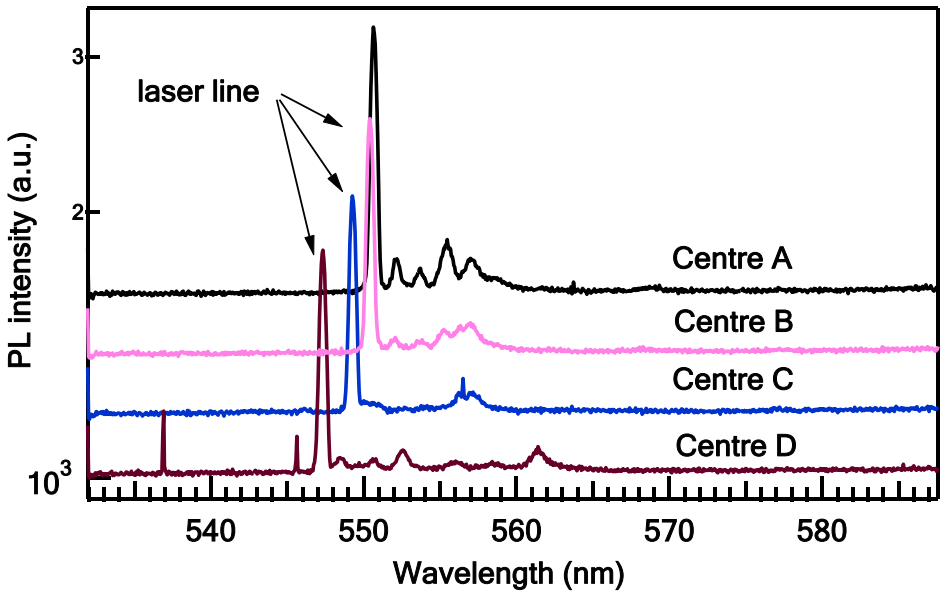

Figure 5.38 PL spectra of different optical centres of Er^{3+} ions incorporated in ZnO thin film. The nominal concentration of erbium is 1 at. %. The spectra were offset vertically for clarity.

Chapter 6

SUMMARY

In this research work two groups of ZnO thin films doped with trace amounts of rare earth (RE) ions were produced by pulsed laser deposition (PLD). One set was doped with europium and a second set was doped with erbium ions. Zinc oxide material and these particular RE elements were chosen because of their potential applications in many important fields ranging from optical communications to solar cells and lasers.

Highly dense PLD targets were successfully fabricated by means of compression and sintering. Targets of high density are an essential requirement if micro-sized particulates the commonly generated by PLD are to be avoided and high quality thin films are to be produced. It was found that a proper heating rate during the sintering process of the PLD targets is significantly crucial for obtaining a high degree of densification. By systematic investigation an optimal heating rate of 5 ^{o}C/min was adopted in this work.

All films were structurally examined by X-ray diffraction (XRD) and found to have a single-crystal hexagonal wurtzite structure preferentially oriented along the (002) direction. The film crystallinity was found to deteriorate with increasing concentrations of RE ions. It is believed that this structural deterioration resulted from the inhomogenous residual strain in the films as evidenced by the XRD measurements. This induced strain is assumed to derive from two different sources. First, large difference in ionic radii and the unequal valences of the Zn^{2+} and RE^{3+} ions can locally disturb the ZnO crystal structure and hence create strains. The second source is due to the misfit between the lattice constants and thermal coefficients of the ZnO film and the sapphire substrate.

In an attempt to partly mitigate the second source of residual strain, a pure ZnO buffer layer grown at a reduced temperature (400 ^{o}C) was introduced between the sapphire and the film. Surprisingly, ZnO:Eu films deposited on a buffer layer exhibited more compressive strain than films grown on sapphire. By contrast, ZnO:Er films with a buffer layer showed less strain than the other ZnO:Er films deposited on a bare substrate. These opposite results suggest that further investigations into the use of buffer layers should be carried out. Such work might focus, for example, on finding the optimal value of growth parameters such as temperature for the buffer layer. Thus, more suitable buffer layers can be obtained and consequently less strained films can be fabricated.

The stoichiometry of the ZnO films and the valence state of rare earth ions were determined using X-ray photoelectron spectroscopy (XPS). It was found that most of the produced films were not stoichiometric. The valence state of both europium and erbium is 3+, indicating that they exist in a chemical environment similar to Eu_2O_3 and Er_2O_3. Such a variation in stoichiometry may be due to composition changes in the PLD targets during sintering process where theses targets were heated in a high temperature environment. Therefore, spatial and in-depth compositional analysis of the PLD targets should be carried out by, for example, Rutherford backscattering (RBS) technique. This analytical study may help in understanding such variation in the films stoichiometry.

ZnO:Eu^{3+} and ZnO:Er^{3+} films showed some morphological changes with increasing nominal concentrations of rare earth ions. Films doped with < 0.5 at. % of RE ions were covered with well-defined grains (crystallites). However, these grains become hardly distinguishable as the RE ion concentrations increased.

The optical properties of the films were studied by taking light transmission, photoluminescence (PL) and combined excitation and emission spectroscopy (CEES) measurements. All films were highly transparent in the visible region of the electromagnetic spectrum with an absorption edge at ~ 375 nm. Films containing low concentrations (< 0.5 at. %) of RE ions showed a characteristic ZnO PL emission. However, no ZnO-related luminescence was observed from any samples containing higher concentrations of RE ions.

Typical intra-4f shell transitions of RE^{3+} ions were clearly seen when the rare earth ions were non-resonantly excited with UV radiation, confirming the efficient transfer of energy from the ZnO to the RE^{3+} ions. A possible mechanism for this energy transfer has been proposed.

Multiple optical centres of RE ions were identified. The ZnO:Eu^{3+} samples were found to have two different centres while ZnO:Er^{3+} films exhibited up to four optical sites. No thermal annealing process was performed to activate these optical centres.

REFERENCES

1. Takahashi, K., A. Yoshikawa, and A. Sandhu, *Wide bandgap semiconductors : fundamental properties and modern photonic and electronic devices*. 2007, Berlin: Springer.

2. Brennan, K. and P.P. Ruden, *Topics in High Field Transport in Semiconductors*. 2001, Singapore: World Scientific Publishing Co.Pte. Ltd.

3. Lutz, J., et al., *Semiconductor power devices physics, characteristics, reliability*. 2011, New York: Springer.

4. Kasap, S. and P. Capper, *Springer handbook of electronic and photonic materials*. 2006, New York: Springer.

5. Heikenfeld, J., et al., *Red light emission by photoluminescence and electroluminescence from Eu-doped GaN.* Applied Physics Letters, (1999). **75**(9): p. 1189-1191.

6. Peng, H., et al., *Spectroscopic and energy transfer studies of Eu^{3+} centers in GaN.* Journal of Applied Physics, (2007). **102**(7): p. 073520-073529.

7. Chen, G., R.G. Haire, and J.R. Peterson, *Eu^{3+} Ion Luminescence Spectra from Lanthanide Sesquioxides Exhibiting Three Different Crystal Structures.* Applied Spectroscopy, (1992). **46**(2): p. 273-276.

8. Driesen, K., V.K. Tikhomirov, and C. Grller-Walrand, *Eu^{3+} as a probe for rare-earth dopant site structure in nano-glass-ceramics.* Journal of Applied Physics, (2007). **102**(2): p. 024312-024316.

9. Favennec, P.N., et al., *Luminescence of erbium implanted in various semiconductors. IV, III-V and II-VI materials.* Electronics Letters, (1989). **25**(11): p. 718-719.

10. Bol, A.A., R. Van Beek, and A. Meijerink, *On the incorporation of trivalent rare earth ions in II-VI semiconductor nanocrystals.* Chemistry of Materials, (2002). **14**(3): p. 1121-1126.

11. Liu, Y., et al., *Optical spectroscopy of Eu^{3+} doped ZnO nanocrystals.* Journal of Physical Chemistry C, (2008). **112**(3): p. 686-694

12. Xueyuan, C., et al., *Recent Progress on Spectroscopy of Lanthanide Ions Incorporated in Semiconductor Nanocrystals.* Journal of Rare Earths, (2007). **25**(5): p. 515-525.

13. Dhanaraj, G., et al., *Springer Handbook of Crystal Growth*. 2010, Berlin,Germany: Springer.

14.Lima, S.A.M., et al., *Low-voltage electroluminescence of europium in zinc oxide thin films.* Applied Physics Letters, (2007). **90**(2): p. 023503-023505.

15.Baca, A., et al., *State-of-the-art program on compound semiconductors 50 (SOTAPOCS 50) and processes at the semiconductor solution interface 3.* SciTech Book News. Vol. 19. 2009, New Jersey: The Electrochemical Society.

16.Imataka, T., et al., *Zinc oxide varistor prepared by low-temperature sintering of ZnO nano-powder and its electrical properties.* Key Engineering Materials, (2003). **247**: p. 411-414.

17.Nahm, C.W., *Al doping effect on microstructure, electrical properties, dielectric characteristics, and aging behaviors of ZPCCY-based varistors.* Journal of Materials Science: Materials in Electronics, (2009). **20**(8): p. 718-726.

18.Anas, S., et al., *Direct synthesis of varistor-grade doped nanocrystalline ZnO and its densification through a step-sintering technique.* Acta Materialia, (2007). **55**(17): p. 5792–5801.

19.Durán, P., J. Tartaj, and C. Moure, *Fully dense, fine-grained, doped zinc oxide varistors with improved nonlinear properties by thermal processing optimization.* Journal of the American Ceramic Society, (2003). **86**(8): p. 1326-1329

20.Senda, T. and R.C. Bradt, *Grain growth in sintered ZnO and ZnO-Bi_2O_3 ceramics.* Journal of the American Ceramic Society, (1990). **73**(1): p. 106-114.

21.Kim, H. and D.W. Kim, *Silver Schottky contacts to a -plane bulk ZnO.* Journal of Applied Physics, (2010). **108**(7): p. 074514-074519.

22.Pearton, S., *GaN and ZnO-based Materials and Devices*. 2012, Dordrecht: Springer.

23.Janotti, A. and C.G. Van De Walle, *Fundamentals of zinc oxide as a semiconductor.* Reports on Progress in Physics, (2009). **72**(12): p. 126501-126530.

24.Litton, C.W.C., Thomas C.
Reynolds, Donald C.
Capper, Peter, S. Kasap, and A. Willoughby, *Zinc Oxide Materials for Electronic and Optoelectronic Device Applications*. 2011, Hoboken: John Wiley & Sons.

25.Guo, W., *Epitaxial growth and properties of ZnO thin films on si substrates*, in *Materials Science and Engineering*. 2010, The University of Michigan Ann Arbor,USA.

26.Demidenko, V.A., et al., *Scintillation properties of ceramics based on zinc oxide.* Radiation Measurements, (2007). **42**(4-5): p. 549-552.

27.Li, W., et al., *Characteristics of ZnO:Zn phosphor thin films by post-deposition annealing.* Nuclear Instruments and Methods in Physics Research, Section B: Beam Interactions with Materials and Atoms, (2000). **169**(1-4): p. 59-63.

28.Ginley, D., H. Hosono, and D. Paine, *Handbook of Transparent Conductors*. 2010, Dordrecht: Springer.

29.Morkoç, H. and Ü. Özgür, *Zinc oxide: fundamentals, materials and device technology*. 2009, Weinheim: Wiley-VCH.

30.Klingshirn, C., et al., *Zinc Oxide: from fundamental properties towards novel applications*. 2010, Berlin: Springer.

31.Duffy, J.A., *Ionic-covalent character of metal and nonmetal oxides.* Journal of Physical Chemistry A, (2006). **110**(49): p. 13245-13248

32.Morgan, S.W.K., *Zinc and its alloys and compounds*. 1985, New York: Distributors, Halsted Press.

33.Bergman, J. and L. McHale, *Handbook of luminescent semiconductor materials*. 2012, Boca Raton, FL: CRC Press.

34.Klason, P., et al., *Temperature dependence and decay times of zinc and oxygen vacancy related photoluminescence bands in zinc oxide.* Solid State Communications, (2008). **145**(5-6): p. 321-326.

35.Reshchikov, M.A. and H. Morkoç, *Luminescence properties of defects in GaN.* Journal of Applied Physics, (2005). **97**(6): p. 061301-61396.

36.Teke, A., et al., *Excitonic fine structure and recombination dynamics in single-crystalline ZnO.* Physical Review B - Condensed Matter and Materials Physics, (2004). **70**(19): p. 195207-195217.

37.Gupta, C.K. and N. Krishnamurthy, *Extractive metallurgy of rare earths*. 2005, Boca Raton, Florida.: CRC Press.

38.Accorsi, G., *Trivalent Lanthanide Ions: Luminescence and Applications*, in *Chemical Sciences* 2007, The University of Bologna: Bologna, Italy.

39.Becker, P.C., N.A. Olsson, and J.R. Simpson, *Erbium-doped fiber amplifiers : fundamentals and technology*. Optics and photonics. 1999, San Diego: Academic Press.

40.Digonnet, M.J.F., *Rare earth doped fiber lasers and amplifiers*. 1993, New York: Marcel Dekker.

41.Wybourne, B.G., *Spectroscopic properties of rare earths*. 1965, New York: Interscience Publishers.

42.Gschneidner Jr, K.A., V.K. Pecharsky, and J.-C. Bunzli, *Handbook on the Physics and Chemistry of Rare Earths. Vol. 37*. 2007, Amesterdam: Elsevier.

43.Dieke, G., *Spectra and energy levels of rare earth ions in crystals*. 1968, New York,USA: John Wiley & Sons, Inc.

44.*http://www.tasmanmetals.com/s/Applications.asp*.

45.*http://www.reehandbook.com/*.

46.Stwertka, A., *A guide to the elements*. 2002, New York: Oxford University Press.

47.Levine, A.K. and F.C. Palilla, *A new, highly efficient red-emitting cathodoluminescent phosphor (YVO_4:Eu) for color television.* Applied Physics Letters, (1964). **5**(6): p. 118-120

48.Chrisey, D.B. and G.K. Hubler, *Pulsed Laser Deposition of Thin Films*. 1994: John Wiley & Sons.

49.German, R.M., *Sintering theory and practice*. 1996, New York: Wiley.

50.Rahaman, M.N., *Ceramic processing and sintering*. 1995, New York: M. Dekker.

51.Lee, W.E. and W.M. Rainforth, *Ceramic microstructures : property control by processing*. 1994, London: Chapman & Hall.

52.Boch, P. and J.-C. Nièpce, *Ceramic Materials: Processes, Properties, and Applications*. 2010, London,UK: ISTE Ltd.

53.Hynes, A.P., R.H. Doremus, and R.W. Siegel, *Sintering and characterization of nanophase zinc oxide.* Journal of the American Ceramic Society, (2002). **85**(8): p. 1979-1987.

54.Mazaheri, M., S.A. Hassanzadeh-Tabrizi, and S.K. Sadrnezhaad, *Hot pressing of nanocrystalline zinc oxide compacts: Densification and grain growth during sintering.* Ceramics International, (2009). **35**(3): p. 991-995.

55.Oszwaldowski, M., et al., *Pulsed laser deposition of II-VI semiconductor thin films and their layered structures.* Journal of Alloys and Compounds, (2004). **371**(1-2): p. 164-167.

56.Maiman, T.H., *Stimulated optical radiation in Ruby.* Nature, (1960). **187**(4736): p. 493-494.

57.Smith, H.M. and A.F. Turner, *Vacuum Deposited Thin Films Using a Ruby Laser*. Applied Optics, (1965). **4**(1): p. 147-148.

58.Mendelsberg, R., *Photoluminescence of ZnO grown by eclipse pulsed laser deposition*, in *Physics and Astronomy*. 2009, University of Canterbury: Christchurch, New Zealand.

59.Eason, R.W., *Pulsed laser deposition of thin films: applications-led growth of functional materials*. 2007, Hoboken, USA: John Wiley & Sons, Inc.

60.Singh, R.K. and J. Narayan, *Pulsed-laser evaporation technique for deposition of thin films: Physics and theoretical model.* Physical Review B, (1990). **41**(13): p. 8843-8859.

61.Kramer, B., *Advances in Solid State Physics*. Vol. 43. 2003, Berlin,Germany: Springer-Verlag.

62.Willmott, P.R., P. Manoravi, and K. Holliday, *Production and characterization of Nd, Cr:GSGG thin films on Si(001) grown by pulsed laser ablation.* Applied Physics A: Materials Science and Processing, (2000). **70**(4): p. 425-429

63.Komuro, S., et al., *Highly erbium-doped zinc-oxide thin film prepared by laser ablation and its 1.54 μm emission dynamics.* Journal of Applied Physics, (2000). **88**(12): p. 7129 - 7136.

64.Komuro, S., et al., *Room-temperature luminescence from erbium-doped silicon thin films prepared by laser ablation.* Applied Physics Letters, (1996). **69**(25): p. 3896-3898.

65.Smart, L.E. and E.A. Moore, *Solid state chemistry: an introduction*. 2005, Boca Raton,USA: CRC/Taylor & Francis.

66.Stout, G.H. and L.H. Jensen, *X-ray structure determination: a practical guide*. 1989, New York,USA: A Wiley-Interscience publication

67.Rao, T.P., et al., *Effect of stress on optical band gap of ZnO thin films with substrate temperature by spray pyrolysis.* Journal of Alloys and Compounds, (2009). **485**(1-2): p. 413-417.

68.Ruthe, K.C. and S.A. Barnett, *Glancing-angle ion-assisted deposition of ZnO thin films.* Surface Science, (2003). **538**(1-2): p. L460-L464.

69.Park, S.H., et al., *Lattice relaxation mechanism of ZnO thin films grown on c-Al $_2O_3$ substrates by plasma-assisted molecular-beam epitaxy.* Applied Physics Letters, (2007). **91**(23): p. 231904-231907.

70.Mass, J., P. Bhattacharya, and R.S. Katiyar, *Effect of high substrate temperature on Al-doped ZnO thin films grown by pulsed laser deposition.* Materials Science and Engineering B: Solid-State Materials for Advanced Technology, (2003). **103**(1): p. 9-15.

71.Vickerman, J.C. and I.S. Gilmore, *Surface Analysis: The Principal Techniques*. 2009, Hoboken,UK.: John Wiley & Sons, Ltd.

72.Watts, J.F. and J. Wolstenholme, *An introduction to surface analysis by XPS and AES*. 2003, Chichester,UK: John Wiley & Sons Ltd.

73.Vij.D.R, *Handbook of applied solid state spectroscopy*. 2006, New York; USA: Springer.

74.Watts, J.F., *X-ray photoelectron spectroscopy.* Vacuum, (1994). **45**(6-7): p. 653-671.

75.Barr, T.L. and S. Seal, *Nature of the use of adventitious carbon as a binding energy standard.* Journal of Vacuum Science and Technology A: Vacuum, Surfaces and Films, (1995). **13**(3): p. 1239-1246.

76.Mandal, S., et al., *Optical and structural characteristics of ZnO thin films grown by rf magnetron sputtering.* Materials Research Bulletin, (2008). **43**(2): p. 244-250.

77.Zhou, W. and Z.L. Wang, *Scanning microscopy for nanotechnology: techniques and applications*. 2007, New York,USA: Springer.

78.Fahlman, B.D., *Materials chemistry*. 2007, Dordrecht, Netherlands: Springer.

79.Khursheed, A., *Scanning Electron Microscope Optics and Spectrometers*. 2010, Singapore, Singapore: World Scientific publishing Co. Ltd.

80.Kohli, K. and K. Mittal, *Developments in Surface Contamination and Cleaning Fundamentals and Applied Aspects*. 2008, New York,USA: William Andrew,Inc.

81.Abou-Ras, D., T. Kirchartz, and U. Rau, *Advanced characterization techniques for thin film solar cells*. 2010, Weinheim, Germany: Wiley-VCH.

82.Jeong, I.S., et al., *n-ZnO/p-Si UV photodetectors employing AlO_x films for antireflection.* Thin Solid Films, (2004). **447-448**: p. 111-114.

83.Lampert, M.A., *Mobile and immobile effective-mass-particle complexes in nonmetallic solids.* Physical Review Letters, (1958). **1**(12): p. 450-453.

84.Yu, P. and M. Cardona, *Fundamentals of Semiconductors: Physics and Materials Properties*. 2010, New York,USA: Springer.

85.Dutta, A., *Semiconductor devices and circuits*. 2008, New Delhi,India: Oxford University Press.

86.Allenic, A., *Structural, electrical and optical properties of p-type ZnO epitaxial films* in *Materials Science and Engineering*. 2008, The University of Michigan: Ann Arbor,USA.

87.Haynes, J.R., *Experimental proof of the existence of a new electronic complex in silicon.* Physical Review Letters, (1960). **4**(7): p. 361-363.

88.Chen, H., et al., *Low-temperature buffer layer for growth of a low-dislocation-density SiGe layer on Si by molecular-beam epitaxy.* Journal of Applied Physics, (1996). **79**(2): p. 1167-1169.

89.Xiu, F.X., et al., *ZnO growth on Si with low-temperature CdO and ZnO buffer layers by molecular-beam epitaxy.* Journal of Electronic Materials, (2006). **35**(4): p. 691-694.

90.Wang, H.H., X.-Z. Yuan, and H. Li, *PEM fuel cell diagnostic tools*. 2012, Boca Raton, FL: CRC Press/Taylor & Francis.

91.Ghosh, R., D. Basak, and S. Fujihara, *Effect of substrate-induced strain on the structural, electrical, and optical properties of polycrystalline ZnO thin films.* Journal of Applied Physics, (2004). **96**(5): p. 2689-2692.

92.Nakamura, T., et al., *Improvement in the crystallinity of ZnO thin films by introduction of a buffer layer.* Thin Solid Films, (2002). **411**(1): p. 60-64.

93.Perriére, J., et al., *Comparison between ZnO films grown by femtosecond and nanosecond laser ablation.* Journal of Applied Physics, (2002). **91**(2): p. 690-696

94.Pérez-Casero, R., et al., *Er-doped ZnO thin films grown by pulsed-laser deposition.* Journal of Applied Physics, (2005). **97**(5): p. 054905-054913.

95.Armelao, L., et al., *Structure-luminescence correlations in europium-doped sol-gel Zno nanopowders.* Journal of Physical Chemistry C, (2008). **112**(11): p. 4049-4054.

96.Miranda, S.M.C., et al., *Rapid thermal annealing of rare earth implanted ZnO epitaxial layers.* Optical Materials, (2010). **33**(7): p. 1139-1142.

97.Wahl, U., et al., *Implantation site of rare earths in single-crystalline ZnO.* Applied Physics Letters, (2003). **82**(8): p. 1173-1175.

98.Maiti, U.N., et al., *Novel low temperature synthesis of ZnO nanostructures and its efficient field emission property.* Materials Research Bulletin, (2009). **44**(1): p. 134-139.

99.Wöll, C., *The chemistry and physics of zinc oxide surfaces.* Progress in Surface Science, (2007). **82**(2-3): p. 55-120.

100.Yang, Y.H., et al., *Growth, structure, and cathodeluminescence of Eu-doped ZnO nanowires prepared by high-temperature and high-pressure pulsed-laser deposition.* Journal of Applied Physics, (2010). **107**(5): p. 053502-53506.

101.Luo, L., et al., *Enhanced ultraviolet lasing from europium-doped zinc oxide nanocrystals.* Optical Materials, (2010). **32**(9): p. 1066-1070.

102.Wagner, C.D., *Use of the oxygen KLL auger lines in identification of surface chemical states by electron spectroscopy for chemical analysis.* Analytical Chemistry, (1980). **52**(9): p. 1445-1451.

103.Wang, D.D., et al., *Dependence of energy transfer and photoluminescence on tailored defects in Eu-doped ZnO nanosheets-based microflowers.* Journal of Alloys and Compounds, (2010). **504**(1): p. 22-26.

104.Petersen, J., et al., *Structural and photoluminescence properties of ZnO thin films prepared by sol-gel process.* Journal of Applied Physics, (2008). **104**(11): p. 113539-113544.

105.Schneider, W.D., et al., *Shake-up excitations and core-hole screening in Eu systems.* Physical Review B, (1981). **24**(9): p. 5422-5425

106.Mercier, F., et al., *XPS study of Eu(III) coordination compounds: Core levels binding energies in solid mixed-oxo-compounds EumXxOy.* Journal of Electron Spectroscopy and Related Phenomena, (2006). **150**(1): p. 21-26.

107.Ghosh, P., K.R. Priolkar, and A. Patra, *Understanding the local structures of Eu and Zr in Eu_2O_3 doped and coated ZrO2 nanocrystals by EXAFS study.* Journal of Physical Chemistry C, (2007). **111**(2): p. 571-578.

108.Tsuji, T., et al., *Concentration quenching in Eu-doped ZnO grown by sputtering-assisted metalorganic chemical vapor deposition.* Journal of Luminescence, (2012). **132**(12): p. 3125-3128.

109.Badalawa, W., et al., *Correlation between structural and luminescent properties of Eu^{3+}-doped ZnO epitaxial layers.* Journal of Applied Physics, (2011). **109**(5): p. 053502-053507.

110.Meyer, B.K., et al., *Bound exciton and donor-acceptor pair recombinations in ZnO.* Physica Status Solidi (B) Basic Research, (2004). **241**(2): p. 231-260.

111.Ebisawa, K., T. Okuno, and K. Abe, *Photoluminescence properties of Eu^{3+}-doped ZnO nanoneedles.* Japanese Journal of Applied Physics, (2008). **47**(9): p. 7236-7238.

112.Heitz, R., A. Hoffmann, and I. Broser, *Fe^{3+} center in ZnO.* Physical Review B, (1992). **45**(16): p. 8977-8988.

113.Monteiro, T., et al., *Photoluminescence and damage recovery studies in Fe-implanted ZnO single crystals.* Journal of Applied Physics, (2003). **93**(11): p. 8995-9000.

114.Yu, L. and M. Nogami, *Local structure and photoluminescent characteristics of Eu^{3+} in ZnO-SiO_2 glasses.* Journal of Sol-Gel Science and Technology, (2007). **43**(3): p. 355-360.

115.Zhang, Y., et al., *Photoluminescence and ZnO →Eu^{3+} energy transfer in Eu^{3+}-doped ZnO nanospheres.* Journal of Physics D: Applied Physics, (2009). **42**(8): p. 85106-85112.

116.Yu, Y., et al., *Enhanced emissions of Eu^{3+} by energy transfer from ZnO quantum dots embedded in SiO_2 glass.* Nanotechnology, (2008). **19**(5): p. 55711-557116.

117.Nguyen, T.D., C.T. Dinh, and T.O. Do, *Shape-and size-controlled synthesis of monoclinic ErOOH and Cubic Er_2O_3 from micro- to nanostructures and their upconversion luminescencemmmm.* American Chemical Society, (2010). **4**(4): p. 2263-2273.

118.Armelao, L., et al., *ZnO:Er(III) Nanosystems analyzed by XPS.* Surface Science Spectra, (2006). **13**(1-4): p. 9-16.

119.Ishii, M., et al., *Local structure analysis of an optically active center in Er-doped ZnO thin film.* Journal of Applied Physics, (2001). **89**(7): p. 3679-3684.

120.Swami, G.T., F.E. Stageberg, and A.M. Goldman, *XPS characterization of erbium sesquioxide and erbium hydroxide.* Journal of Vacuum Science & Technology A (1984). **2**(2): p. 767-770.

121.Reynolds, D.C., et al., *Neutral-donor-bound-exciton complexes in ZnO crystals.* Physical Review B - Condensed Matter and Materials Physics, (1998). **57**(19): p. 12151-12155.

122.Hamby, D.W., et al., *Temperature dependent exciton photoluminescence of bulk ZnO.* Journal of Applied Physics, (2003). **93**(6): p. 3214-3217.

123.Misra, P., T.K. Sharma, and L.M. Kukreja, *Temperature dependent photoluminescence processes in ZnO thin films grown on sapphire by pulsed laser deposition.* Current Applied Physics, (2009). **9**(1): p. 179-183.

124.Varshni, Y.P., *Temperature dependence of the energy gap in semiconductors.* Physica, (1967). **34**(1): p. 149-154

125.Przeździecka, E., et al., *Photoluminescence, electrical and structural properties of ZnO films, grown by ALD at low temperature.* Semiconductor Science and Technology, (2009). **24**(10): p. 105014-105023.

126.Wang, L. and N.C. Giles, *Temperature dependence of the free-exciton transition energy in zinc oxide by photoluminescence excitation spectroscopy.* Journal of Applied Physics, (2003). **94**(2): p. 973-978.